THE HYDRODYNAMIC CHARACTERISATION OF AN AXIAL-FLOW MEMBRANE MODULE

Pierre Charl Marais

Thesis submitted in partial fulfillment of requirements for the degree

Master of Science (Chemical Engineering)

at the University of Stellenbosch

Supervisors: Prof. S.M. Bradshaw
Dr. E.P. Jacobs

December 2001

DECLARATION

I, the undersigned, hereby declare that the work contained in this thesis is my own original work and has not previously in its entirety or in part been submitted at any university for a degree.

ABSTRACT

The hydrodynamics of a hollow fibre membrane module for the ultrafiltration of potable water were investigated. The purpose was to use a hydrodynamic model to predict the permeate flux for modules of various dimensions. Various models were considered, but most of them could not account for important effects such as macroscopic radial gradients and wet fibre expansion, found in hollow-fibre membrane modules. The Porous Medium Model was found to be a suitable model and it was used together with a finite element software package, *Fastflo*, to solve for the pressure distributions inside the membrane modules and predict permeate flux. The permeability of the membranes was obtained using a combination of numerical and experimental procedures and was found to be 2.3×10^{-13}m. A cost analysis was performed to find the most economical module dimensions (outer diameter and length) for any required product flow rate. It was assumed that the cost of the fibres and module housing comprised the capital cost, while the operating cost consisted of the pumping energy. A capital recovery factor of 0.3 was used to convert capital costs to a yearly cost. It was found that the optimum module dimensions are an outer diameter of between 90mm and 160mm and a length of 0.6m. Finally the pressure distributions on the lumen and shell sides during both cross-flow filtration and backwash were examined. Shade plots proved useful for identifying possible areas of stagnant flow, as well as indicating where backwash is the most effective.

OPSOMMING

Die hidrodinamika binne-in 'n holvesel membraanmodule vir die ultrafiltrasie van drinkwater is ondersoek. Die doel was om 'n hidrodinamiese model te gebruik om die permeaatvloed vir modules van verskeie dimensies te voorspel. Verskillende modelle is oorweeg, maar die meeste kon nie belangrike faktore soos makroskopiese radiale drukgradiënte of nat veselverlenging in ag neem nie. Die Poreuse Medium Model was die mees geskikte model en is gebruik saam met *Fastflo*, 'n sagteware pakket wat gegrond is op die eindige element metode, om vergelykings vir die drukverspreiding binne-in die module op te los en permeaatvloed te voorspel. Die permeabiliteit van die membrane is verkry met behulp van numeriese en eksperimentele prosedures en 'n waarde van 2.3×10^{-13} m is bepaal. Hierna is 'n koste-analise uitgevoer om die mees ekonomiese module afmetings (lengte en buite-deursnit) te bepaal vir 'n gegewe produk vloeitempo. Daar is aanvaar dat kapitaalkoste bestaan uit die koste van vesels en module-omhulsel, terwyl bedryfskoste bereken is deur die hoeveelheid energie benodig om die pomp aan te dryf. 'n Kapitaalherwinningsfaktor van 0.3 is gebruik om kapitaalkoste om te skakel na 'n jaarlikse koste. Die optimum module afmetings is 'n lengte van 0.6m en 'n buite-deursnit van tussen 90mm en 160mm. Laastens is die drukverspreidings tydens beide kruisvloeifiltrasie en die terugspoelproses ondersoek. Areas van stagnante vloei kan deur middel van skadu-grafieke geïdentifiseer word, terwyl dit ook moontlik is om die terugspoelproses te optimeer.

ACKNOWLEDGEMENTS

I wish to express my sincere gratitude to the following people:

Steven Bradshaw

for acting as supervisor and always being available to help with complicated matters, as well as excellent guidance in the preparation of this thesis.

Ed Jacobs

for initiating this project and giving me an opportunity to participate in the development of membrane technology, as well as sharing his valuable knowledge with me.

The Water Research Commission and National Research Foundation

for providing financial assistance during the course of the project.

Drs. Nick Stokes and Zili Zhu

from CSIRO in Melbourne (Australia) for helping me understand the finer details of *Fastflo*.

Deon Koen

for providing technical assistance in the manufacturing of experimental modules.

My family and friends

for all their support and encouragement during the past three years.

My wife, Patti

for her love, understanding and support through difficult times.

CONTENTS

LIST OF FIGURES

LIST OF TABLES

NOMENCLATURE

Symbol	Unit	Description
$\underline{1}$	-	unit vector
a	-	dimensionless parameter defined by eqn. [3.9]
A	m^2	total membrane surface area
A_{flow}	m^2	cross-sectional flow area
A_m	m^2	membrane area per module
A_r	-	ratio between actual membrane area and required membrane area
A_{req}	m^2	required membrane area
A_{tot}	m^2	actual membrane area
A_v	m^{-1}	membrane surface area per unit volume available for filtration
B_1, B_2, B_3, B_4	Pa	constants in eqns. [3.19] – [3.22]
C	-	flow rate conversion factor
C_{ajd}	c/kL	cost adjusted for required area
C_{cap}	c/kL	capital cost
C_{kWh}	R/kWh	electricity cost
C_{mod}	R	capital cost per module
C_{pump}	c/kL	pumping cost
C_{tot}	c/kL	total cost
C_{yr}	R/yr	pumping cost per year
D_h	m	diameter of permeate outlet
d_i	m	inner fibre diameter
D_i	m	module inner diameter
D_o	m	module outer diameter
d_o	m	outer fibre diameter
d_p	m	mean pore diameter
d_w	m	average fibre wall thickness
e	-	Porosity

Symbol	Unit	Description
E	kW	energy consumption
F	-	fraction retentate
f	-	filtration fraction
g	m/s^2	gravitational constant
H	m	height of permeate slit
i	%	interest rate per year
J	$m^3/s.m^2$	permeate flux
J_{lim}	$m^3/s.m^2$	limiting flux
J_v	m/s	permeate volume flux
K	m^2	fibre wall permeability
K"	-	Kozeny constant
k	m^2	Darcy permeability
k_1	-	dimensionless parameter defined by eqn. [5.5]
k_2	-	dimensionless parameter defined by eqn. [5.5]
k_3	-	dimensionless parameter defined by eqn. [5.5]
l	m	length of pore channel
L	m	module length
La	-	dimensionless parameter defined by eqn. [5.6]
L_{eff}	m	dry fibre length available for filtration
L_p	m	membrane permeability
$L_{p,app}$	m	apparent membrane permeability
L_{wet}	m	wet fibre length available for filtration
m	$Pa.s/m^3$	parameter in eqn. [2.7]
n	Pa.s/m	parameter in eqn. [2.7]
N	-	number of fibres; number of years of operation
OD	m	module outer diameter
p	Pa	hydrostatic pressure
P	-	dimensionless hydrostatic pressure
PD	%	fibre packing density
P_f	Pa	feed pressure
P_i	Pa	inlet pressure

Symbol	Unit	Description
P_p	Pa	permeate pressure
P_T	Pa	transmembrane pressure
Q	m^3/s	experimental transmembrane flow rate
Q_{act}	L/h	actual permeate rate
Q_{feed}	L/h	feed flow rate
Q_i	m^3/s	inlet volumetric flow rate
Q_p	L/h	permeate flow rate
Q_{req}	L/h	required permeate rate
R	-	dimensionless radius
r	m	radial position
R_c	m^{-1}	cake resistance
r_C	m	module inner radius
R_f	m^{-1}	film resistance
r_L	m	fibre lumen radius
R_m	m^{-1}	membrane resistance
r_M	m	fibre outer radius
r_S	m	Krogh cylinder radius
S	m^{-1}	specific surface area
T_L	-	transport modulus for laminar flow
T_S	-	shell side transport modulus
u	m/s	inlet flow velocity
U	-	dimensionless axial velocity
V	-	dimensionless radial velocity
$\underline{\mathbf{V}}$	m/s	superficial velocity vector
X	-	dimensionless length
x	m	axial position

Greek letters

Symbol	Unit	Description
α	-	dimensionless fibre wall radius
β	-	dimensionless shell radius
$\Delta\Pi$	Pa	osmotic pressure drop
ΔP	Pa	estimate for axial pressure drop
ΔP_i	Pa	difference between inlet and permeate pressure
ΔP_{bed}	Pa	pressure drop across the packed bed
Δp_m	Pa	transmembrane pressure drop
Δx	m	fibre wall thickness
ε	-	shell side porosity
ϕ	s^{-1}	fluid source/sink
γ	-	parameter defined by eqn. [3.15] and [3.56]
η	-	pump efficiency
η_0	Pa.s	solvent viscosity
φ	-	fibre volume fraction
κ	-	membrane permeability, defined by eqn. [3.14] and [3.55]
λ	-	parameter defined by eqn. [3.18] and [3.54]
μ	Pa.s	fluid viscosity
Π	Pa	osmotic pressure
θ	yr^{-1}	operating time per year
ρ	kg/m^3	fluid density
σ	m	axial coordinate
τ	-	tortuosity factor
Ψ	-	dimensionless lumen flow rate
ξ	-	dimensionless radial function

Subscripts

0	inlet
1	outlet
L	lumen
r	radial
S	shell
x	axial

Abbreviations

CCF	Capital Charge Factor
CF	Cross-flow
CFD	Computational Fluid Dynamics
CRF	Capital Recovery Factor
DE	Dead-end
ECS	Extra-capillary space
FDM	Finite Difference Method
FEM	Finite Element method
HFMM	Hollow Fibre Membrane Module
H-P	Hagen-Poiseuille
KCM	Krogh Cylinder Model
NOM	Natural organic material
PDE	Partial Differential Equation
PMM	Porous Medium Model
PMT	Periodical Payment / Annuity
PV	Present Value
RTD	Residence Time Distribution
THMFP	Trihalomethane formation potential
TVM	Time value of money
UF	Ultrafiltration

Chapter 1

INTRODUCTION

"We must keep water where it belongs on the national agenda: on the top". - Prof. Kader Asmal, Minister of Water Affairs and Forestry, South Africa (Business Day Newspaper - 23 March 1998).

1.1 THE NEED FOR MEMBRANES

South Africa is a relatively dry country, therefore water provision is one of the main problems that must be dealt with. It is very important that every drop of water be utilized as efficiently as possible. Due to the high population growth, the need for water increases constantly. People from previously disadvantaged communities also demand a better quality of life, which includes access to clean, running water. In the past, these people had to walk for miles to find any water, which was often not fit for human consumption.

Most of our water for domestic and industrial use comes from dams, rivers, mountains and bore holes. These waters usually have a cloudy appearance and dark colour because they contain mud particles and dissolved natural organic matter. The addition of chemicals at purification plants ensures that all these impurities flocculate and sink to the bottom of huge settling tanks, from which the clear water is withdrawn. Sand filters are then employed to remove any particles which may not have been removed and finally chlorine is used to disinfect the water. From here, the water is pumped to the consumer, free of germs and any unwanted properties.

The purification of water as explained above, is the norm in any city or town and all its citizens have access to it. In contrast to this, small rural communities or people living on farms obtain water from irrigation canals, rivers, dams, bore holes and mountain streams. However, none of these waters have undergone purification and may contain harmful viruses, parasites and bacteria. While most people living on farms have access to running water, people from remote rural villages typically have

to walk great distances to obtain water in buckets. Hence their level of hygiene is also very low.

Since it is impossible to supply all rural communities using the technology just discussed with clear, disinfected potable water due to large costs, other ways to provide running water at a reasonable cost have been devised. Lyonnaise des Eaux in France first performed experiments on membrane technology in the 1980s and showed that ultrafiltration (UF) can successfully substitute conventional water clarification processes for drinking water production. UF is a pressure-driven membrane filtration operation that works on the sieving or size-exclusion principle. These membranes act as surface filters for colloidal, particulate and dissolved species in the size range 2 to 30 nm and above. UF therefore offers a technique by which the concentration of natural organic material (NOM), iron and aluminium in water can be reduced, rendering a clarified and disinfected product for potable use.

Conventional processes rely heavily on dosing chemicals, which mix with the flocculated impurities. The result is a chemical-rich sludge, which is detrimental to the environment when disposed of. Flocculation and sand filtration are effective in removing macro impurities, but they fail to remove all micro organisms. Furthermore, chlorine as a disinfectant may lead to the formation of carcinogenic trihalomethanes. Certain pathogens, such as *Cryptosporidium,* are also resistant to traditional disinfectants. Membrane technology has important environmental benefits over conventional processes since it offers an impermeable barrier to impurities in water and reduces or eliminates the need for dosing chemicals. In a study conducted on Parisian waters in France by Cabassud *et al.* (1991), they compared various quality parameters such as microbial count, aluminium and iron content, turbidity and trihalomethane formation potential (THMFP) in raw water with that in ultrapure water. They showed that UF removed all bacteria, 40% of the THMFP, 95% of the aluminium content and all of the iron content. In comparison with conventional filtration, UF needs relatively little equipment and floor space. The technology is therefore well suited for point-source provision of safe-drinking water.

1.2 MODULE DESIGN

The application of membranes in practice must be such that it is technically and economically viable. Although there are many different possible designs, all membranes are housed in a unit called a module. The idea is then to maximize the membrane area within a module available for filtration. Of course, the filtration system can consist of a number of modules manifolded in series or parallel arrangements. Generally, two membrane geometries are available: flat and tubular. The type of module design depends on various factors such as the type of separation, ease of operation, duration of the membranes' life, ease of cleaning, packing density etc. A typical pressure-driven membrane filtration operation is shown in fig. 1 below. A feed pump supplies contaminated water to the membrane module. Only clean water filters through the porous membranes and is collected as permeate from the shell side, while the retentate leaves the membrane module at the downstream end. A part of the retentate is recycled to ensure that the minimum cross-flow velocity is maintained.

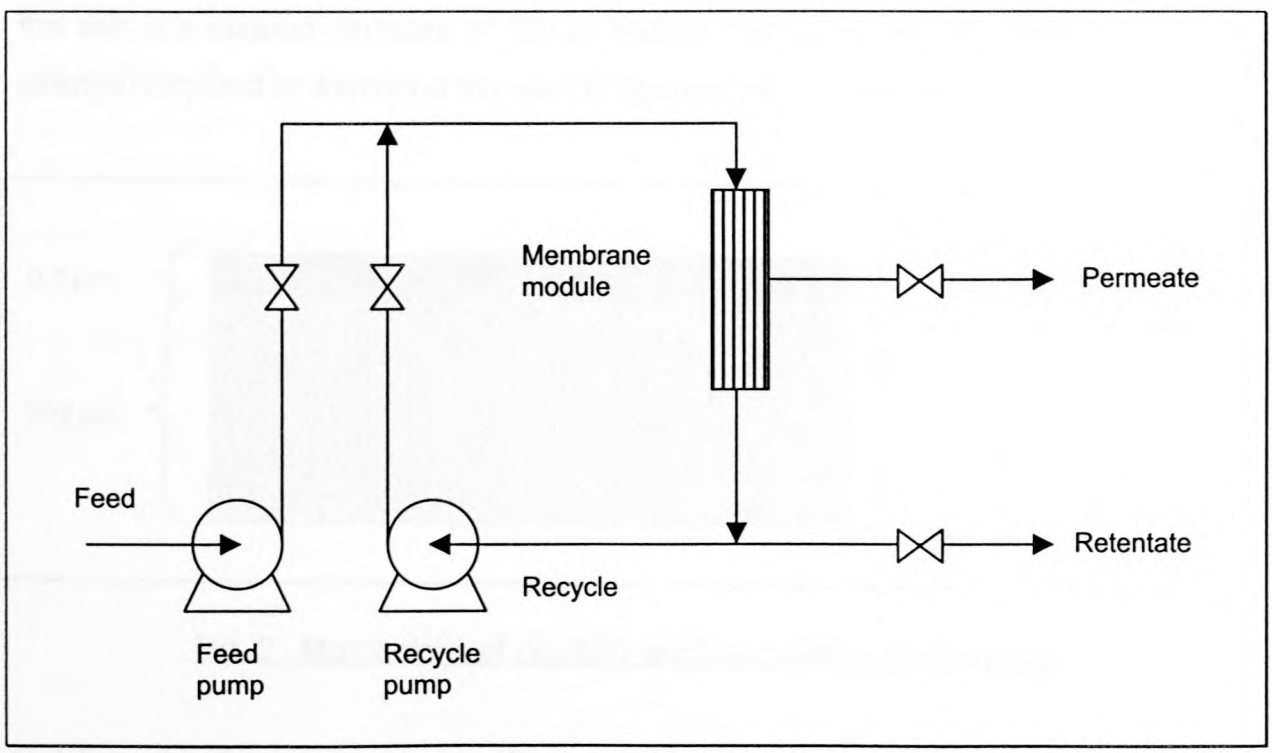

Fig. 1 : A typical pressure-driven membrane filtration operation.

Two types of module configurations involve flat membranes: Plate-and-frame modules and Spiral-wound modules. Plate-and-frame modules consist of sets of two flat membranes facing each other with their filtration sides. A spacer is placed between each set. In this manner, a packing density of up to 400 m^2/m^3 can be achieved. In Spiral-wound modules, the membranes are arranged in the same way as in the Plate-and-frame modules, except that sheets are wrapped around a central perforated pipe that collects the permeate. A packing density of 1 000 m^2/m^3 is possible.

Narrow bore tubular membranes can be subdivided into two types, depending on the diameter: capillary and hollow-fibre. These membranes are encapsulated inside tubes to form a module. Capillary membranes with the active retention layer on the inside are referred to as internally skinned. It is also possible to have the skin layer on the outside or on both sides, resulting in a double-skinned membrane. A cross-section of the wall of a one-side skinned membrane is shown in fig. 2. The skin layer is a thin section about 0.1 to 0.2 μm thick. The separation capability of the skin determines the size of macromolecules that is retained on the skin surface. Below the skin is a support structure of 100 to 300 μm thickness, providing the mechanical strength required to withstand the operating pressure during filtration.

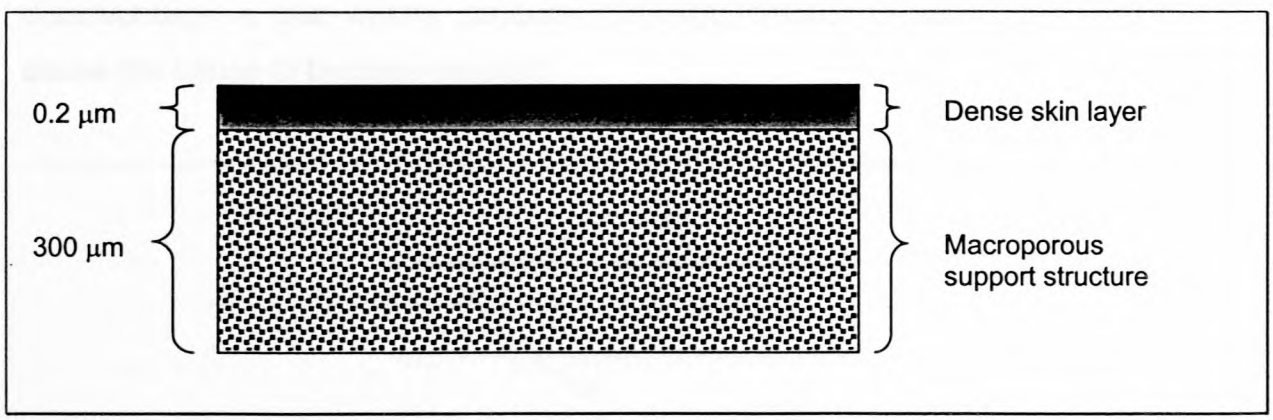

Fig. 2 : Morphology of capillary and hollow-fibre membranes.

Capillary membranes and hollow-fibre membranes are both assembled in the same way inside their modules, the only difference being the size of the tube diameters. Their free ends are potted in epoxy resin at both ends of the module, thus these membranes are self-supporting. With capillary membranes, a packing density of

about 1 200 m^2/m^3 is possible while hollow-fibre membranes boast the highest packing density: 30 000 m^2/m^3.

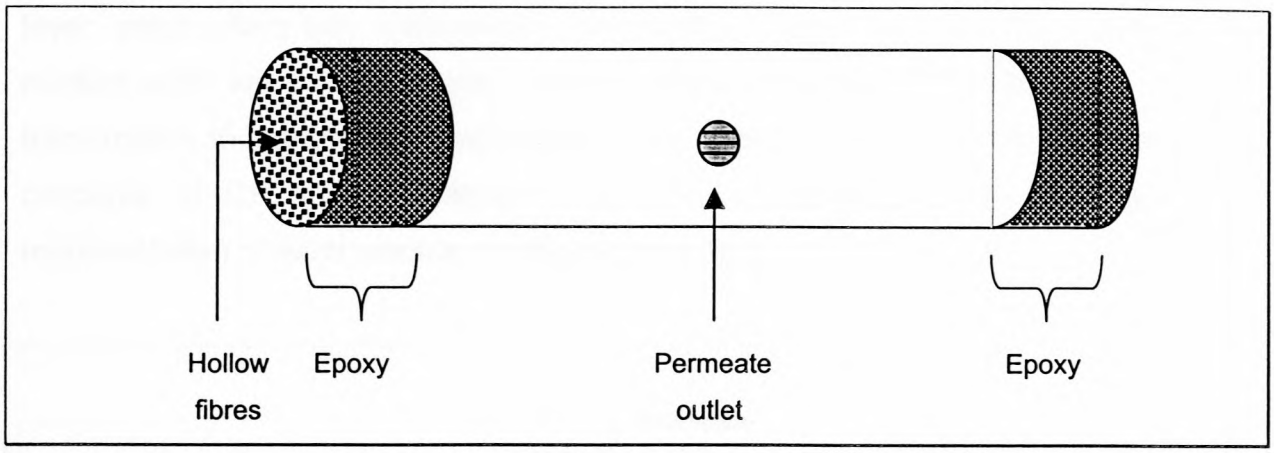

Fig. 3 : Assembly of tubular membranes inside a module.

Various types of flow configurations are possible, like inside-out, outside-in, cross-flow (CF), dead-end (DE), etc. (see figs. 4 and 5). With inside-out filtration, the feed stream enters the inside (or lumen side) of the capillaries and concentrate flows out at the downstream end. Clean water is collected on the outside (or shell side) of the capillaries. A possible advantage of this configuration is that the high fluid velocities can help reduce fouling of the membrane surface, while a disadvantage is that waters containing a large amount of suspended solids may cause the lumen to become blocked.

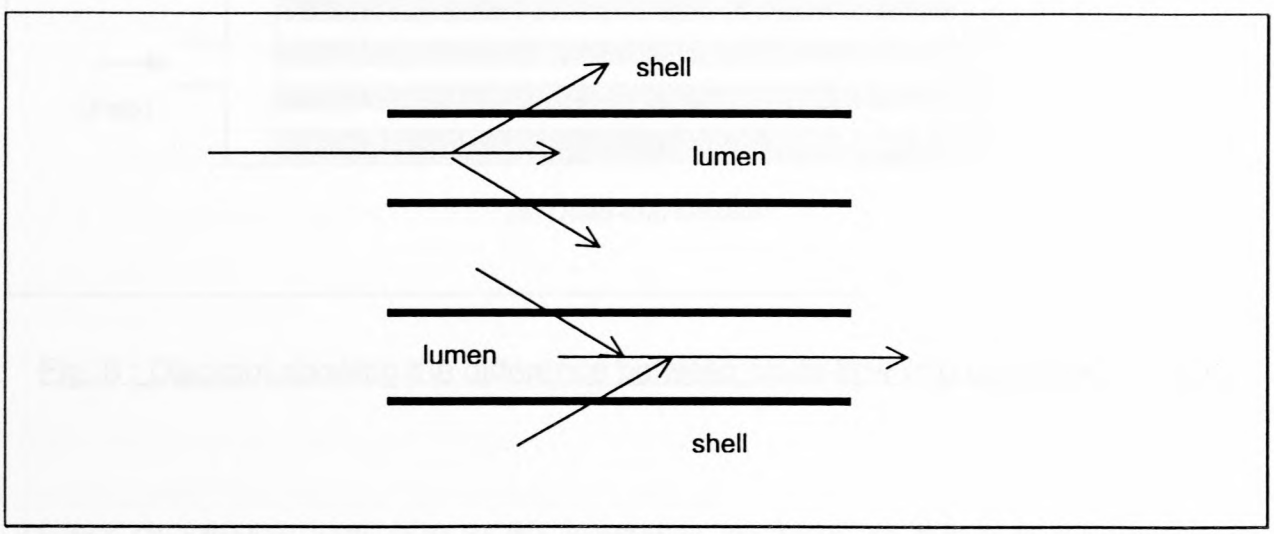

Fig. 4 : Inside-out vs. Outside-in filtration.

Outside-in filtration, as used by Serra *et al.* (1998), is the opposite process, i.e. water is fed from the shell side. This configuration appears to be superior to inside-out filtration, because it provides a greater filtering surface. The result is a thinner cake layer, which offers less resistance to permeation. An added advantage is that only purified water flows in the lumen, eliminating any possibility of fibre blocking. This in turns means that any appropriate value for the fibre inner diameter can be used. The concepts of CF and DE filtration are best explained by way of a graphical representation of each module configuration in fig. 5.

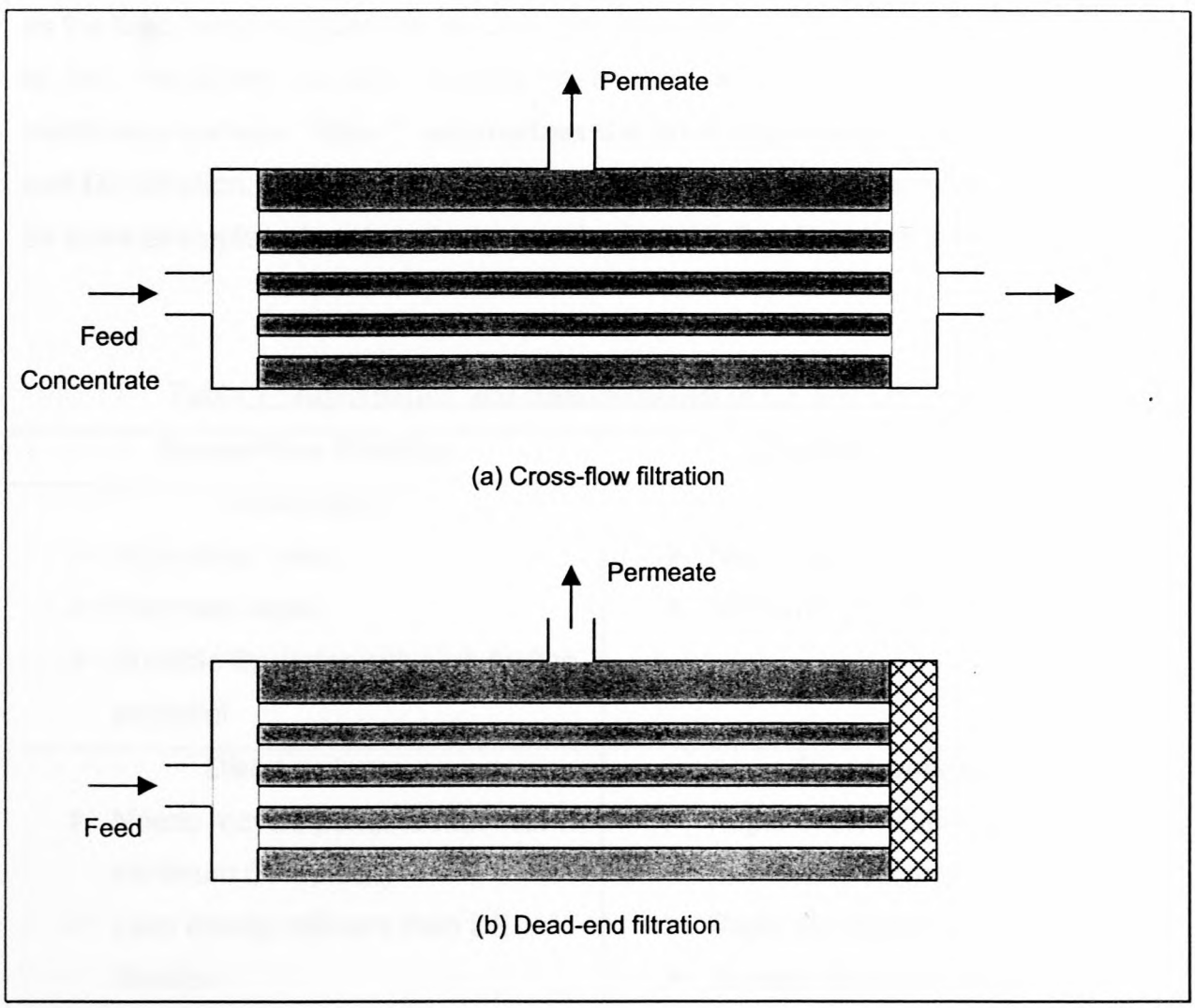

Fig. 5 : Diagram showing the difference between cross-flow and dead-end filtration.

During *CF filtration* both ends of the capillaries are open, so that feed fluid enters at the one end and flows out at the other end. As the flow is parallel to the membrane

surface, the high shear rates prevent the build-up of too much solute on the membrane surface. Clean water filters through the membranes to the space between the fibres (the shell side), where it is withdrawn as permeate. In fig. 1, the feed pump supplies the feed stream to the module, while a part of the downstream retentate is recycled to maintain the minimum cross-flow velocity across the membranes.

In *DE filtration* the downstream end of the capillaries is blocked, so that all the feed water passes through the membrane to the permeate side. No recycle pump is used as the feed pump supplies the required pressure and flow rate. Flow is perpendicular to the membrane surface, leading to a rapid accumulation of solutes on the membrane surface. Table 1 summarizes the advantages and disadvantages of CF and DE filtration. A more detailed description of each module configuration as well as a few examples of system design can be found in the literature (Mulder, 1991).

Table 1 : Advantages and disadvantages of CF and DE filtration

Cross-Flow filtration	**Dead-End filtration**
Advantages ➢ High shear rates ➢ Thin cake layer ➢ Suitable for water with high fouling potential	*Advantages* ➢ Needs feed pump only ➢ Very energy efficient
Disadvantages ➢ Needs recycle pump to maintain minimum CF velocity ➢ Less energy efficient than DE filtration	*Disadvantages* ➢ Rapid accumulation of solutes on membrane surface ➢ Rapid flux decline ➢ Suitable for water with low fouling potential

The design of a membrane module filtration system consists not only of module configuration, but also of performance optimisation. It is important to establish the optimum module dimensions and operating parameters. Serra *et al.* (1998) developed a model, which predicts the net production rate during an operating cycle.

Each operating cycle consists of a filtration phase, during which the membranes are fouled, followed by a backwash phase that removes the fouling layer. The model is used to optimise the module geometry by calculating the net production rate as a function of fibre diameter, void fraction, membrane permeability, fibre length and fibre outside-to-inside ratio. It can also be used to determine how the module's performance varies with changing operating parameters and feed properties. Finally energy costs can be calculated.

Starov *et al.* (1995) optimised module geometry by investigating the sensitivity of fibre performance to fibre length. They used an analytical model to optimise performance, which is a balance between productivity and selectivity. Productivity is defined as the fraction of feed recovered as permeate, while selectivity is an indication of the amount of solute rejected by the membrane. A dimensionless length parameter was used as independent variable to gauge how fibre performance changes as a function of length. Selectivity tends to zero as productivity increases to 1.0, so the aim is to find the optimum combination of productivity and selectivity for each module configuration. In a subsequent study Smart *et al.* (1996) extended the above optimisation by examining the sensitivity of fibre performance to operating pressure, packing density and fibre diameter. They found that the productivity and selectivity exhibit a similarity property over a wide range of operating parameters, for various flow configurations. From the above it is thus clear that any membrane process can be simulated and the design and operating parameters optimised.

1.3 AIMS OF THE THESIS

The current project is part of a membrane module programme launched by the Institute for Polymer Science (IPS) at the University of Stellenbosch and funded by the Water Research Commission (WRC). The aim was to investigate the viability of a low-cost membrane filtration system for the treatment of sub-standard surface waters. In 1994 a $3m^2$ bench scale UF pilot plant was installed as an undergraduate engineering project (Botes, 1995) at the Mon Villa Seminar Centre on a farm 15km outside Stellenbosch. The work was extended in 1996 with the erection of a 15 m^2 pilot plant at the same site. A module of 90mm outer diameter, 1.2m length and 57.4% fibre packing density was used in a CF filtration set-up as in fig. 1. Although

the process was proven to be successful (Botes, 1995; 2000), one of subsequent aims was to scale up the modules, which is where the current project fits in.

The work presented in this thesis is largely a theoretical study to :

- investigate the hydrodynamics inside a membrane module, and
- improve the design of such a module.

Hydrodynamic models were used to improve the design of a hollow-fibre membrane module (HFMM) for the UF of potable water. Previous modelling work on hollow-fibre systems was looked at and a newer model, which takes into account important effects neglected by previous models, was used for a hydrodynamic analysis of a HFMM in this study. The strengths and weaknesses of the various models are discussed and compared to each other. The latest model was implemented using a finite element software package to simulate the hydrodynamics inside a HFMM, as well as predicting permeate fluxes for various module geometries. Finally a cost study was done to compare the operating costs of various module geometries to find the most cost effective HFMM.

1.4 STRUCTURE OF THE THESIS

The thesis will follow the structure set out below:

- Chapter 2 covers a brief description of membrane physical properties, various membrane processes, some elementary flux modelling theory and a discussion about fouling.

- Chapter 3 looks at the design of a typical HFMM and a few practical applications, before reviewing previous modelling work on hollow-fibre systems. The new approach is discussed and compared with the previous models.

- Chapter 4 contains an overview of computational fluid dynamics and the finite element method, which form the basis of the numerical simulation in this thesis. Finally the features of the software package, *Fastflo*, are discussed.

- Chapter 5 highlights the two coupled partial differential equations to be solved by the numerical software, how they are translated into *Fastflo* syntax and their solution. The estimation of two important parameters is also explained.

- Chapter 6 lists the base parameters used in this thesis and discusses all the results obtained with the numerical simulation.

- Finally Chapter 7 contains the main conclusions of this thesis, as well as some recommendations for future research.

~~~
~~~

Chapter 2

MEMBRANE AND MODULE BASICS

2.1 DEFINITION AND PHYSICAL PROPERTIES OF MEMBRANES

A membrane in general may be defined as a selective barrier between two phases, with the upstream side being the feed and the downstream side being the permeate. It is a porous medium that separates unwanted substances from a liquid or gas stream by retaining those particles that are too large to pass through the pores. Initially, organic polymers, like cellulose, were used to make membranes, but they have very low resistance to thermal, chemical and biological attack. Today, synthetic organic polymers like polyamide or polysulphone are preferred, mostly on account of their superior chemical and thermal resistance. Membranes can be divided into two groups: porous and non-porous, depending on the application. Porous membranes are used in UF while non-porous membranes are used in operations like gas separation. Inorganic materials, like ceramics, are also used to manufacture membranes. Although they do not cover such a wide size range as polymeric membranes, they are extremely tolerant against chemical and thermal attack. Biological membranes are known to us as membranes appearing in living cells, but their structure and functionality is very different from synthetic membranes. Transport of molecules across these membranes is necessary for cell metabolism and growth.

2.2 MEMBRANE PROCESSES

Filtration is the process of separating two or more components from each other, by the principle of size exclusion. Usually, conventional filtration can separate only particles larger than 5μm in diameter from solvents. Sometimes, chemicals are also added as disinfectants and flocculants. Of all the various separation methods available today, membrane processes are relatively new. In the late 1950s, the first membrane desalination separation was achieved by Sourirajan and Loeb (Cheryan, 1998). This made it possible to separate particles in the sub micron range. Since

then, many different kinds of membrane separation techniques have been developed. At present, this is one of the fastest growing technologies, finding increasingly more applications. Although there are many different kinds of membrane processes, they all have at least one common component: the membrane itself, in whatever form it may be. Most of these techniques are pressure-driven, which means that a pressure differential across the membrane is the driving force behind the separation. The main types are:

- Microfiltration (MF)
- Ultrafiltration (UF)
- Nanofiltration (NF)
- Reverse Osmosis (RO)

There are also three other types of membrane processes, viz electrodialysis (ED), dialysis (D) and membrane distillation (MD), but they have different driving potentials, as shown in table 2. All these techniques make it possible to cover a wide range of particle sizes. They are classified in the table below.

Table 2 : Different types of membrane separation techniques

Type	Driving potential	Pore Size Range	Typical application
MF	Pressure	10 - 0.1 μm	Food sterilization
MD	Temperature	1 - 0.2 μm	Boiler feedwater
UF	Pressure	10-0.001 μm	Cheese making
NF	Pressure	< 0.005 μm	Water softening
RO	Pressure	< 0.005 μm	Seawater desalination
D	Concentration	< 0.005 μm	Artificial kidneys
ED	Electrical field	No pores	Chlor-alkali process

2.3 FLUX MODELLING

Pressure driven processes are governed by several factors, which determine the permeation rate through a membrane. For this purpose, the general membrane equation (Coulson & Richardson, 1991) is used:

$$J = \frac{|\Delta P| - |\Delta \Pi|}{\mu(R_m + R_c + R_f)} \qquad [2.1]$$

where

J	=	Membrane permeation rate [$m^3/s/m^2$]
$\|\Delta P\|$	=	Transmembrane pressure [Pa]
$\|\Delta \Pi\|$	=	Osmotic pressure difference across membrane [Pa]
μ	=	Fluid viscosity [Pa.s]
R_m	=	Membrane resistance [m^{-1}]
R_c	=	Cake resistance [m^{-1}]
R_f	=	Film resistance [m^{-1}]

In order to compare the flux capability of different membranes with each other, pure water that contain no solutes, must be used. Eqn. [2.1] then reduces to an equation analogous to the well-known Carman-Kozeny equation (Coulson & Richardson, 1991):

$$J = \frac{|\Delta P|}{\mu R_m} \qquad [2.2]$$

The Carman-Kozeny equation describes the relation between pressure drop and mean velocity for flow through packed beds in terms of porosity and specific surface and is given by:

$$u_{ave} = \left(\frac{1}{K''}\right)\left(\frac{e^3}{S^2[1-e]^2}\right)\left(\frac{-\Delta P_{bed}}{S^2 \mu l}\right) \qquad [2.3]$$

where

u_{ave} = Average fluid velocity [m/s]

K" = Kozeny constant [-]

E = porosity [-]

S = Specific surface area [m^{-1}]

μ = Fluid viscosity [Pa.s]

L = Length of pore channel [m]

ΔP_{bed} = Pressure drop across the packed bed [Pa]

From eqn. [2.2], it is clear that a lower membrane resistance will yield a higher flux. Since viscosity is a function of temperature, a higher temperature will give rise to a lower viscosity, resulting in a higher flux. A better approximation of the UF flux can be obtained by the following expression, which is equivalent to the Hagen-Poiseuille equation (Cheryan, 1998):

$$J = \frac{\varepsilon d_p^2 P_T}{32 \Delta x \mu} \qquad [2.4]$$

where

ε = Surface porosity of the membrane [-]

d_p = Mean pore diameter [m]

P_T = Transmembrane pressure [Pa]

Δx = Membrane thickness [m]

μ = Fluid viscosity [Pa.s]

A plot of J vs. P_T indicates that there is a linear relationship between them, i.e. an increase in pressure will result in a proportional increase in flux. However, as time progresses with filtration, solutes build up on the membrane surface, thus creating more resistance to flux. The flux-pressure relationship is no longer linear and the more the pressure is increased, the less the flux increases. At a certain level, a condition will be reached where the flux no longer increases, regardless increase in

pressure. This phenomenon is known as the "limiting flux". Other models must now be used to predict the flux.

Different theories exist to model flux in the pressure independent region where mass transfer controls. These are the gel polarization model, the osmotic pressure model and the resistance-in-series model (Yeh & Wu, 1997; Aimar *et al.* 1991). Before these models are described, the concept of the concentation boundary layer must be introduced.

2.3.1 The Concentration Boundary Layer

As solutes accumulate at the membrane surface, the concentration increases, with the highest concentration being at the membrane surface. Moving away from the surface, the concentration decreases until it reaches a constant value in the bulk of the fluid. The region of varying concentration is the concentration boundary layer and is characterized by a concentration profile, as depicted in fig. 6. In addition to the concentration boundary layer, there exists an analogous boundary layer, the velocity boundary layer. This develops because of the friction between the fluid and the membrane surface. The fluid nearest to the membrane surface will be retarded while higher fluid layers will be accelerated. Again, a velocity profile is established.

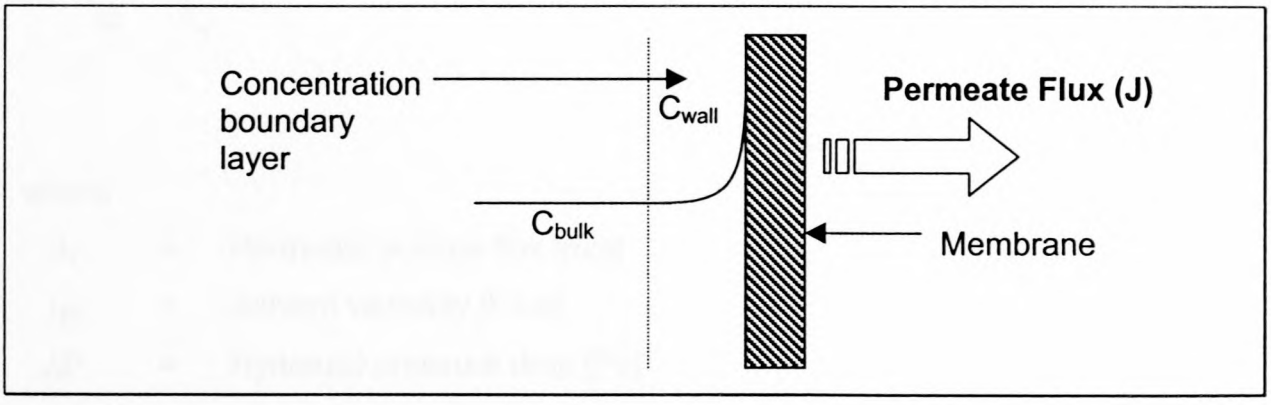

Fig. 6 : Concentration boundary layer.

2.3.2 Gel Polarisation Model

The gel polarization model assumes that the permeation rate is pressure independent. It states that a gel layer forms on the membrane surface and that this gel layer offers hydraulic resistance which reduces permeate flux. This model is only valid at steady state, when the convective precipitation of solutes is balanced by the particle backtransport (Wetterau *et al.* 1996). However, there are some limitations to the gel polarization model (Lee & Clark, 1997). One theory states that macromolecules convect to the membrane surface while colloidal particles migrate away to some region between the membrane surface and the hollow-fibre centreline. This is known as the *tubular pinch effect* (Belfort, 1989).

2.3.3 Osmotic Pressure Model

Wijmans *et al.* (1985) have done UF experiments with Dextran solutions to show that the permeation rate is less than the pure solvent flux due to the effects of osmotic pressure. The osmotic pressure reduces the original driving force and the permeate flux is given by:

$$J_v = \frac{1}{\eta_0}\frac{\Delta P - \Delta\Pi}{R_m} \qquad [2.5]$$

where

J_v	=	Permeate volume flux [m/s]
η_0	=	Solvent viscosity [Pa.s]
ΔP	=	Hydraulic pressure drop [Pa]
$\Delta\Pi$	=	Osmotic pressure difference [Pa]
R_m	=	Membrane resistance [m^{-1}]

The osmotic pressure, Π, is a function of concentration:

$$\Pi = a_1 C + a_2 C^2 + a_3 C^3 \qquad [2.6]$$

where a_1, a_2 and a_3 are coefficients and C is the concentration at the membrane surface.

It can be shown (Coulson & Richardson, 1991) that when $J \rightarrow 0$,

$$|\Delta P| = aC_f^n = \Pi \qquad [2.7]$$

Thus an increase in concentration will give an increase in the osmotic pressure, which in turn decreases the driving force, $|\Delta P| - |\Delta \Pi|$. The result is a decline in the permeation rate.

2.3.4 Resistance-in-Series Model

Finally, the resistance-in-series model takes into account the effect of fouling or solute adsorption, which leads to a decrease in the permeation rate. Yeh & Wu (1997) derived an equation which predicts permeate flux by taking into consideration the decline in transmembrane pressure along the tube axis of the hollow-fibres:

$$\bar{J} = \frac{1}{\phi} + \frac{R_m + R_f}{\left(mQ_i - n\bar{J}\right)\phi^2} \ln\left[1 - \frac{\left(mQ_i - n\bar{J}\right)\phi}{R_m + R_f + \phi \Delta P_i}\right] \qquad [2.8]$$

where

$\bar{J}$ = Average permeate flux of a hollow-fibre module [$m^3/s.m^2$]

ϕ = $1/J_{lim}$ [$m^2.s/m^3$]

J_{lim} = Limiting flux [$m^3/s.m^2$]

R_m = Intrinsic membrane resistance [Pa.s/m]

R_f = Film resistance [Pa.s/m]

m = $\frac{8\mu L}{N\pi r_L^4}$ [$Pa.s/m^3$]

μ = Fluid viscosity [Pa.s]

L = Fibre length [m]

r_L = Fibre lumen radius [m]

n = $\frac{8\mu L^2}{r_L^3}$ [Pa.s/m]

Q_i = Inlet volumetric flow rate [m^3/s]

ΔP_i = $P_i - P_p$ [Pa]

P_i = Inlet pressure [Pa]

P_p = Permeate pressure [Pa]

Yeh & Wu (1997) performed experiments on four different combined-module systems with three identical modules each. Using various feed concentrations, transmembrane pressures and feed flow rates and by using eqn. [2.8], they obtained the best flux results with the modules arranged in series.

2.4 FOULING PHENOMENA

The greatest limiting factors in UF process applications are concentration polarization and fouling. *Concentration polarization* (CP) can be defined as the accumulation of solute near the membrane surface. It begins to form immediately but is a reversible process. *Fouling*, on the other hand, is the adsorption of solutes onto the membrane surface and clogging of the membrane pores. The fouling layer takes longer to form and its effect is irreversible. Since these two factors lead to flux decline and thus higher energy consumption, methods must be used to restore the flux to the highest value as possible.

2.4.1 Backwashing

Before UF, various pre-treatment steps can be employed, like the addition of chemicals or the use of vortex strainers. These methods serve to pre-treat the water and remove larger particles, but are not able to prevent CP or fouling entirely. Backwashing is the preferred method of combatting CP and fouling directly. The basic principle here is the periodic reversal of the permeate flow, thus also reversing the transmembrane pressure. This works very well with hollow-fibres because they are self-supporting. The problem is to find the optimal frequency and duration of backwashing. Wetterau *et al.* (1996) have done several experiments on the effects of fouling and they presented a method for optimising the backwashing frequency. Nakatsuka *et al.* (1996) suggested that the backwashing pressure must be at least twice as high as the forward filtration pressure in order to maintain a constant and high flux. According to Botes (2000), backwashing is the *only* flux enhancement strategy that is used extensively on full-scale capillary type membrane plants, as demonstrated by authors such as Redkar & Davis (1993) and Matsumo *et al.* (1987; 1988) during the cross-flow filtration of yeast suspensions.

2.4.2 Backpulsing

Backpulsing, a similar technique to the above, is described by Redkar *et al.* (1996). The only difference is that backpulsing occurs much more frequently. According to their model, forward filtration must proceed until a certain critical time, $t_{crit.}$, before backpulsing is applied to depolarise the gel layer. However, their theory assumes that foulants are completely removed from the membrane surface and it does not take into account pore blocking or solute adsorption.

2.4.3 Air Sparging

The disadvantage of backwashing and backpulsing is that they use the clean product, thus temporarily suspending the production. The remedy to this is to make use of air injection into the feed stream, as first described by Cui & Wright (1996) in their investigation of air sparging in downward CF UF. A two phase gas/liquid flow, termed slug flow, develops, which create high wall shear stresses. The successive

positive and negative shear stresses prevent particle deposition by lifting them from the membrane surface. The result is a thicker but more porous cake, which offers less resistance to permeation. In this way the flux is enhanced and thus the need for backwashing is reduced. Mercier *et al.* (1997) and Cabassud *et al.* (1997) also showed with their experiments that the high shear stresses created by the slug flow could enhance flux. The only drawback to air sparging is that additional equipment such as compressors, gas bottles and air release equipment are needed, as mentioned by Botes (2000).

2.4.4 Flow reversal

HFMMs are usually installed in a vertical position (to minimize floor space), so that the flow through it is either upward or downward. Permeate can then be withdrawn either in a cross-current or co-current fashion. As water flows along the fibres, the feedstream gets more concentrated by the dewatering action. The result is that the downstream side is dirtier than the upstream side and the membrane becomes more fouled there, according to Breslau *et al.* (1980). The solution to this is to put the module in flow reversal mode by closing the permeate outlet, as described by Breslau *et al.* (1980). Consider a module where the flow is upwards and permeate is withdrawn co-currently from the top of the module (fig. 7). The inlet pressure is 80 kPa and the outlet pressure is 20 kPa. By closing the permeate outlet, the flow will continue as before, but no permeate leaves the module. An average pressure of 50 kPa will exist within the module. Since the pressure at the inlet will still be higher than the average pressure, permeate will still be produced as before. At the top end however, the shell side pressure is greater than the discharge pressure and the permeate will flow back into the fibres, thus cleaning those fibres in the upper part of the module (see fig. 8). By reversing the direction of flow through the module, the same cleaning action can be applied to the fibres in the lower part. Flow reversal is thus advantageous in the sense that no permeate is used for restoring the flux.

Iritani *et al.* (1991) compared experimental results of CF upward UF with those of CF downward filtration. They found that DE upward UF is more effective than CF downward filtration below the critical shear stress, $\tau_{w,c}$, at the membrane surface, whereas CF upward filtration is more effective than DE upward filtration above $\tau_{w,c}$.

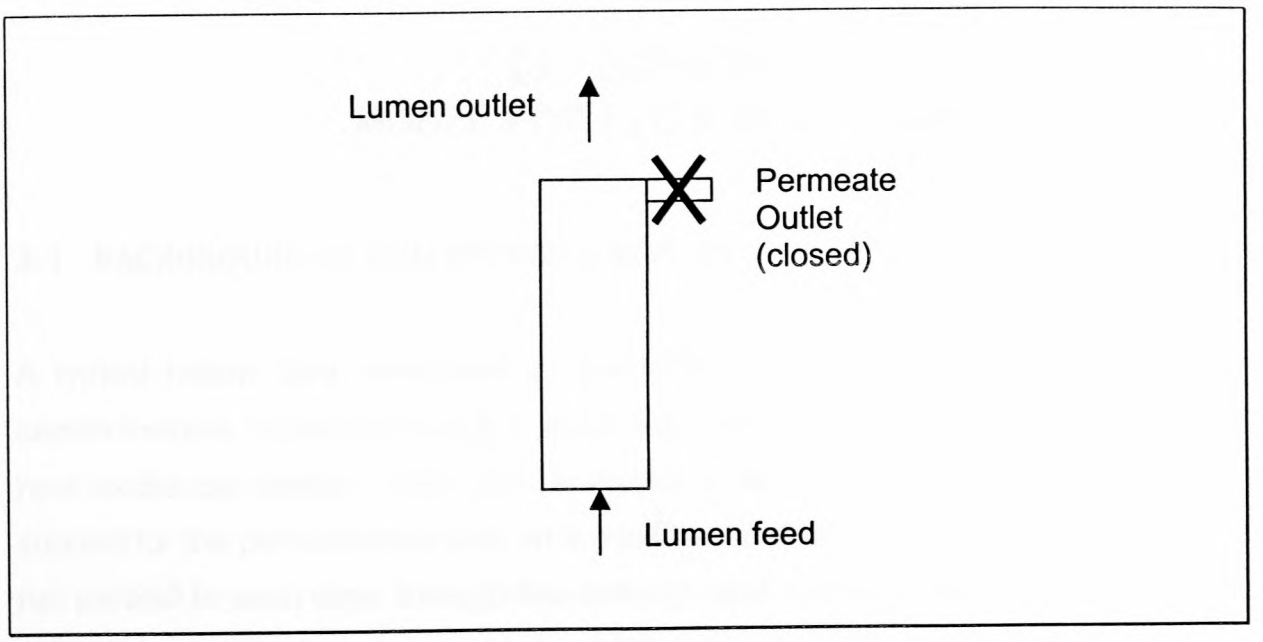

Fig. 7 : Co-current filtration.

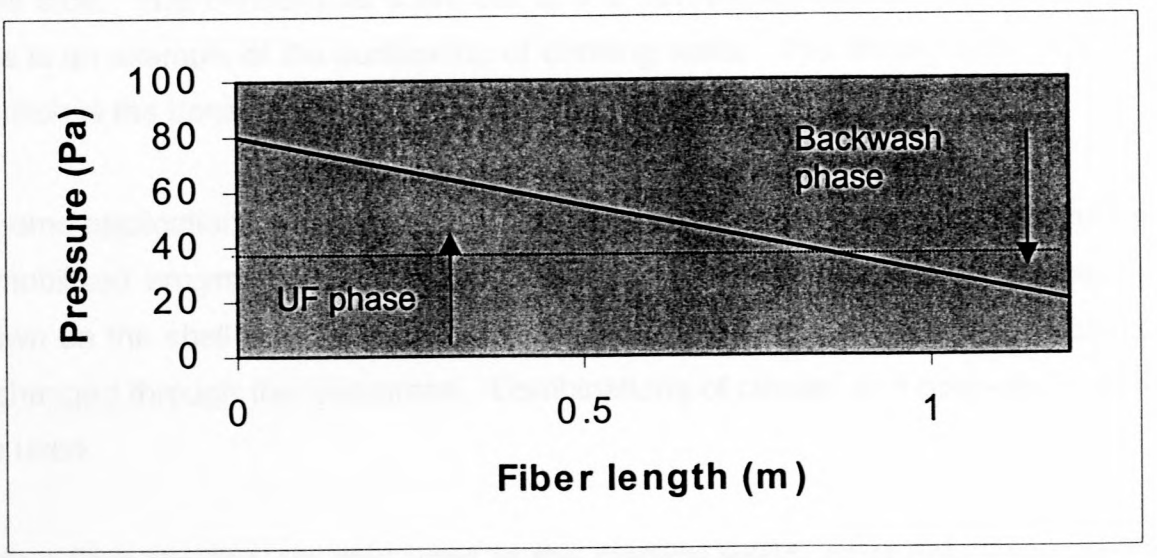

Fig. 8 : Pressure profile in a HFMM during recycling.

~~~
~~~

Chapter 3

DEVELOPMENT OF A MATHEMATICAL MODEL FOR FLOW IN A MEMBRANE MODULE

3.1 BACKGROUND OF HOLLOW-FIBRE DEVICES

A typical hollow fibre membrane module (HFMM) consists of a bundle of fibres sealed inside a cylindrical cartridge, much like a shell-and-tube configuration found in heat exchanger design. Each fibre is mainly a macroporous matrix, which acts as support for the permselective skin on the inside, outside or on both sides. The fibres run parallel to each other through the cartridge and they are potted in epoxy at both ends, their lumina being open at the inlet and outlet. The inside of the fibres is referred to as the lumen side, while the space surrounding the outside of the fibres is called the shell side. Typically, fluid is pumped through the lumina, the permselective skin retains particles larger than its pore size and only pure fluid filters through to the shell side. The concentrate flows out at the downstream side of the fibre lumina. This is an example of the purification of drinking water. The driving force behind the filtration is the transmembrane pressure drop.

In some applications hollow-fibre systems are used as bioreactors for cell culture and immobilized enzymes (Patkar *et al.* 1995; Piret & Cooney, 1990). The cells are grown on the shell side while the recycling lumen flow provides nutrients, which are exchanged through the membrane. Combinations of closed- and open-shell modes are used.

Hollow-fibre devices are also used in the medical world, most notably as artificial livers or pancreas (Chick *et al.* 1975; Wolf, 1980) where a patient's natural organs have failed. The best-known example is the process of haemodialysis (Bosch, 1993), during which blood is passed through a hollow-fibre system acting as artificial kidneys. Blood flows through the fibre lumina with the dialysate moving counter-currently through the shell side. Yoshikawa *et al.* (1992, 1994) also experimented with extracorporeal blood treatment by separating plasma from blood in a HFMM.

3.2 PREVIOUS HYDRODYNAMIC MODELS

The main advantage of hollow-fibre devices is the large surface area per unit volume available for fluid transport. In order to understand the flow inside these systems, the hydrodynamics occurring inside them must be modelled mathematically. One of the earliest attempts was performed by Krogh (1919), who made calculations on the oxygen pressure head required in capillaries in muscles. He assumed that all the capillaries have the same multi-fibre geometry, which allowed him to use only one representative fibre for modelling the hydrodynamics. In his honour, this single representative fibre is called the Krogh cylinder, with an outer radius, R_S, which is the radius of the surrounding fluid annulus. The Krogh cylinder is defined such that the porosity of a single fibre unit is the same as the porosity of the whole fibre bundle. Also, the fibres are assumed to be arranged in a regular array with no fluid exchange between adjacent Krogh cylinders. Radial pressure gradients are also neglected.

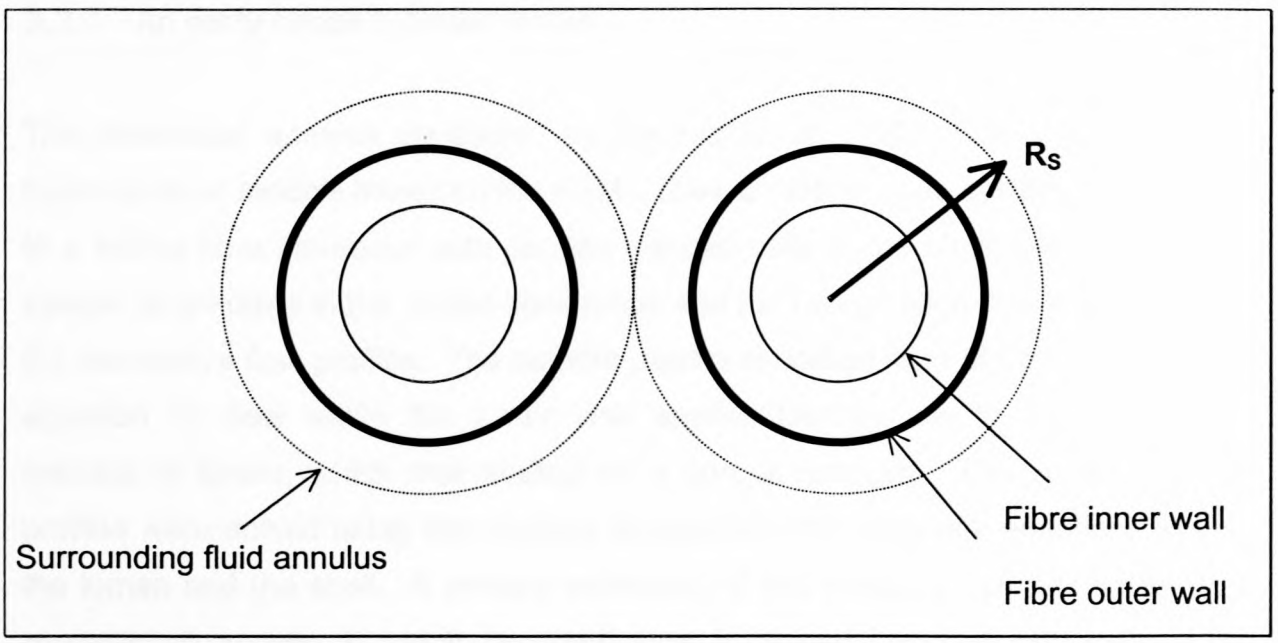

Fig. 9 : The Krogh Cylinder.

Fig. 9 shows the geometry of the Krogh cylinder. The inside of the fibre is called the lumen and it is surrounded by a macroporous matrix. The dotted line indicates the surrounding fluid annulus. The Krogh Cylinder Model (KCM) was used as basis for modelling by several authors [e.g. Apelblat *et al.* (1974), Bruining (1989), Kelsey *et al.* (1990), Pangrle *et al.* (1991) and Yoshikawa *et al.* (1992, 1994)]. They all used

different combinations of the Navier-Stokes equation (for lumen and/or shell side flows) and Darcy's Law (for flow within the permeable capillary wall) for modelling the flow in their hollow-fibre systems.

Roos (1992) followed a slightly different approach than the KCMs by modelling the flow through membranes by means of volumetric averaged equations for incompressible Newtonian flow through porous media. This method was an improvement on simpler methods in that it could solve the governing equations in complex geometries such as tubular, prismatic, foamlike and granular porous structures. A FORTRAN program was used to solve the volumetric averaged equations and the results compared very well to statistical and experimental results.

A brief description of the KCMs will now be given to show their aims, strengths and weaknesses.

3.2.1 An early Krogh Cylinder Model

The theoretical analysis developed by Apelblat *et al.* (1974) was one of the first hydrodynamic models based on the KCM. Their capillary tissue system is analogous to a hollow-fibre bioreactor with densely packed cells in the shell side space. The system is operated in the closed-shell mode and the recirculation flow is modelled by the convective flow profiles. The authors used a simplified form of the Navier-Stokes equation for flow within the lumen and applied Darcy's law to the surrounding annulus of tissue, which was treated as a porous medium. The convective flow profiles were solved using the coupled momentum and continuity equations in both the lumen and the shell. A primary weakness of this model is that it is limited to a closed-shell system in which the shell side is densely packed with cells. The assumption of very little, or no radial convection at all, makes this model one-dimensional. Salmon *et al.* (1988) showed that radial recirculation flow could indeed have a significant effect on the performance of hollow-fibre bioreactors. An open-shell system has even more significant radial gradients and a different modelling approach is needed.

3.2.2 A general description of flow phenomena

Bruining (1989) presented a general model that predicts the pressures and flow rates in HFMMs for different modes of operation. These are DE filtration, CF filtration, closed-shell mode and CF filtration with suction of permeate for backwash (Yuan & Finkelstein, 1956). Each of these modes is characterised by the fraction retentate, F, as follows:

F = 0	Dead-end
0 < F < 1	Cross-flow
F = 1	Closed-shell
F > 1	Cross-flow with permeate suction

Bruining (1989) performed numerical experiments with laminar and turbulent flows inside the fibres and constant and varying shell side pressures. By using an overall mass-balance, his analysis shows how the flows and pressures are interrelated for the different modes of operation, and how they depend on the system's physical properties. According to this model, only two dimensionless parameters are needed to predict the flows and pressures. These are the so-called transport modulus, T_L, and the dimensionless flow rate parameter inside the fibre, Ψ. T_L represents the ratio of viscous flow resistance in the fibres and the fibre wall permeation resistance, and is useful in determining the macroscopic performance of a membrane module. Ψ is related to the entrance flow and its physical properties. Bruining (1989) derived the following relation between F, T_L and Ψ:

$$\Psi_0 = \frac{\sqrt{T_L}\sinh\left(\sqrt{T_L}\right)}{\cosh\left(\sqrt{T_L}\right) - F} \qquad [3.1]$$

Ψ_0 is the dimensionless entrance flow rate and T_L is given by:

$$T_L = \frac{128KL^2}{d_i^3 d_w} \text{ (lumen side)} \qquad [3.2]$$

where K is the fibre wall permeability, L is the fibre length, d_i is the inner fibre diameter and d_w is the fibre wall thickness.

The fraction retentate is the ratio between exit and entrance dimensionless flow rate inside the fibre and is given by:

$$F = \frac{\Psi_1}{\Psi_0} \qquad [3.3]$$

For each combination of T_L and Ψ_0, the corresponding operating mode can be predicted by determining the value of F in eqn. [3.1]. Fig. 10 shows the different operating modes for various combinations of T_L and Ψ_0.

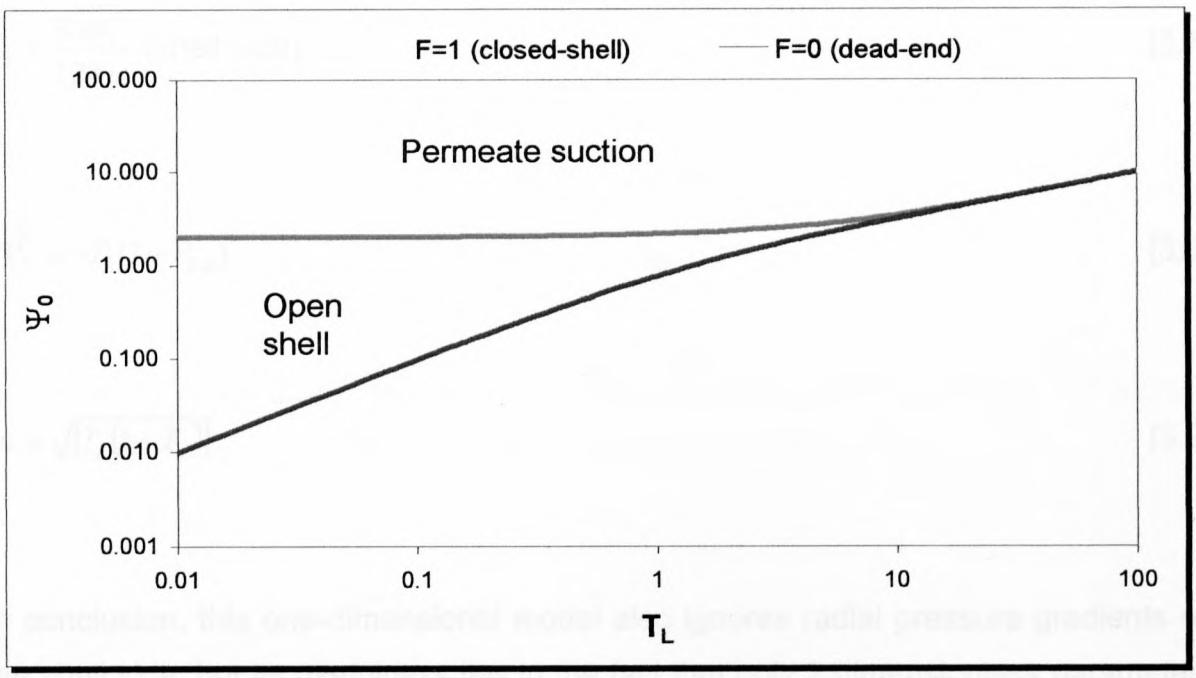

Fig. 10 : Modes of operation for hollow fibre devices.

For laminar flow inside the fibres and a pressure drop on the shell side, Bruining (1989) obtained the following solutions for the dimensionless flow rate inside the fibre, Ψ, and the lumen and shell pressures:

$$\Psi = \frac{\Psi_0'}{1+T_S}\left[T_S + \cosh(aX)\right] + \frac{\Psi_0'}{a}\sinh(aX) \qquad [3.4]$$

$$P_L = \frac{\Psi_0'}{1+T_S}\left[-T_S - \frac{\sinh(aX)}{a}\right] + \frac{\Psi_0'}{a^2}\left[\cosh(aX) - 1\right] + 1 \qquad [3.5]$$

$$P_S = \frac{\Psi_0'}{1+T_S}\left[-T_S - \frac{\sinh(aX)}{a}\right] + \frac{\Psi_0' T_S}{a}\left[1 - \cosh(aX)\right] + P_{S,0} \qquad [3.6]$$

where

$$T_S = \frac{k_1 \pi d_i^4}{128\mu} \text{ (shell side)} \qquad [3.7]$$

$$\Psi_0' = -T_L(1 - P_{S,0}) \qquad [3.8]$$

$$a = \sqrt{\left[T_L(1+T_S)\right]} \qquad [3.9]$$

In conclusion, this one-dimensional model also ignores radial pressure gradients on the shell side, but its usefulness lies in the fact that only 2 dimensionless parameters are needed to predict all the pressures and flows for the different modes of operation. The analysis is particularly suited to the general case of laminar or turbulent flow in porous ducts.

3.2.3 A theoretical analysis of convective flow profiles

The convective flow analysis in a hollow-fibre membrane bioreactor developed by Kelsey *et al.* (1990) is also based on flow through an average representative fibre, called the Krogh cylinder. Although some previous analyses (Kleinstreuer & Agarwal, 1986; Salmon *et al.*, 1988) showed that radial convection could dramatically influence the performance of HFMMs, none of those were able to model the convective recirculation flow within such devices. In Kelsey *et al.*'s investigation, flow on the shell side was assumed to be unobstructed by biocatalyst and was described by the Navier-Stokes equations rather than Darcy's law, as in the model of Apelblat *et al.* (1974). The analysis started off with the dimensionless continuity and momentum equations for steady-state flow in the lumen and shell sides:

$$\frac{\partial U}{\partial X}+\frac{1}{R}\frac{\partial(RV)}{\partial R}=0 \qquad [3.10]$$

$$\frac{1}{R}\frac{\partial}{\partial R}\left(R\frac{\partial U}{\partial R}\right)=\frac{dP}{dX} \qquad [3.11]$$

and yields the following dimensionless coupled second-order ordinary differential equations after applying the necessary boundary conditions:

$$\frac{d^2P_L}{dX^2}=16\kappa\left(P_L-P_S\right) \qquad [3.12]$$

$$\frac{d^2P_S}{dX^2}=-\frac{16\kappa}{\gamma}\left(P_L-P_S\right) \qquad [3.13]$$

where

$$\kappa = \frac{L_p L_{eff}^2}{r_L^3} \qquad [3.14]$$

$$\gamma = \left(\frac{r_M}{r_L}\right)^4 \left[4\left(\frac{r_S}{r_M}\right)^4 \ln\left(\frac{r_S}{r_M}\right) + 4\left(\frac{r_S}{r_M}\right)^2 - 3\left(\frac{r_S}{r_M}\right)^4 - 1 \right] \qquad [3.15]$$

Note that L_p is the hydraulic membrane permeability and L_{eff} is the effective filtration length.

A combination of equations [3.12] and [3.13] leads to the steady-state analytical solutions for the lumen and shell side pressures:

$$P_L(X) = B_1 \sinh(\lambda X) + B_2 \cosh(\lambda X) + B_3 X + B_4 \qquad [3.16]$$

$$P_S(X) = -\frac{B_1}{\gamma} \sinh(\lambda X) - \frac{B_2}{\gamma} \cosh(\lambda X) + B_3 X + B_4 \qquad [3.17]$$

where

$$\lambda = \frac{16\kappa(\gamma + 1)}{\gamma} \qquad [3.18]$$

$$B_1 = \frac{-4\gamma}{\lambda(\gamma + 1)} \qquad [3.19]$$

$$B_2 = \frac{-4\gamma}{\lambda(\gamma+1)\sinh(\lambda)}\left[1-\cosh(\lambda)-\frac{f(\gamma+1)}{\gamma}\right] \quad [3.20]$$

$$B_3 = \frac{-4}{\gamma+1} \quad [3.21]$$

$$B_4 = P_{L,0} + \frac{4\gamma}{\lambda(\gamma+1)\sinh(\lambda)}\left[1-\cosh(\lambda)-\frac{f(\gamma+1)}{\gamma}\right] \quad [3.22]$$

These solutions are in terms of three dimensionless parameters: γ describes the geometry of the fibres, κ is the membrane permeability and f is the filtration fraction.

The model can be used to study axial flow and pressure variations for the same operational modes investigated by Bruining (1989). Additional work was done to describe convective recirculation flow, by developing axial and radial velocity profiles. Since pressure is only a function of X, eqn. [3.11] can be integrated twice with respect to R in both the lumen and shell to give the following expressions for the axial (U) and radial (V) velocities in the lumen and shell:

$$U_L(R,X) = -\frac{1}{4}(1-R^2)\frac{dP_L}{dX} \quad [3.23]$$

$$U_S(R,X) = -\frac{1}{4}\left[2\beta^2\ln\left(\frac{R}{\alpha}\right)-R^2+\alpha^2\right]\frac{dP_S}{dX} \quad [3.24]$$

$$V_L(R,X) = \frac{R}{16}(2-R^2)\frac{d^2P_L}{dX^2} \quad [3.25]$$

$$V_S(R,X) = -\frac{R \cdot \xi(R)}{16}\frac{d^2 P_S}{dX^2} \qquad [3.26]$$

where

$$\alpha = \frac{r_M}{r_L} \qquad [3.27]$$

$$\beta = \frac{r_S}{r_L} \qquad [3.28]$$

$$\xi(R) = 2\left(\beta^2 - \alpha^2\right) + R^2 - \frac{3\beta^4}{R^2} + \frac{2\alpha^2\beta^2}{R^2} + \frac{4\beta^4}{R^2}\ln\left(\frac{\beta}{\alpha}\right) - 4\beta^2 \ln\left(\frac{R}{\alpha}\right) \qquad [3.29]$$

The axial and radial velocity profiles in the lumen, membrane wall and shell are shown in figs. [11] and [12], for a module with length 1.2m and outer diameter 90mm.

The axial velocity profile is parabolic in the lumen with the maximum at the centreline, while it is zero in the fibre wall. From the graph is is clear the velocity in the shell side is much slower compared to that in the lumen. Also, the lumen velocity has its maximum at the inlet (at X = 0). The radial velocity, or filtrate flux, is zero at the lumen centreline and interface between the fibres, while it obtains its maximum value at a distance $\sqrt{2/3}$ of the lumen radius, or 0.8165R. This maximum can easily be obtained by examining the equation for $V_L(R, X)$:

$$V_L(R,X) = \frac{R}{16}\left(2 - R^2\right)\frac{d^2 P_L}{dX^2} \qquad [3.25]$$

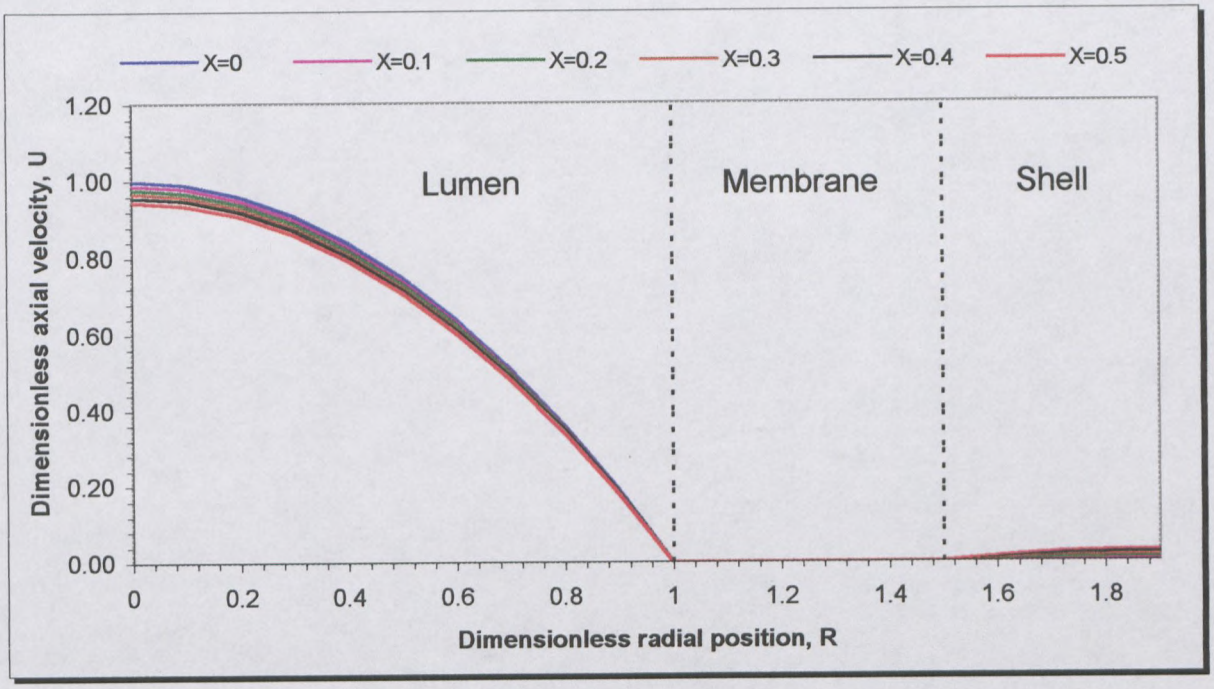

Fig. 11 : Axial velocity profiles in a hollow-fibre membrane module.

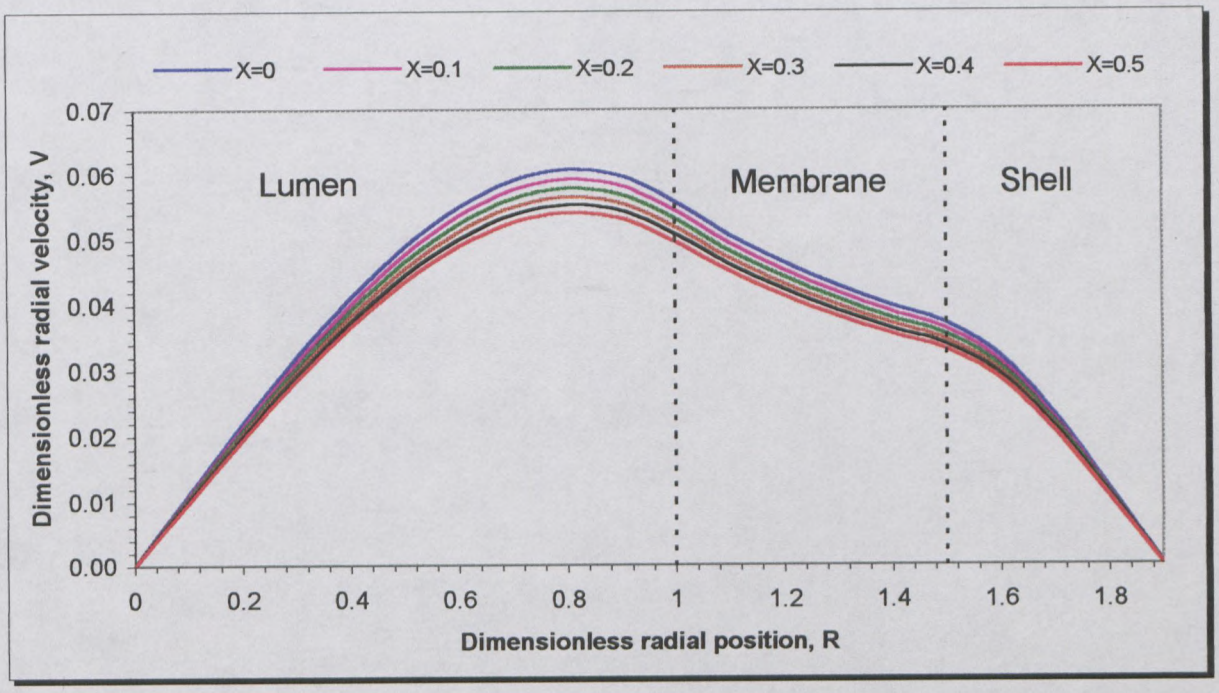

Fig. 12 : Radial velocity profiles in a hollow-fibre membrane module.

The radial dependence is given by :

$$\frac{R}{16}\left(2 - R^2\right) \qquad [3.30]$$

By differentiating this expression with respect to R and setting the resulting derivative equal to zero, we get :

$$\frac{d}{dR}\left[\frac{R}{8} - \frac{R^3}{16}\right] = 0 \qquad [3.31]$$

which yields the following maximum value for R :

$$R = \sqrt{\frac{2}{3}} \qquad [3.32]$$

These velocity profiles were used to study flow streamlines and the extent of recirculation. Since this model is particularly useful for hollow-fibre bioreactors, the residence time distribution (RTD) for the closed-shell operation was also studied. The RTD was found to be bimodal, with two distinct peaks. The first peak is associated with the fluid that remains inside the lumen as it passes down the fibre, while the second peak represents the fluid that passes through the membrane and travels part of the way on the shell side. Kelsey *et al.* (1990) showed that as the membrane becomes more permeable (i.e. κ increases), the magnitude of the first peak decreases while that of the second peak increases, due to more recirculation flow.

Although this model was also based on one representative fibre and ignored radial pressure gradients, its analytical solution makes it an easy-to-use model.

3.2.4 Analysing laminar fluid flow in porous tube systems

Yet another attempt to model fluid flow through a porous tube and shell system, was conducted by Pangrle *et al.* (1991). The Navier-Stokes equations were used to describe flows in the lumen and shell sides, while Brinkman's equation (Brinkman, 1947) was employed for flows in the porous tube wall. The momentum and mass conservations equations were coupled together with Brinkman's equation in order to model the flow phenomena in the three flow regions of a 2-D, axisymmetric tube and shell system. The Galerkin finite element method (FEM) was used to obtain the model predictions and these were compared to experimental results with the aid of magnetic resonance imaging measurements. It was found that the experimental results were in good agreement with the FEM predictions, justifying the validity of the numerical model. However, although the authors tried to make fewer simplifying assumptions to the governing equations than previous models, the model was still based on a single representative fibre and could not account for shell side flows within the fibre bundle.

3.2.5 A physical experimental approach

The separation of plasma from blood using a HFMM was investigated by Yoshikawa *et al.* (1992, 1994). Where previous researchers concentrated on a theoretical analysis, this work included physical experiments using pure water as a first step. The Hagen-Poiseuille and Carman-Kozeny equations were used for the axial pressure gradients and flow rates respectively, but once again, radial pressure gradients were neglected. Thus this model becomes equivalent to the previous KCMs. Additional information concerning dead space on the shell side was obtained by performing an impulse response test. KCl was injected to the feed stream as a tracer and the changes in concentration at the lumen and shell side outlets were measured as a function of time. The residence time distribution revealed the existence of dead space, which causes liquid to stagnate in the space among

densely packed fibres. This resulted in a negative influence on permeation, which suggests that too great a packing density is disadvantageous.

3.2.6 The need for a 2-D model

The primary weakness of all the above-mentioned models is the lack of incorporation of *interfibre flows* in the shell side, as well as very small *radial pressure gradients*. Park & Chang (1986) also demonstrated that not all fibres in the fibre bundle are supplied with the same feed flow, due to the shape of the lumen manifold. They found that with a cylindrical manifold, the highest velocity occurs in the fibre located *at* the centre of the fibre bundle and the lowest velocity occurs in the fibres *around* the centre, resulting in a non-uniform pressure distribution. With a conical manifold a relatively uniform pressure distribution may be obtained by using a large pressure drop parameter, a small Reynolds number and a large manifold height. This will ensure that the velocities are more or less the same everywhere. A residence time distribution (RTD) study revealed that fluid in the centre fibres passes the bundle faster than fluid in the fibres in the outer region. The RTD also confirmed that the velocity distributions in the manifolds are in good agreement with the theoretical predictions. In addition, since the hydrophilic fibres *expand when wetted*, they assume a wavy appearance, because they are fixed at both ends of the module. Hence the Krogh cylinder approach might be inaccurate and different modelling techniques are required.

Thus for these two reasons (interfibre flows and wet fibre expansion) we would want a model that incorporates radial gradients. This would also be important for any shell features that were not one-dimensional, like permeate outlets. Furthermore, the model can be extended to cope with any other detail of module design or variation of system parameters. In this study, parameters like membrane permeability and fluid viscosity were assumed to be constant, but they can be rendered space and/or time dependent for an even more rigorous hydrodynamic analysis.

In 1995, Labecki *et al.* (1995) proposed a new model, the porous medium model (PMM), which encompasses all fibres and has a spatial domain corresponding to the actual dimensions of the entire module. The most important feature of this model is

that it can easily be extended to account for any detail of module design, such as the positioning of permeate outlets, as well as dealing with operating modes that produce significant radial pressure gradients. The next section deals with the derivation of the model.

3.3 THE POROUS MEDIUM MODEL

3.3.1 The mathematics of porous media flow

Labecki *et al.* (1995) treated the lumen and shell sides as two interpenetrating porous regions with a continually, spatially dependent, source/sink of incompressible fluid. Since the Reynolds numbers of the flows in and around the fibres are laminar (Re < 2 000; De Nevers, 1991), Darcy's Law for flow in porous media (Bird *et al.,* 1960) is used:

$$\underline{V} = -\frac{\underline{\underline{k}}}{\mu}\left(\nabla p - \rho \underline{g}\right) \qquad [3.33]$$

where $\underline{V}$ is the superficial velocity vector, $\underline{\underline{k}}$ is the Darcy permeability tensor, μ is the fluid viscosity, ∇p is the pressure gradient, ρ is the fluid density and $\underline{g}$ is the gravitational vector. Using cylindrical co-ordinates and neglecting angular effects, this becomes

$$\underline{V}_L = -\frac{1}{\mu}\left(k_{r,L}\left(\frac{\partial p_L}{\partial r} - \rho g_r\right);\ k_{x,L}\left(\frac{\partial p_L}{\partial x} - \rho g_x\right)\right) \qquad [3.34]$$

for the lumen, and

$$\underline{V}_S = -\frac{1}{\mu}\left(k_{r,S}\left(\frac{\partial p_S}{\partial r} - \rho g_r \right);\ k_{x,S}\left(\frac{\partial p_S}{\partial x} - \rho g_x \right) \right) \qquad [3.35]$$

for the shell. When looking at the lumen, it is clear that the fibres are not directly connected to each other, thus the averaged lumen flow is one-dimensional, yielding

$$\underline{V}_L = -\frac{1}{\mu}\left(k_{x,L}\left(\frac{\partial p_L}{\partial x} - \rho g_x \right);\ 0 \right) \qquad [3.36]$$

or

$$\underline{V}_L = V_{L,x} = -\frac{1}{\mu} k_{x,L}\left(\frac{\partial p_L}{\partial x} - \rho g_x \right) \qquad [3.37]$$

Applying an overall mass balance to the lumen and shell sides and incorporating a fluid source/sink term, ϕ, Labecki *et al.* (1995) derived an alternative form of the continuity law:

$$\nabla \cdot \underline{V}_L = -\phi \quad \text{for the lumen} \qquad [3.38]$$

and

$$\nabla \cdot \underline{V}_S = \phi \quad \text{for the shell.} \qquad [3.39]$$

The fluid source/sink term is due to the filtration of fluid through the incompressible membrane. Fluid that disappears from the lumen ($-\phi$) must instantly appear on the shell side ($+\phi$), and *vice versa*. ϕ is equivalent to the transmembrane pressure and is given by

$$\phi = \frac{L_p A_v}{\mu}(p_L - p_S) \qquad [3.40]$$

where L_p is the hydraulic permeability of the membrane, A_v is the membrane surface area per unit volume available for filtration and p_L and p_S are the lumen and shell hydrostatic pressures. A combination of eqs. [3.37] with [3.38] and [3.35] with [3.39] yields the following pair of coupled partial differential equations (PDEs) for p_L and p_S as functions of r and x:

$$k_{x,L}\frac{\partial^2 p_L}{\partial x^2} = L_p A_v(p_L - p_S) \qquad [3.41]$$

and

$$-k_{r,S}\frac{1}{r}\frac{\partial}{\partial r}\left(r\frac{\partial p_S}{\partial r}\right) - k_{x,S}\frac{\partial^2 p_S}{\partial x^2} = L_p A_v(p_L - p_S) \qquad [3.42]$$

These two equations cannot be solved by analytical methods. Numerical methods, like the finite difference method (FDM) or the finite element method (FEM), have to be used. This will be looked at in the next chapter.

3.3.2 The computational domain and boundary conditions

Labecki *et al.*'s (1995) hollow-fibre system is a cylindrical cartridge with a bundle of hollow-fibres inside it. These fibres are fixed in epoxy at both ends of the cartridge, with their lumina opening into upstream and downstream manifolds. The space between the fibres is called the shell side or extracapillary space (ECS). Fluid enters or leaves the ECS through upstream and downstream manifolds in a radial direction, normal to the fibre bundle. The lumen flow is axial or parallel to the fibres. Since the hollow-fibre system is axisymmetric only one half needs to be considered for modelling purposes. Fig. 13 shows what the physical device looks like, while fig. 14

displays the computational domain and boundaries. The different boundary conditions are set out in table 3.

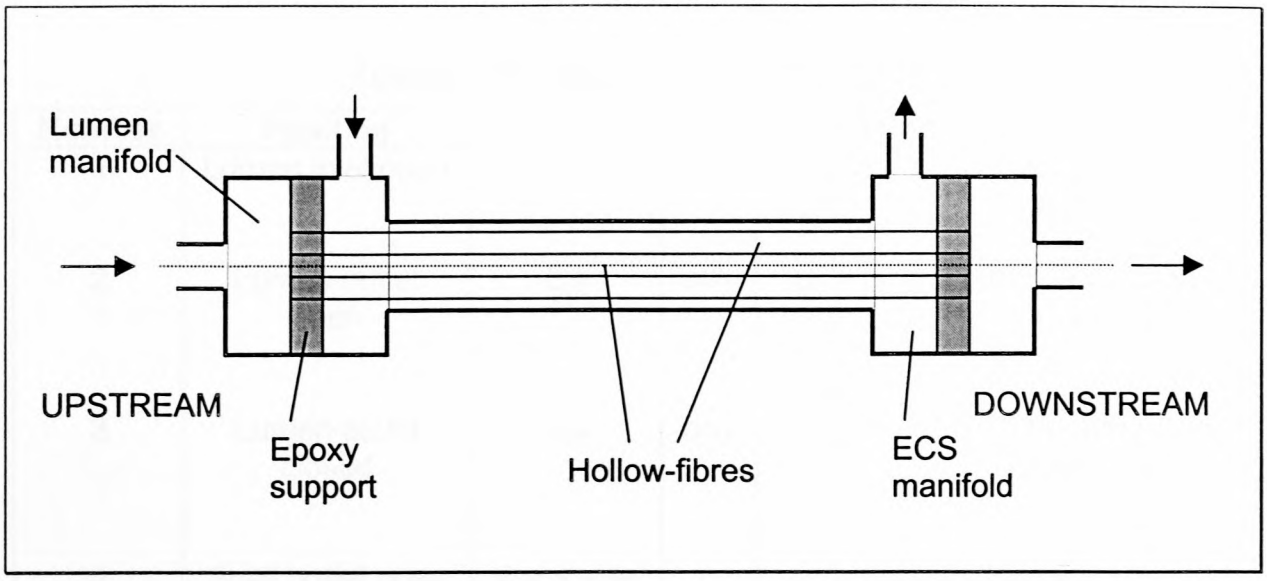

Fig. 13 : Diagram of physical membrane module.

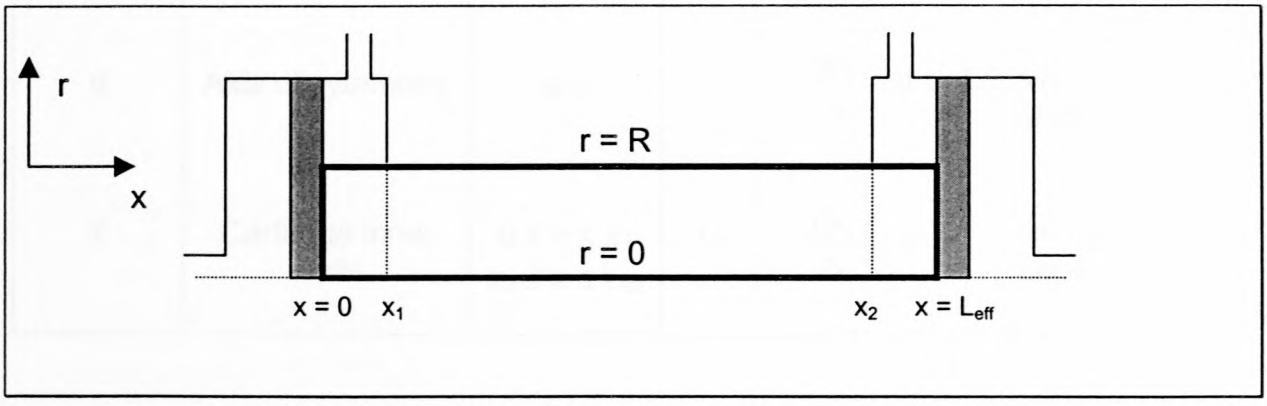

Fig. 14 : Diagram of computational domain.

The *x* co-ordinate is used down the axis of the membrane module, while the *r* co-ordinate is used for the radial direction. For CF UF, the lumen inlet and outlet pressures are known, as well as the shell outlet pressure. When the DE filtration mode is used, the lumen outlet is blocked, which means there is no fluid flux across that boundary. The result is a zero pressure gradient on the lumen side in the x-direction, or $\frac{\partial p_L}{\partial x} = 0$. At the inside walls of the cartridge, as well as at the axis of

symmetry, there is no fluid flux across the boundary, hence the pressure gradient on the shell side in the axial and radial directions is zero, or $\frac{\partial p_S}{\partial x} = 0$ and $\frac{\partial p_S}{\partial r} = 0$.

Table 3 : Boundary conditions for HFMM

Number	Position	X	r	Condition	Explanation
1	Lumen inlet open	0	any	$p_L = p_{L,in}$	Known inlet pressure
2	Lumen outlet open	L_{eff}	any	$p_L = p_{L,out}$	Known outlet pressure
3	Lumen outlet closed	L_{eff}	any	$\frac{\partial p_L}{\partial x} = 0$	No axial lumen flux
4	Shell outlet open	$x_1 \le x \le x_2$	r_c	$p_S = p_{S,out}$	Known outlet pressure
5	Shell side module ends	0; L_{eff}	any	$\frac{\partial p_S}{\partial x} = 0$	No axial shell flux
6	Axis of symmetry	any	0	$\frac{\partial p_S}{\partial r} = 0$	No radial shell flux
7	Cartridge inner walls	$0 \le x \le x_1$ $x_2 \le x \le L_{eff}$	r_c	$\frac{\partial p_S}{\partial r} = 0$	No radial shell flux

3.3.3 Model parameters

The permeability of the membranes was determined using the PMM and is calculated by

$$L_p = \frac{\mu Q}{A \Delta p_m} \qquad [3.43]$$

where Q is the experimental transmembrane flow rate, or permeation flow rate, A is the total membrane surface area and Δp_m is the transmembrane pressure drop. The complete procedure is described in section 5.3. Labecki *et al.* (1995) made a number of assumptions in choosing expressions for the lumen and shell Darcy permeabilities in the axial and radial directions, because they needed only approximate values to demonstrate the applicability of their model.

- The axial permeabilities, $k_{x,L}$ and $k_{x,S}$, were obtained from a one-dimensional analysis of the laminar Krogh cylinder flow, with the necessary modifications to account for wet fibre expansion.

- Both the lumen and shell *axial* permeabilities, $k_{x,L}$ and $k_{x,S}$, are affected in the same manner by a tortuosity factor, $\tau = \left(\frac{L_{eff}}{L_{wet}}\right)^2$ (Carman, 1937).

- The *radial* permeability in the shell side, $k_{r,S}$, is not influenced by tortuosity.

- Consequently the model deals with only one tortuosity component.

- The shell side radial permeability, $k_{r,S}$, is based on Happel's (1959) expression for flow perpendicular to an array of parallel cylinders.

- The lumen radial permeability, $k_{r,L}$, can be set to zero, because the averaged lumen flow is one-dimensional, as discussed in section 3.3.1.

The above assumptions lead to the following expressions for the permeabilities:

$$k_{x,L} = \frac{N r_L^4 \sqrt{\tau}}{8 r_c^2} \qquad [3.44]$$

$$k_{x,S} = \frac{r_m^2 \tau}{4\varphi}\left(-\ln\varphi - \frac{3}{2} + 2\varphi - \frac{1}{2}\varphi^2\right) \qquad [3.45]$$

$$k_{r,S} = \frac{r_m^2}{4\varphi}\left(-\ln\varphi + \frac{\varphi^2 - 1}{\varphi^2 + 1}\right) \quad \text{(Happel, 1959)} \qquad [3.46]$$

where N is the number of fibres, r_L is the lumen radius, r_c is the cartridge inner radius, τ is the tortuosity factor and φ is the fibre volume fraction, given by:

$$\varphi = \frac{N r_M^2 L_{wet}}{r_C^2 L_{eff}} \qquad [3.47]$$

3.4 COMPARISON BETWEEN THE KCM AND PMM

Since the KCM neglects radial effects, it is a one dimensional (1-D) model, whereas the PMM, as used by Labecki *et al.* (1995) is a 2-D model, but it could easily be extended to 3 dimensions. Labecki *et al.* compared the results of their PMM to that of Bruining's (1989) and Kelsey *et al.*'s (1990) models for the DE and CF filtration modes. In order to do this, the original models of Bruining (1989) and Kelsey *et al.* (1990) had to be rederived using pressure boundary conditions and including wet fibre expansion effects. For open inlet or outlets, a known pressure value is specified. A zero axial pressure derivative is imposed for closed outlets. The axial coordinate, x, is replaced by σ to include wet fibre expansion:

$$\sigma = \frac{x L_{wet}}{L_{eff}} \qquad [3.48]$$

A summary of the equations for the models of Bruining (1989) and Kelsey *et al.* (1990) is given in table 4, with the base parameters listed below the table.

If one looks at the governing equations of the PMM, eqns. [3.41] and [3.42], it is clear that when the radial terms are neglected, the PMM becomes identical to the 1-D KCM governing equations. Labecki *et al.* (1995) compared the inlet and outlet flow rate predictions by the PMM to that predicted by the models of Kelsey *et al.* (1990) and Bruining (1989) as functions of membrane permeability. Figs. 15 and 16 show these results for a module with the following parameters:

Number of fibres	*8128*
Effective filtration length	*0.215m*
Wet fibre length	*0.238m*
Inner fibre radius	1.15×10^{-4} *m*
Outer fibre radius	1.24×10^{-4} *m*
Module inner radius	*0.01575m*
Pressure drop ($P_{L,0} - P_{L,1}$ *and* $P_{L,0} - P_{S,1}$)	*10 kPa*

Permeate was withdrawn from the downstream ECS manifold.

Table 4 : Equations for the 1-D models of Bruining (1989) and Kelsey *et al.* (1990)

	Bruining	**Kelsey *et al.***
Governing equations	$\frac{d^2 p_L}{d\sigma^2} = \frac{16 L_p}{R_L^3}(p_L - p_S)$ Constant shell pressure	$\frac{d^2 p_L}{d\sigma^2} = \frac{16 L_p}{R_L^3}(p_L - p_S)$ $\frac{d^2 p_S}{d\sigma^2} = -\frac{16 L_p}{R_L^3}\frac{1}{\gamma}(p_L - p_S)$
Pressure solutions	$P_L(\sigma) = P_{S,1} + A_1 \sinh(\theta\sigma) + A_2 \cosh(\theta\sigma)$ $P_S(\sigma)$ = constant	$P_L(\sigma) = B_1 \sinh(\lambda\sigma/L_{wet}) + B_2 \cosh(\lambda\sigma/L_{wet}) + B_3\sigma/L_{wet} + B_4$

Table 4 (continued)

	Bruining	Kelsey *et al.*
Flow rates	$Q_{L,0} = -\beta A_1$ $Q_{L,1} = -\beta[A_1 \cosh(\theta L_{wet}) + A_2 \sinh(\theta L_{wet})]$ $Q_{S,1} = \beta\{A_1[\cosh(\theta L_{wet})-1] + A_2 \sinh(\theta L_{wet})\}$	$Q_{L,0} = \alpha(\lambda B_1 + B_3)$ $Q_{L,1} = \alpha[\lambda B_1 \cosh(\lambda) + \lambda B_2 \sinh(\lambda) + B_3]$ $Q_{S,0} = \alpha(-\lambda B_1 + \gamma B_3)$ $Q_{S,1} = \alpha[-\lambda B_1 \cosh(\lambda) - \lambda B_2 \sinh(\lambda) + \gamma B_3]$

The subscripts 0 and 1 denote the axial positions $\sigma = 0$ and $\sigma = L_{wet}$ respectively.

Parameters for Bruining's (1989) model

$$\beta = \frac{N\pi r_L^3}{2\mu}\sqrt{\frac{L_p}{r_L}} \qquad [3.49]$$

$$\theta = 4\sqrt{\frac{L_p}{r_L^3}} \qquad [3.50]$$

$$A_1 = -(P_{L,0} - P_{S,1})\frac{\sinh(\theta L_{wer})}{\cosh(\theta L_{wet})} \quad \text{OR} \quad A_1 = \frac{P_{L,1} - P_{S,1} - (P_{L,0} - P_{S,1})\cosh(\theta L_{wet})}{\sinh(\theta L_{wet})} \qquad [3.51]$$

DEAD-END MODE CROSS-FLOW MODE

$$A_2 = P_{L,0} - P_{S,1} \qquad [3.52]$$

Parameters for Kelsey *et al.*'s (1990) model

$$\alpha = -\frac{N\pi r_L^4}{8\mu L_{wet}} \qquad [3.53]$$

$$\lambda = 4\sqrt{\frac{\kappa(\gamma+1)}{\gamma}} \qquad [3.54]$$

$$\kappa = \frac{L_p L_{wet}^2}{r_L^3} \qquad [3.55]$$

$$\gamma = \left(\frac{r_M}{r_L}\right)^4\left[4\left(\frac{r_S}{r_M}\right)^4 \ln\left(\frac{r_S}{r_M}\right) + 4\left(\frac{r_S}{r_M}\right)^2 - 3\left(\frac{r_S}{r_M}\right)^4 - 1\right] \qquad [3.56]$$

Fig. 15 shows the results of the inlet flow rate predictions, for the DE and CF filtration modes. At low L_p values, the DE curves approach zero for all models, as expected. The CF curves also exhibit asymptotic behaviour as the membrane becomes more impermeable and they converge to a value of 2.34×10^{-5} m^3/s. The Hagen-Poiseuille equation can also be used to calculate this asymptotic value for impermeable fibres. At the higher end of the permeability scale, the DE and CF curves as predicted by the KCM model of Kelsey *et al.* (1990) approach the asymptotic value of 3.2×10^{-5} m^3/s. This can be explained by the fact that the transmembrane pressure at high permeabilities becomes almost zero, which in turn means that fluid will travel over the same distance, whether in the lumen or in the shell. The PMM curves also converge at high permeabilities because the Darcy permeabilities, $k_{x,L}$, $k_{x,S}$ and $k_{r,S}$ are of the same order of magnitude. However, the PMM curves converge to a slightly higher asymptotic value of 3.4×10^{-5} m^3/s because of the incorporation of a radial term to account for radial pressure variations.

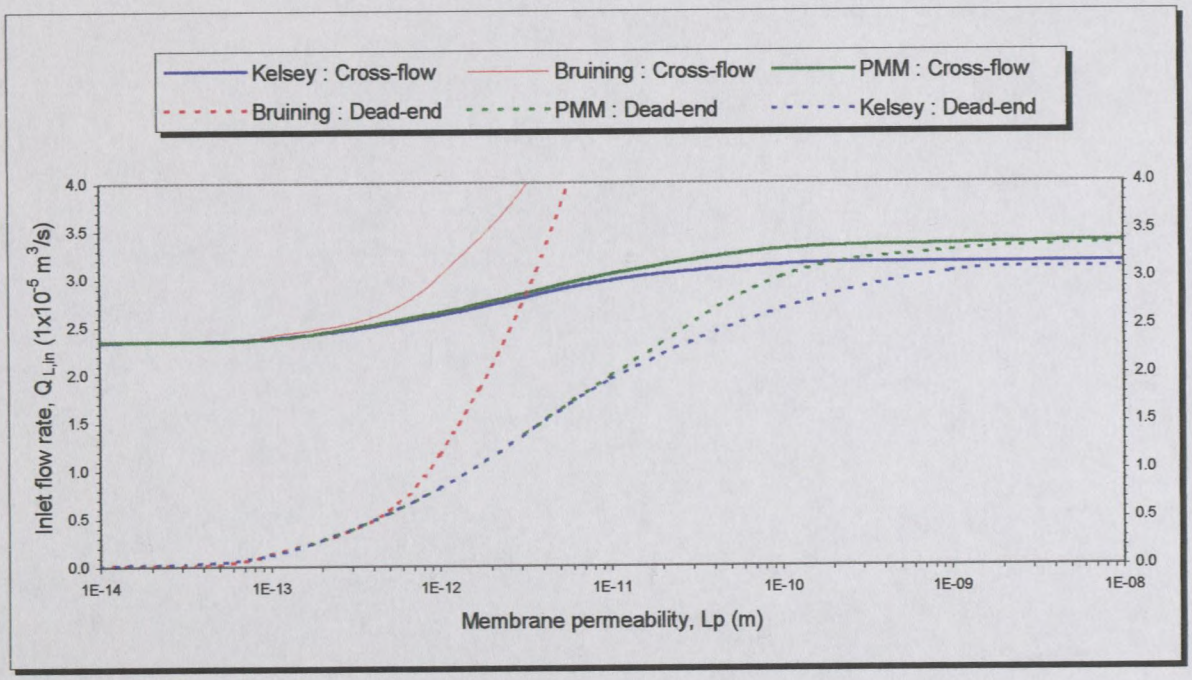

Fig. 15 : Inlet flow rate prediction by various hydrodynamic models (reproduced from Labecki *et al.*, 1995).

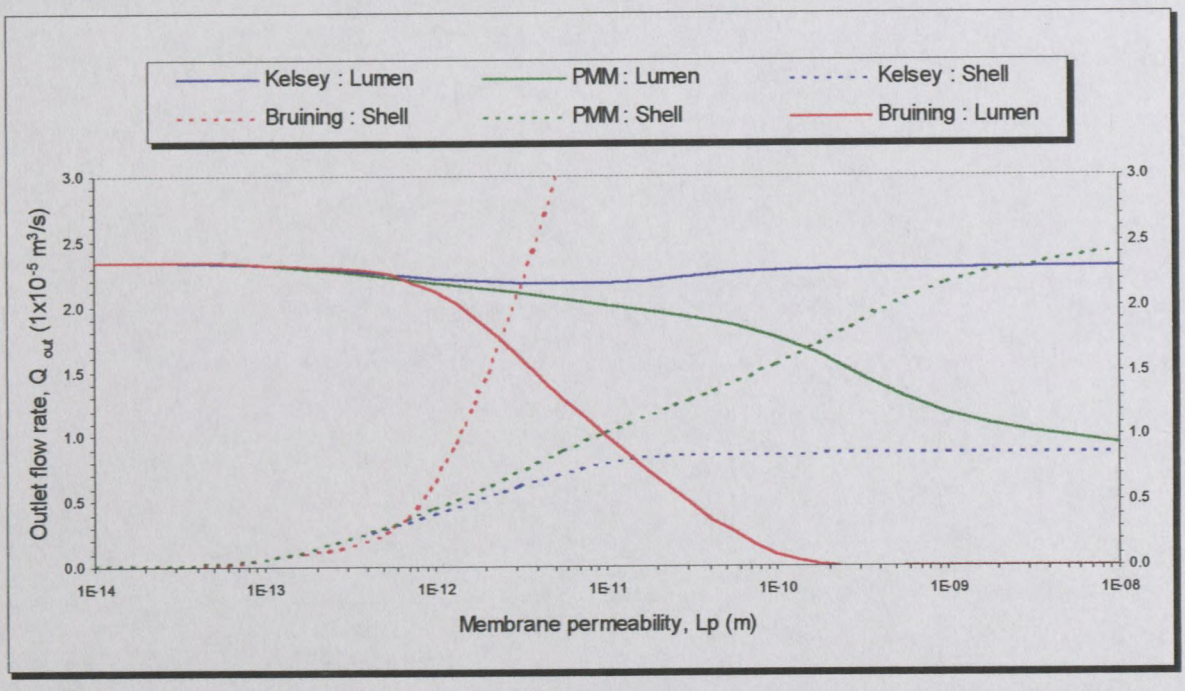

Fig. 16 : Outlet flow rate prediction by various hydrodynamic models (reproduced from Labecki *et al.*, 1995).

In Bruining's (1989) model, the curves approach infinity as the permeability increases. This is because the shell side pressure is assumed to be constant and that the ECS acts as a fluid sink.

The outlet flow rate curves in fig. 16 also exhibit asymptotic behaviour. The lumen flow rate as predicted by Kelsey *et al.* (1990) approaches the same value of 2.34×10^{-5} m^3/s at both low and high permeabilities. At low L_p values all the fluid remains inside the lumen and the Hagen-Poiseuille equation is applicable. At high L_p values the membrane offers almost no resistance to flow and the lumen and shell side pressures are the same everywhere. The Hagen-Poiseuille equation can again be used to calculate the flow rate. At intermediate values for L_p more fluid passes to the shell side as L_p increases, leading to a slight decrease in the lumen outlet flow. A minimum value of 2.18×10^{-5} m^3/s is achieved at an L_p value of 1×10^{-11} m. The ECS outlet flow rate is the difference between the lumen inlet and outlet flow rates. The outlet flow rates predicted by the PMM differ considerably from the KCM models at higher L_p values. This can be attributed to the fact that the 1-D KCM models do not take radial flow into account and fluid leaves the ECS manifolds in an axial direction. This is of course only possible in theory. The 2-D PMM model allows for radial outflow from the ECS manifolds.

All three models produce more or less the same results for L_p values up to 1×10^{-13} m, while the results obtained with the model of Kelsey *et al.* (1990) equals that of the PMM for L_p values up to 1×10^{-12} m. As an L_p value of 2.3×10^{-13} m is used in this project, as will be shown later, either Kelsey *et al.*'s model or the PMM can be used. However, the choice falls on the PMM, as it is much more flexible should one wish to change any features of the module design, or use more permeable membranes.

~~~
~~~

Chapter 4

THE FINITE ELEMENT METHOD AND *FASTFLO*

4.1 COMPUTATIONAL FLUID DYNAMICS

Fluid mechanics is the study of forces and motion in fluids, where the fluid can be a liquid or a gas. There is a widespread application of fluid mechanics in the world around us and the subject can be split up into various subdivisions. A few of these are:

- *aerodynamics,* the study of air flow around automobiles, airplanes, etc.;
- *hydrodynamics,* the study of water flow in pipes, rivers, etc.;
- *hydrology,* the study of water flow in ground and other porous media; and
- *multiphase flow,* the study of flow phenomena in oil wells and chemical reactors.

Fluid mechanics has been studied since the time of Sir Isaac Newton. Theory and practice were always studied together, experiments being used to validate theoretical approximations. The wind-tunnel was the most common tool for doing experiments. This proved to be effective in simulating scaled-down versions of real world applications. However, with the advent of computers, it was found that there is a much more cost-effective alternative to wind tunnels, and computational fluid dynamics, or CFD, was born. According to Anderson (1995), CFD can be thought of as a "transportable wind tunnel". The computer program itself is analogous to the wind tunnel. The advantages of CFD over a wind tunnel are numerous. Some of these are:

- cheaper;
- lower energy consumption;
- simulation accessible to remote people;
- faster and more accurate solutions; and
- can simulate flow conditions not reproducible in a wind tunnel.

Fletcher (1991) mentions the improvement in computer hardware performance and the decrease in costs that aids the rapid growth in CFD. Today, complex problems such as weather prediction or the pressure distribution on the surface of aircraft can be calculated within minutes on a supercomputer.

All fluid flow is governed by three fundamental equations:

- conservation of mass (continuity equation);
- Newton's second law (momentum equation); and
- conservation of energy (energy equation).

These three equations are all in integral or partial derivative form. CFD is the procedure during which these equations are replaced by their discretized algebraic equivalents. These are then solved to obtain approximate solutions for the unknown variables at discrete points.

4.2 THE FINITE ELEMENT METHOD

The Finite Element Method (FEM) has been developed over the last thirty years for solving engineering problems by numerical techniques. According to Norrie & De Vries (1973), it is a particular class of approximation procedure, in which the subdivision of a region into subdomains or finite elements is an essential part of the procedure. Furthermore, it is a subclass of the method of trial functions. A detailed discussion of this method is beyond the scope of this thesis and the reader is referred to a gentle introduction on the subject by Henwood & Bonet (1996). However, the very basic ideas needs to be mentioned briefly.

In the finite element method, a real-life situation is converted to a mathematical model through PDEs. The physical shape of the object is represented as an element mesh on which boundary conditions such as pressures, temperatures and other loads are applied. For the solution of PDEs, we need to set the boundary conditions as to find a unique solution. There are three types of boundary conditions, viz Dirichlet, Neuman and Robin boundary conditions.

Dirichlet boundary conditions

The value of the solution is explicitly defined on the boundary (or part of it). For example the pressure at the inlet of a HFMM is set to a known, fixed value.

Neuman boundary conditions

The normal derivative of the solution is defined on the boundary. If we set the normal derivative of the pressure to zero, the pressure gradient across that boundary is zero. In order to find a unique solution, a Dirichlet boundary condition must be defined somewhere on the boundary of the domain.

Robin boundary conditions

A combination of the first two boundary conditions is called a Robin boundary condition. In this case the normal derivative of the solution and the value of the solution itself on the boundary are connected by a function. Typically, a PDE will involve a function $u(\underline{x})$ defined for all $\underline{x}$ in the domain with respect to some given boundary condition. The purpose of the method is to determine an approximation to the function $u(\underline{x})$.

This study was not concerned with the mathematics of the FEM, but rather with its application. Therefore only a brief description of the three main steps during the solution of a PDE with the FEM, will be given. First, the domain, on which the PDE should be solved, should be subdivided into subregions or cells, called finite elements. This subdivision is called discretization and creates a mesh. Depending on the dimension of the problem (1-D, 2-D or 3-D), the elements can be triangles, squares, rectangles, or tetrahedrons, cubes, or hexahedrons. Lower-order polynomials are used to approximate the solution, $u(\underline{x})$, of a PDE, on the local elements. For a triangular element in 2-D, the solution $u(\underline{x})$ at each of the corner nodes {i, j, k} have values of u_i, u_j and u_k. $u(\underline{x})$ is then approximated within the local element by

$$\bar{u} = \begin{bmatrix} \phi_i(x,y) & \phi_j(x,y) & \phi_k(x,y) \end{bmatrix} \begin{bmatrix} u_i \\ u_j \\ u_k \end{bmatrix}$$

where $\{\phi_i, \phi_j, \phi_k\}$ are interpolation functions. If the local element is the triangle with 3 nodes at (0,0), (1,0) and (1,1), then

$$\phi_1 = 1 - x$$
$$\phi_2 = x - y$$
$$\phi_3 = y$$

and the linear approximation to $u(\underline{x})$ in the element is

$$u(x,y) = \begin{bmatrix} 1-x & x-y & y \end{bmatrix} \begin{bmatrix} u_i \\ u_j \\ u_k \end{bmatrix}$$

In addition to 3-noded triangular elements, 6-noded triangles, with a quadratic approximation to $u(\underline{x})$, can also be used.

In step 2 the solution of the PDE is approximated by piece-wise continuous polynomials on each element. By substituting the characteristic form of $u(\underline{x})$ on the elements and applying the given boundary conditions, the PDE is discretized and split into a finite number of algebraic equations. The aim is to determine the unknown coefficients of the polynomials in such a way, that distance from the exact solution becomes a minimum. This is what makes the FEM essentially a variational minimization technique.

Lastly, the solution of the linear system of algebraic equations returns the approximation to $u(\underline{x})$. Since the number of elements is finite, we have reduced the problem of finding a continuous solution for our PDE to calculating the finite number of coefficients of the polynomials.

From the user's point of view, FEM is divided into three subareas, viz pre-processing, solving and post-processing.

1. **Pre-processing**. Here a mathematical model of the problem to be analysed, is created. The mathematical model is constituted as equations in a *matrix system*. Also, the physical shape of the object is drawn and boundary conditions are identified and stated, as applicable to each boundary of the element domain.

2. **Solving**. The matrix system is solved by a numerical process.

3. **Post-processing**. After the matrix system has been solved, the results are acquired. These can be numerical values or graphical representations, depending on the needs of the user. When graphic post-processing is desired, the results are projected on the original model.

The FEM provides a greater flexibility to model complex geometries than finite difference and finite volume methods do. The advancement in computer technology enables us to solve even larger system of equations, to formulate and assemble the discrete approximation, and to display the results quickly and conveniently. This has also helped the FEM to become a powerful tool. A more in depth discussion of the FEM can be found in literature (Connor & Brebbia, 1976; Carey & Oden, 1986).

4.3 CHOICE OF SIMULATION SOFTWARE

The two coupled PDEs, eqns. [3.41] and [3.42], cannot be solved by analytical methods. Several numerical methods exists for this purpose. One of these methods is the FEM, as discussed in the previous section. The Commonwealth Scientific and Industrial Research Organisation (CSIRO) in Australia, developed a computer program called *Fastflo* (CSIRO, 1997) for this purpose. *Fastflo* is a finite element package for the numerical solution of PDEs in two and three dimensions. It is very flexible because the finite element methodology can handle domains with complex shapes, and because it incorporates a high level language, *Fasttalk*, by which users specify and solve a broad range of PDEs.

4.3.1 Specification of the problem

Fasttalk is a high level language developed especially for *Fastflo*. It enables users to:

- specify PDEs;
- assign boundary conditions;
- carry out finite element operations such as assembly and solution of systems of equations;
- write macros or subroutines that contain frequently used *Fasttalk* instructions; and
- view results graphically.

Fastflo solves boundary value problems posed by at least one PDE and boundary conditions. Each PDE is represented by one *Fasttalk* statement. Problems are assembled by typing their name, along with some possible arguments. This generally produces a sparse left-hand side (LHS) matrix and a right-hand side (RHS) vector.

A more in-depth description of *Fastflo*'s features can be found in Appendix A.

~~~
~~~

Chapter 5

SOLUTION OF THE PDEs AND FLUX CALCULATIONS

5.1 SIMULATION OF FLOW THROUGH A HFMM

The finite element software will now be implemented to investigate the flow through a hollow-fibre membrane module, by solving eqs. [3.41] and [3.42]. Note that for the purpose of this study, it is assumed that only *pure water* is used, thereby eliminating the effects of flux decline due to concentration polarization and fouling. (The inclusion of CP and fouling will introduce time dependency, requiring a severe expansion of the problem file in a separate study.) All the variables will first be non-dimensionalised in order to scale them to similar orders of magnitude. This is necessary as the program file contains a combination of very large and very small dimensional numbers, which can make the numerical solution process unstable. Eqns. [3.41] and [3.42],

$$k_{x,L}\frac{\partial^2 p_L}{\partial x^2} = L_p A_v (p_L - p_S) \qquad [3.41]$$

and

$$-k_{r,S}\frac{1}{r}\frac{\partial}{\partial r}\left(r\frac{\partial p_S}{\partial r}\right) - k_{x,S}\frac{\partial^2 p_S}{\partial x^2} = L_p A_v (p_L - p_S) \qquad [3.42]$$

can be written in dimensionless form as

$$k_1 \frac{\partial^2 P_L}{\partial X^2} = La(P_L - P_S) \quad [5.1]$$

and

$$-k_2 \frac{1}{R}\frac{\partial}{\partial R}\left(R\frac{\partial P_S}{\partial R}\right) - k_3 \frac{\partial^2 P_S}{\partial X^2} = La(P_L - P_S) \quad [5.2]$$

where

$$X = \frac{x}{L_{eff}}, \quad R = \frac{r}{r_C} \quad [5.3]$$

$$P_L = \frac{p_L}{p_{L,in}}, \quad P_S = \frac{p_S}{p_{L,in}} \quad [5.4]$$

$$k_1 = \frac{k_{x,L}}{k_{x,S}}, \quad k_2 = \frac{k_{r,S}}{k_{x,S}}\frac{L_{eff}^{\ 2}}{r_C^2}, \quad k_3 = \frac{k_{x,s}}{k_{x,S}} \quad [5.5]$$

$$La = \frac{L_p A_v L_{eff}^{\ 2}}{k_{x,S}} \quad [5.6]$$

Boundary conditions are given in fig. 21.

The mesh and problem files, as applicable to the current problem, will now be discussed to show how equations [5.1] and [5.2] are solved.

5.1.1 The computational domain and finite element mesh

The physical membrane modules used in this study and thus the computational domain are similar to that shown in figs. 13 and 14 in section 3.3.2. The only difference is that the modules under investigation have no ECS manifolds. Permeate is withdrawn from an outlet, which is basically a round hole, at the one side of the module. However, in order to make the modules two-dimensional and axisymmetric, the permeate outlet was modelled as a slit, with the same flow area as the original hole, right around the module. This slit resembles the ECS manifold and is illustrated in fig. 17. The permeate outlet can be either at the upstream end, in the middle or at the downstream end of the module.

The axisymmetric computational domain, with all applicable boundary conditions, is shown in fig. 18. The boundary conditions are colour-coded for easier identification.

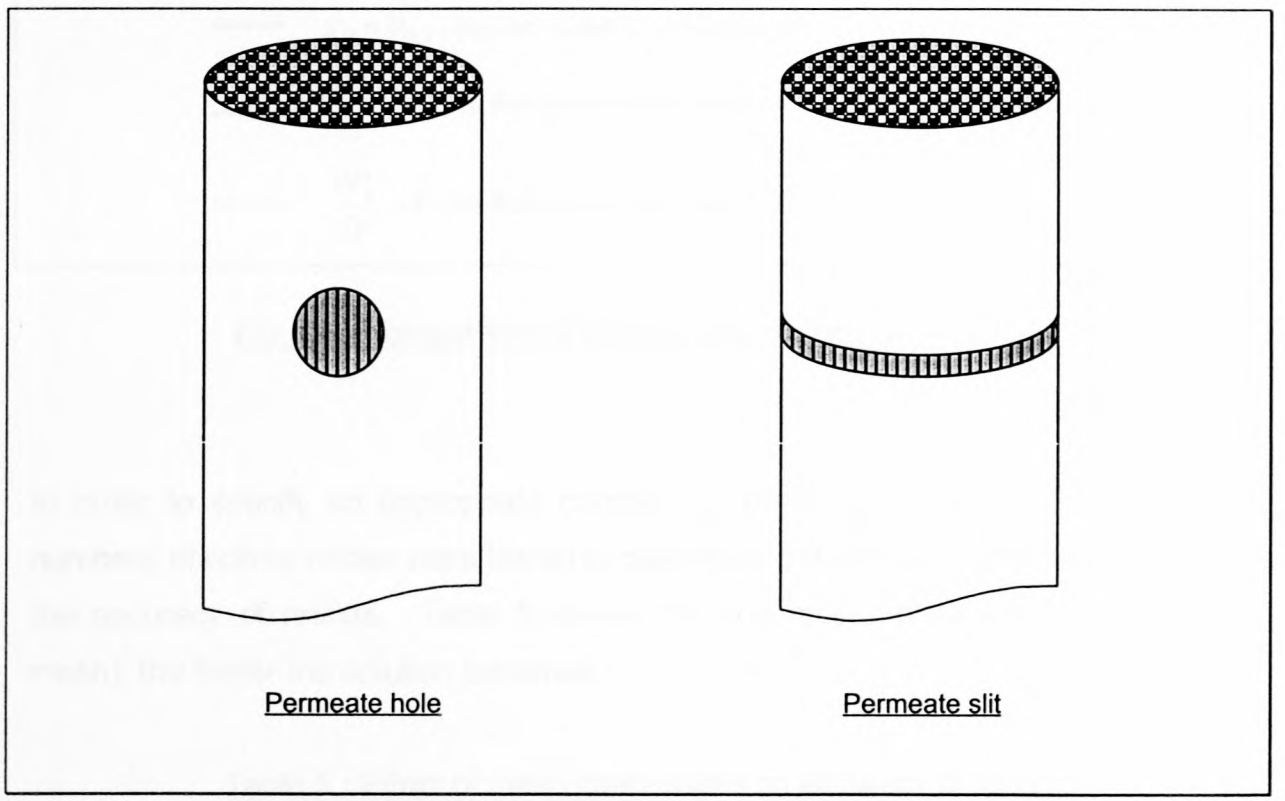

Fig. 17 : Permeate outlet modelled as a slit.

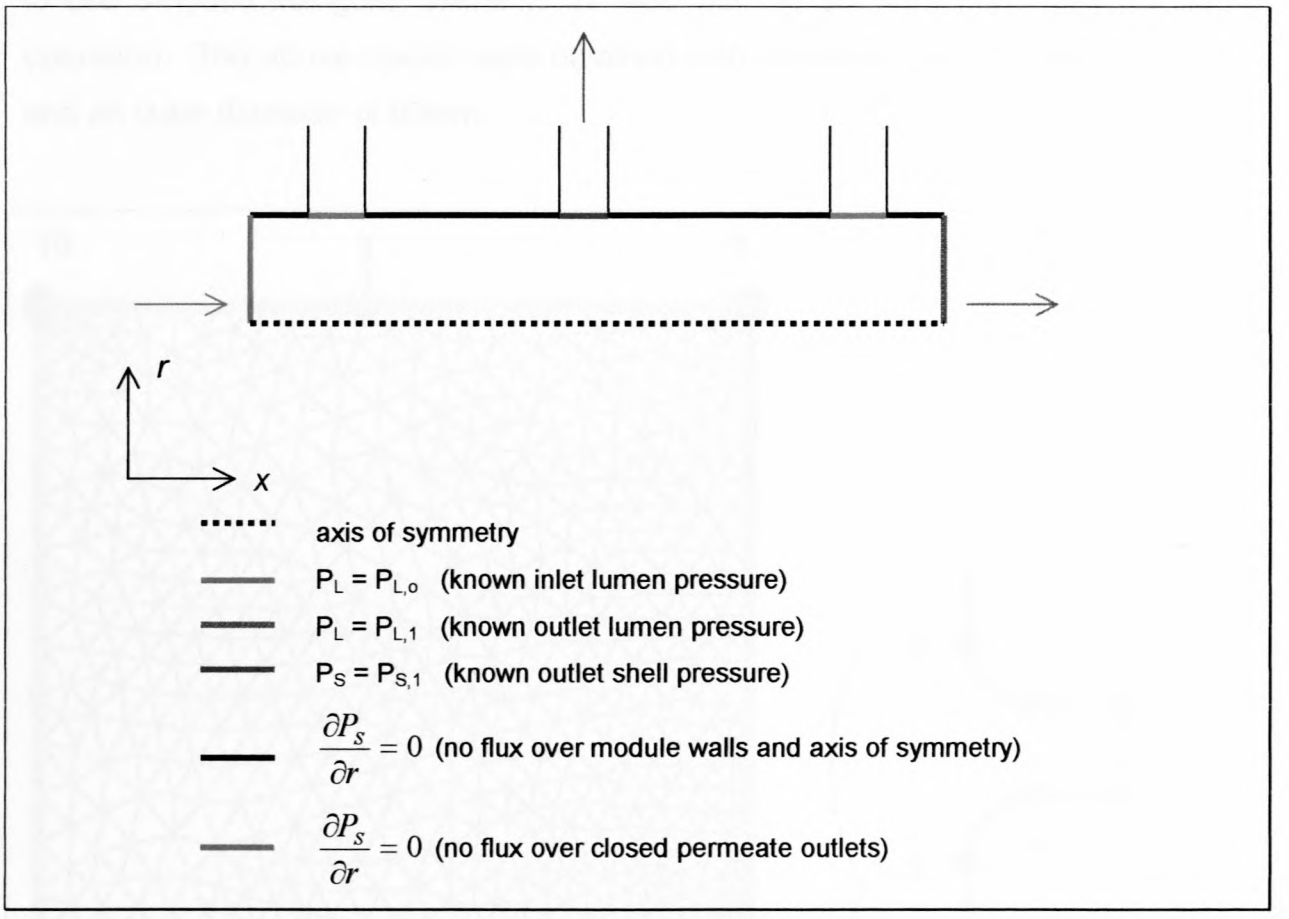

Fig. 18 : Computational domain and boundary conditions.

In order to specify an appropriate number of corner nodes for the mesh, various numbers of corner nodes were tested to determine the effect of mesh coarseness on the accuracy of results. Table 5 shows that the more nodes are used (i.e. finer mesh), the better the solution becomes.

Table 5 : Effect of mesh coarseness on accuracy of results

Nr. of nodes	QLin (L/h)	QLout (L/h)	QLin – QLout (L/h)	QSout (L/h)	% error
100	6047.8	5700.7	347.1	361.3	2.00
250	6047.8	5700.8	347.0	348.9	0.28
500	6047.7	5700.9	346.8	350.4	0.52
750	6047.8	5701.0	346.8	349.7	0.42
1000	6047.6	5701.0	346.6	345.4	0.17
1500	**6047.5**	**5701.0**	**346.5**	**346.2**	**0.04**
2000	6047.5	5701.1	346.6	345.3	0.16
2200	6047.5	5701.1	346.4	342.1	0.64

Ideally, the difference between the lumen inlet and outlet flow rates, $Q_{L,in}$ - $Q_{L,out}$,

consisting of 1500 nodes produced the most accurate results. Finer meshes need too much processing time, so a choice of 1500 corner nodes was an acceptable specification. In addition, 6-noded triangular elements were used. It was attempted to use 3-noded triangular elements as well, but the software performed an illegal operation. The above results were obtained with a module having a length of 1.2m and an outer diameter of 90mm.

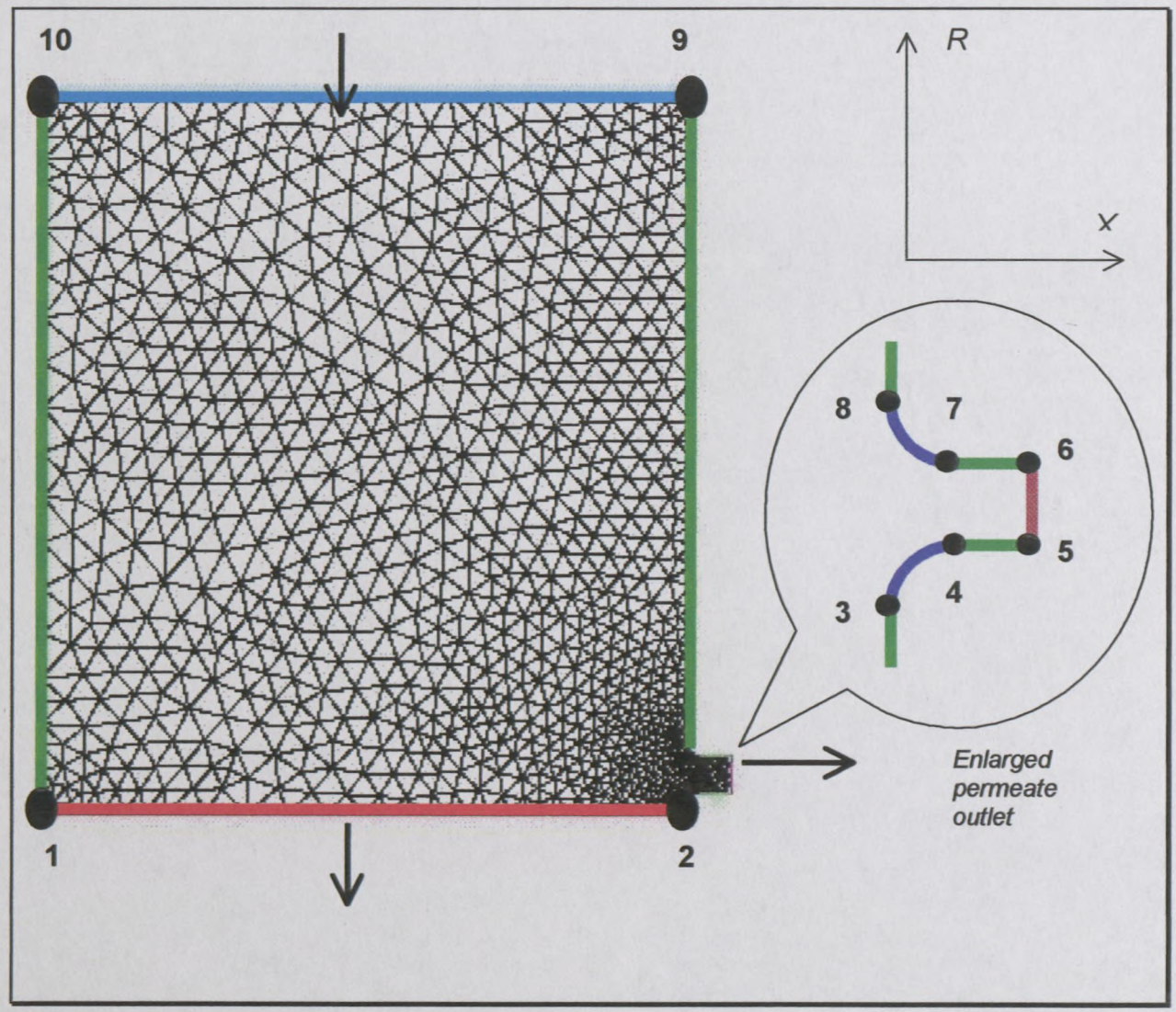

Fig. 19 : The finite element mesh.

The computational domain in fig. 19 is for a membrane module in a vertical position, with the permeate outlet located at the bottom. Flow is from the top to the bottom, with the lumen inlet at the top and the lumen outlet at the bottom. Boundary conditions are colour-coded. The mesh is concentrated near the permeate outlet,

where the most significant radial gradients occur, as a uniform mesh concentration results in an inaccurate solution. Table 6 summarizes this. The complete mesh file for fig. 19 is given in Appendix D.

Table 6 : Effect of mesh concentration

	Concentrated mesh	Uniform mesh
QLin (L/h)	6047.5	6050.8
QLout (L/h)	5701.0	5698.1
QLin - Qlout (L/h)	346.5	352.7
QSout (L/h)	346.2	193.8
% error	0.04	29.07

5.2 ESTIMATING THE LUMEN AXIAL PRESSURE DROP

Of the many parameters to be specified in *Fastflo*'s problem file, some must be determined experimentally beforehand. One of these, the outlet lumen pressure, $P_{L,out}$, depends on the axial pressure drop, ΔP, along the module length. The axial pressure drop depends on the length of the module and is calculated by making use of the rederived (Labecki *et al.*, 1995) 1-D model of Kelsey *et al.* (1990) and the Hagen-Poiseuille equation (Yoshikawa *et al.*, 1992).

Hagen-Poiseuille: $$\Delta P = \frac{8\mu L_{eff}}{\pi r_L^4} \cdot \frac{Q_{feed}}{N}, \quad \text{where } Q_{feed} = uA_{flow} \qquad [5.7]$$

1-D model: $$Q_{feed} = \alpha(\lambda B_1 + B_3) \qquad [5.8]$$

where

$$\alpha = -\frac{N\pi r_L^4}{8\mu L_{wet}} \qquad [5.9]$$

$$\lambda = 4\sqrt{\kappa(1+1/\gamma)} \qquad [5.10]$$

$$\kappa = \frac{L_p L_{wet}^2}{r_L^3} \qquad [5.11]$$

$$\gamma = \left(\frac{1}{r_L^4}\right)\left[4r_S^4 \ln(r_S/r_M) + 4r_S^2 r_M^2 - 3r_S^4 - r_M^4\right] \qquad [5.12]$$

$$B_1 = \frac{(P_{S,out} - P_{L,in})[\cosh(\lambda)-1] + (P_{L,out} - P_{L,in})\left[1+\frac{\cosh(\lambda)}{\gamma}\right]}{\frac{[\lambda - \sinh(\lambda)][\cosh(\lambda)-1]}{\gamma} + \left[\frac{\lambda}{\gamma} + \sinh(\lambda)\right]\left[1+\frac{\cosh(\lambda)}{\gamma}\right]} \qquad [5.13]$$

$$B_3 = \frac{\lambda}{\gamma} B_1 \qquad [5.14]$$

In this study, an inlet flow velocity, u = 1.2 m/s, is used. This value falls within the velocity range of 1 to 1.5 m/s commonly used in the industry. Higher values result in too large pressure drops, which are counterproductive. Instead of guessing a value for ΔP in order to obtain a value for $P_{L,out}$ in equation [5.13], ΔP is estimated by using the H-P equation. The 1-D model is then used to predict the lumen feed flow rate, from which the inlet flow velocity is calculated. If this is not equal to 1.2 m/s, ΔP and thus the outlet lumen pressure are adjusted iteratively until the inlet flow velocity is equal to 1.2 m/s. The value for ΔP which yields an inlet flow velocity of 1.2 m/s, is then used in *Fastflo*. In this study, the permeate flux for membrane modules of different lengths and diameters will be predicted, so the above procedure is repeated for all the various module lengths. More details of the calculation can be found in Appendix F. Table 7 lists the results of the axial pressure drop estimations.

Table 7 : Estimated axial pressure drops as a function of module length

L (m)	0.5	0.6	0.7	0.8	0.9	1.0	1.1	1.2
ΔP (Pa)	10729	13510	16275	19025	21758	24478	27185	29880

5.3 MEMBRANE PERMEABILITY DETERMINATION

The membrane permeability, L_p, must also be determined beforehand. The permeability of the membranes was determined using the PMM and is calculated by

$$L_p = \frac{\mu Q}{A \Delta p_m} \qquad [5.15]$$

where Q is the experimental transmembrane flow rate, or permeation flow rate, A is the total membrane surface area and Δp_m is the transmembrane pressure drop. In the cross-flow filtration mode, the transmembrane pressure drop is difficult to determine. The pressure drop, Δp, between the lumen inlet and shell outlet in the dead-end filtration mode, is more easily measured, since all the pressure drop occurs across the membrane. This approximation is used to determine the apparent permeability:

$$L_{p,app} = \frac{\mu Q}{A \Delta p} \qquad [5.16]$$

The procedure consists of two parts : numerical and experimental. Using a dead-end mode simulation in *Fastflo*, the lumen inlet pressure is set to a known, fixed value, while the shell outlet pressure is kept at 0 kPa. Thus Δp is specified. With μ and A also specified, the actual L_p is treated as a variable input parameter. The flow rate, Q, is then calculated with the PMM by numerically integrating the normal component

of the superficial velocity over either the inlet or outlet flow area. This value of Q is then used to calculate the apparent permeability, $L_{p,app}$. Repeating the procedure for a range of different L_p values, a correction plot of $L_{p,app}$ vs. L_p (fig. 25) is obtained. Next Q and Δp are measured experimentally in the *dead-end mode.* For this purpose an experimental set-up as shown in fig. 20 was constructed. Clear PVC pipe was used as the shell for the membrane module. The test module was 1.2m long and 50mm in outer diameter. A bundle of 339 fibres was used for an effective membrane area of 1.38 m^2 and a packing density of 62%, or a void fraction of 38%. The fibre bundle was inserted with the ends sticking out about 10 cm at both ends of the module. The module was spun in a centrifugal device in order to insert an epoxy solution to a depth of 6 cm at both ends, the epoxy being the medium with which the fibres are sealed inside the module. The module was then left alone for 48 hours to allow the epoxy to set. Lastly the protruding ends of the fibre bundle was cut off so that the fibre lumens were exposed, the region inbetween the fibres being filled with epoxy. The module was then connected into the system as shown in fig. 20. The permeate pipe was connected to the module by placing saddles over each of the permeate outlets.

In the experimental procedure, water was pumped from the reservoir, with some of the feed bled through valve V1 to obtain the correct inlet feed pressure, measured by gauge P1 or P2, depending on whether the module (HFMM) is fed from the top or bottom. With the feed from the top, valve V3 was opened, while valve V2 was opened for feed from the bottom. Dead-end filtration with the feed from both ends was achieved by opening valves V2 and V3. (V5 was opened with V3 and V4 was opened with V2 for cross-flow filtration.) Valve V6 was used to drain the system. The position of the permeate outlet was controlled by opening either V7, V8 or V9. The flow rate, Q, was measured by rotameter R1 or R2, which were equal in the dead-end filtration mode, while the pressure drop, Δp, was given by P1 or P2, since the outlet pressure was atmospheric, or zero gauge pressure. Having obtained experimental values for Q and Δp, $L_{p,app}$ was calculated from eqn. [5.16]. Finally the correction plot (fig. 22) was used to obtain the true permeability.

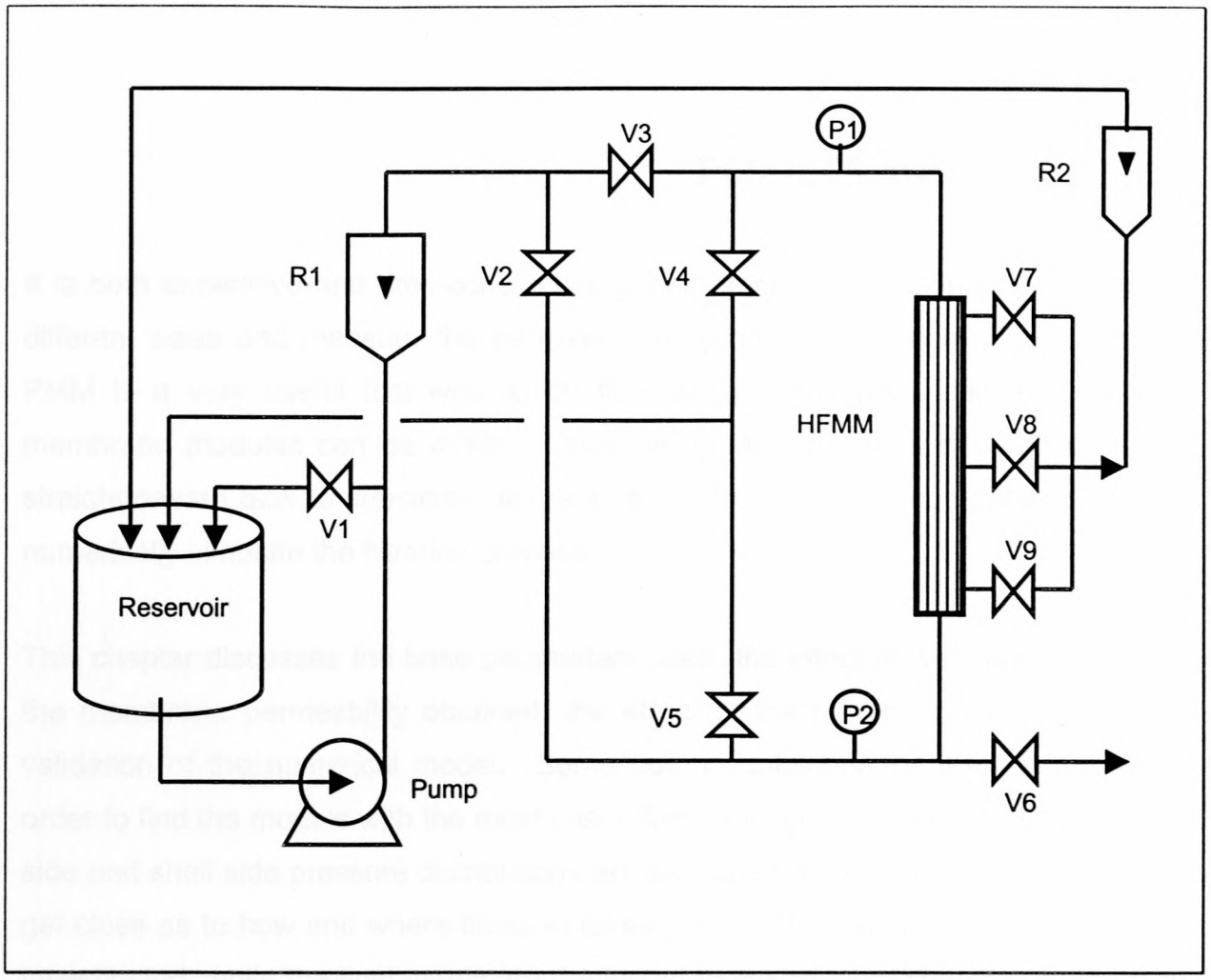

Fig. 20 : Schematic diagram of experimental set-up for hollow-fibre membrane module filtration plant.

~~~
~~~

Chapter 6

RESULTS AND DISCUSSION

It is both expensive and time-consuming to build membrane modules physically of different sizes and measure the permeate flux produced by each one. Thus the PMM is a very useful tool with which flux predictions for an infinite number of membrane modules can be made. Once the model has been developed, it is a straightforward task to substitute different values for all the various parameters and numerically simulate the filtration process.

This chapter discusses the base parameters used, the effect of wet fibre expansion, the membrane permeability obtained, the effect of the permeate slit size and the validation of the numerical model. Some cost calculations are also performed in order to find the module with the most cost effective length and diameter. The lumen side and shell side pressure distributions are examined during cross-flow filtration to get clues as to how and where filtration takes place. The backwash process is also investigated, while the final pages are dedicated to the effect of changing membrane permeability on lumen side and shell side pressure distributions.

6.1 BASE PARAMETERS USED

In this study the permeate flux was predicted for modules of various lengths and diameters. The parameters given in Table 8 were kept constant. Module outer diameter was based on standard u-PVC dimensions, while module length ranged from 0.5 m to 1.2 m as the hollow fibres are manufactured in lengths up to 1.4m. Fibre inner and outer diameters were fixed at 1.2 mm and 1.8 mm respectively. The membrane permeability depends on the type of membrane and was determined experimentally as 2.3×10^{-13} m. The water temperature was kept constant at 20°C, at which the viscosity and density were 0.001002 Pa.s and 998 kg/m^3 respectively. The packing density of 62% was based on the effective membrane area of 5 m^2 per 1.2 m length for a module of 90 mm outer diameter (Jacobs, 1998). The inlet

pressure was chosen as 100 000 Pa for ease of use, while the inlet flow velocity was set at 1.2 m/s, a commonly used specification in the industry.

Table 8 : Base parameters used

Module outer diameter *(standard u-PVC dimensions)*	D_o	20mm; 25mm; 32m; 40mm; 50mm; 63mm; 75mm; 90mm; 110mm; 125mm; 140mm; 160mm; 200mm; 250mm; 315mm; 355mm; 400mm.
Module length	L	0.5m; 0.6m; 0.7m; 0.8m; 0.9m; 1.0m; 1.1m; 1.2m
Membrane permeability	L_p	2.3×10^{-13} m
Inner fibre diameter	d_i	1.2mm
Outer fibre diameter	d_o	1.8mm
Fluid viscosity	μ	0.001002 Pa.s
Fluid density	ρ	998 kg/m^3
Inlet pressure	$P_{L,in}$	100 000 Pa
Inlet flow velocity	u	1.2 m/s
Fibre packing density	PD	62%
Number of fibres	N	*depends on module diameter* (see Appendix H)
Axial permeability	$k_{x,L}$	*depends on module diameter* (see eqn. [3.44])
Shell axial permeability	$k_{x,S}$	*depends on module diameter* (see eqn. [3.45])
Shell radial permeability	$k_{r,S}$	*depends on module diameter* (see eqn. [3.46])

6.2 EFFECT OF MOISTURE ON DRY FIBRE LENGTH

As already mentioned, the PMM takes into account the expansion of the hydrophilic fibres in the axial and radial directions when wetted. In order to determine the extent of wet expansion, water was pumped for 24 hours through fibres of various lengths to wet them. Then they were dried for another 24 hours and their dry lengths measured. The results are displayed in table 9.

Although an average axial expansion of 0.62% was measured, these results can be deemed insignificant, as the wet fibre expansion was less than 1% in all cases. However, this effect was included in *Fastflo*'s problem file. Furthermore, when

ignoring the outlier expansions of 0.43%, 0.5% and 0.6%, the average axial expansion was found to be approximately 0.7%, which was the value used in *Fastflo*.

Table 9 : Effect of wet fibre expansion

Dry length [mm]	Wet length [mm]	% expansion
1192	1200	0.67
1093	1100	0.64
993	1000	0.70
894	900	0.67
794	800	0.76
697	700	0.43
597	600	0.50
497	500	0.60

6.3 MEMBRANE PERMEABILITY

The procedure for membrane permeability determination was described in section 5.3. Values for the simulated permeability, L_p, ranged from 1×10^{-16} m to 1×10^{-8} m. Various module configurations were used, all with an inlet-to-outlet pressure drop of 100 kPa. These configurations are shown in fig. 21 on the next page.

The valves in fig. 24 that should be opened for each configuration, are:

- Config. A – V3, V9
- Config. B – V3, V7
- Config. C – V3, V7, V9
- Config. D – V2, V3, V7, V8
- Config. E – V3, V8

A module with the following physical dimensions was used for the various configurations:

- Length – 1.2 m
- Outer Diameter – 50 mm
- Number of fibres – 339
- Packing density – 62%

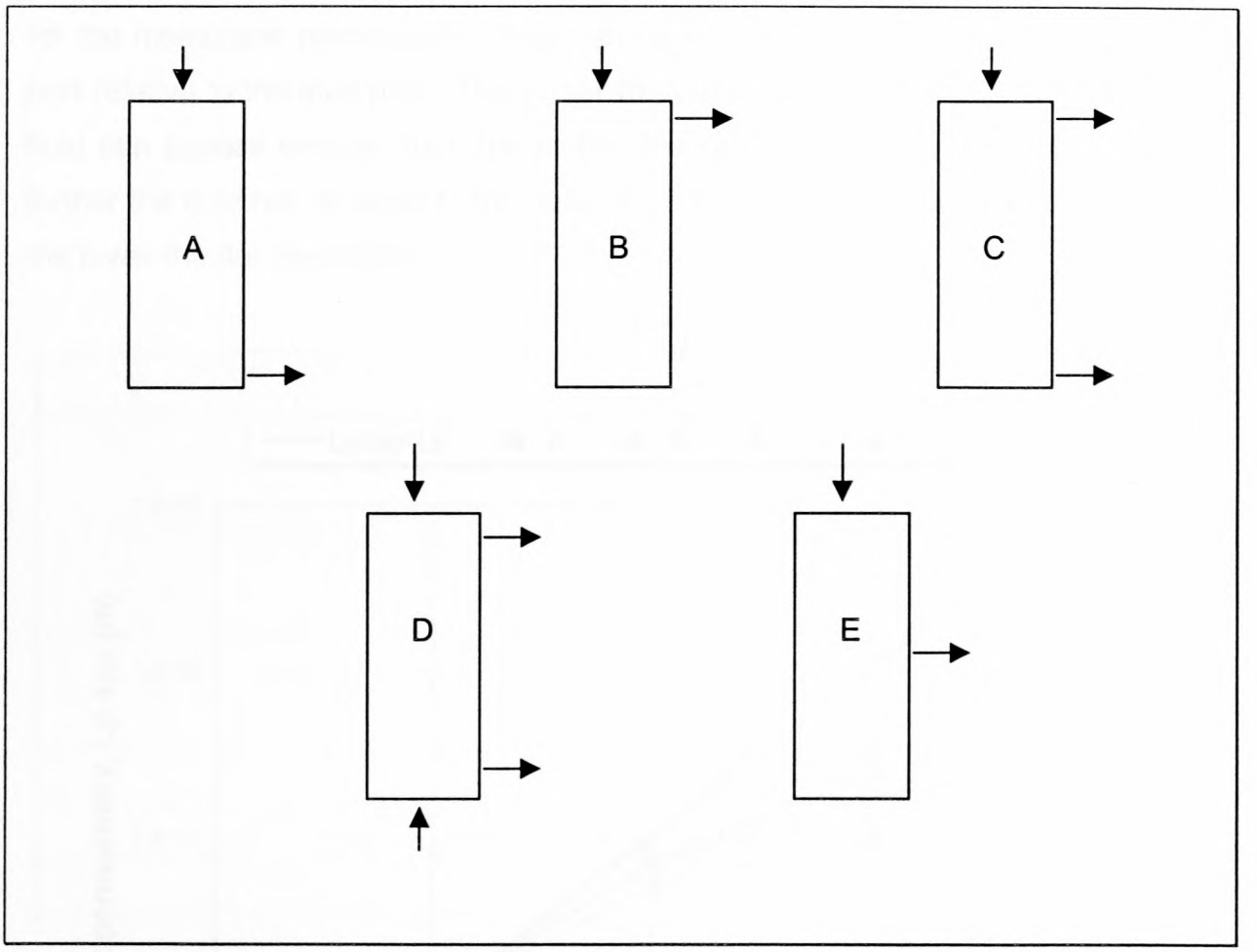

Fig. 21 : Dead-end flow configurations used in membrane permeability determination: A) Downstream outlet port open; B) Upstream outlet port open; C) 2 outlet ports open; D) 2 inlet and 2 outlet ports open; E) Middle outlet port open.

Representing the relationship between $L_{p,app}$ and L_p graphically, a correction plot (fig. 22) for the various module configurations is obtained which can be used to obtain a better estimate of the true membrane permeability determined from flow rate and pressure drop measurements. Actual values are shown in Appendix G. Fig. 22 compares very well with the results obtained by Labecki *et al.* (1995). Note that configuration E is an additional configuration not used by Labecki *et al.*

It is evident from fig. 22 that the curves start to deviate from the $L_{p,app} = L_p$ line from a permeability of 1×10^{-12} m. Thus for highly permeable membranes, the L_p estimates will be less accurate. This is because most of the resistance is imposed by the lumen and the shell side space, rather than by the membrane, especially at L_p values above 1×10^{-11} m. Flow configuration D appears to yield the most accurate estimate for the membrane permeability. This can be explained by the position of the outlet port relative to the inlet port. The closer the outlet port is to the inlet port, the more fluid can bypass directly from the inlet to the outlet, producing a higher flux. The further the fluid has to travel to the outlet port, the more resistance it encounters and the lower the flux becomes.

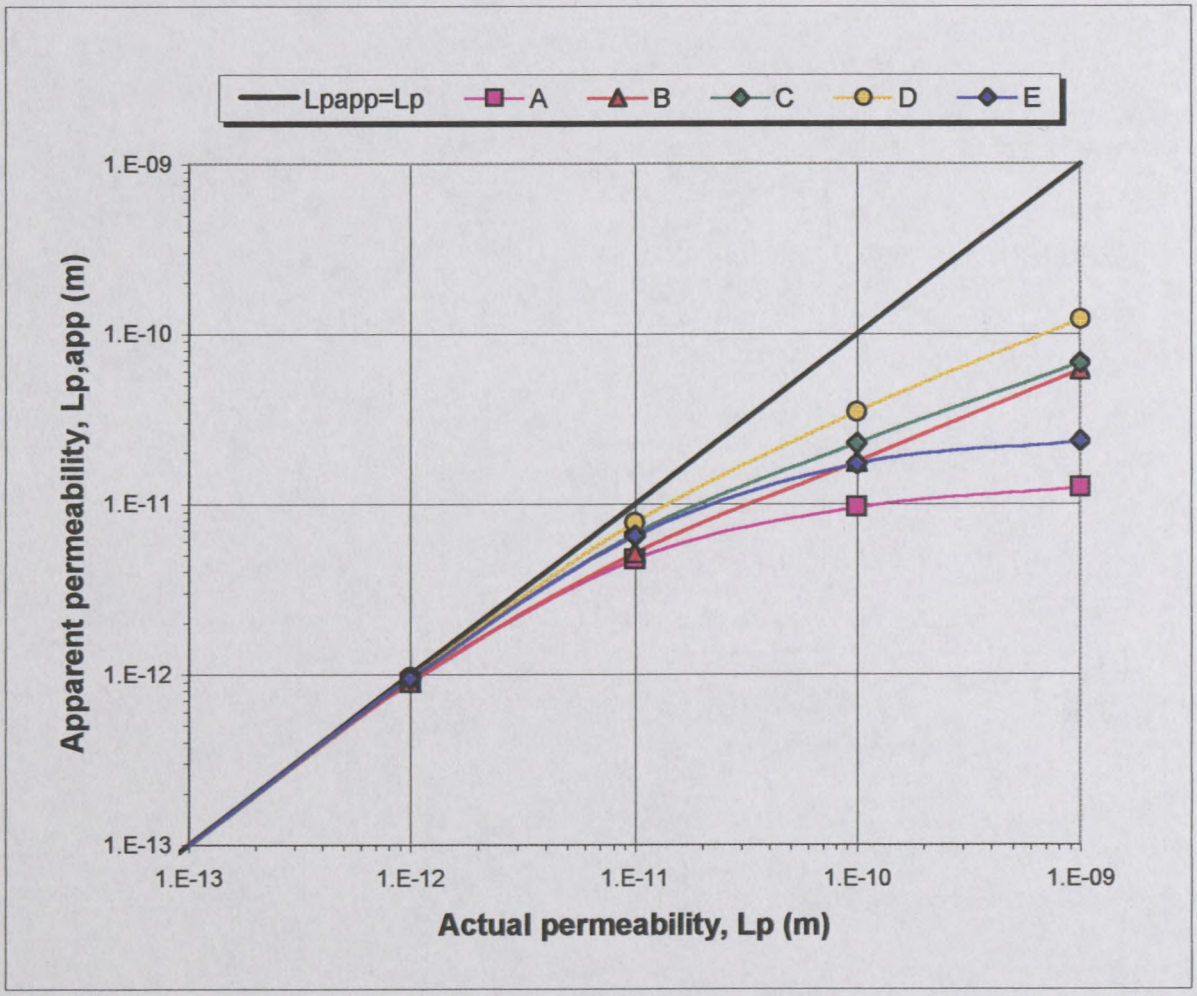

Fig. 22 : Apparent membrane permeability as a function of actual membrane permeability for several dead-end mode configurations.

Q and Δp_m were measured experimentally in the *dead-end* filtration mode for the module with dimensions given on p. 67 and found to be:

- Q = 114 L/h (or 82.6 LMH using effective membrane area of 1.38 m^2)
- Δp_m = 100 000 Pa

Substituting these values into eqn. [5.16], an apparent permeability, $L_{p,app} = 2.3 \times 10^{-13}$ m, is obtained. This implies a true permeability, $L_p = 2.3 \times 10^{-13}$ m, by using the correction plot. From figs. 15 and 16 on p. 46, it can be seen that this value for L_p is in the region where the KCM and PMM yields similar results. Any of the models may thus be used to make flow predictions, but the PMM would be preferred, because the value for L_p obtained above is more or less at the point where the KCM and PMM prediction curves begin to diverge.

6.4 VALIDATION OF THE NUMERICAL MODEL

In order to verify the accuracy of the PMM, a mass balance was done between the lumen inlet and shell outlet flows as the first step. In the *dead-end* filtration mode, the inlet flow rate should be equal to the outlet flow rate. The lumen inlet flow rate was predicted by numerically integrating the normal superficial velocity component (axial) over the circular inlet flow area, while the shell outlet flow rate was predicted by integrating the normal superficial velocity component (radial) over the flow area of the permeate slit. The following results were obtained with the 1.2 m length, 50 mm outer diameter module, using both the upstream and downstream permeate outlets :

Table 10 : Mass balance between inlet and outlet flow rates

	Upstream	**Downstream**
Lumen inlet flow rate (L/h)	117.8	112.1
Shell outlet flow rate (L/h)	117.6	111.8
Difference (L/h)	0.2	0.3
Error	0.17%	0.27%

These results show that the mass balance was satisfied to an acceptable degree of accuracy.

The next step in validating the suitability of the model was to compare the model predictions with physical measurements made under various operating conditions of inlet pressure and flow rate. Here the *cross-flow* filtration mode was applied using a module with the same dimensions as above. The results obtained are given in table 11.

Table 11 : Comparison between numerical predictions and experimental measurements for different inlet conditions of pressure and flow rate

Inlet pressure (Pa)	Inlet flow rate (m/s)	Model prediction (L/h)	Experimental flow rate (L/h)	Difference (L/h)	% error
75 000	1.2	61.2	63	1.8	2.9
100 000	1.2	86.9	89	2.1	2.4
125 000	1.2	109.8	113	3.2	2.9
150 000	1.2	136.9	140	3.1	2.2
100 000	1.0	89.5	92	2.5	2.7
100 000	1.5	83.0	85	2.0	2.4

First the inlet flow rate was kept constant at 1.2 m/s and the inlet pressure varied from 75 000 Pa to 150 000 Pa. Then the inlet pressure was kept constant at 100 000 Pa and the inlet flow rate varied between 1.0 m/s and 1.5 m/s. The model predictions compared favourably with the experimental measurements of permeate flow rate, with an average error of 2.6%. From the results in tables 10 and 11, it can be concluded that the PMM can be used with confidence to predict permeate fluxes produced by HFMMs of different designs.

6.5 EFFECT OF PERMEATE SLIT SIZE

In section 5.1.1 it was mentioned that the permeate outlet was modelled as a slit right around the module, in order to make the computational domain axisymmetric. The flow areas of each slit and equivalent circular permeate outlet should be equal :

Area (slit) = Area (circular outlet)

$$\pi D_o H = \frac{\pi}{4} D_h^2$$

$$H = \frac{D_h^2}{4D_o}$$

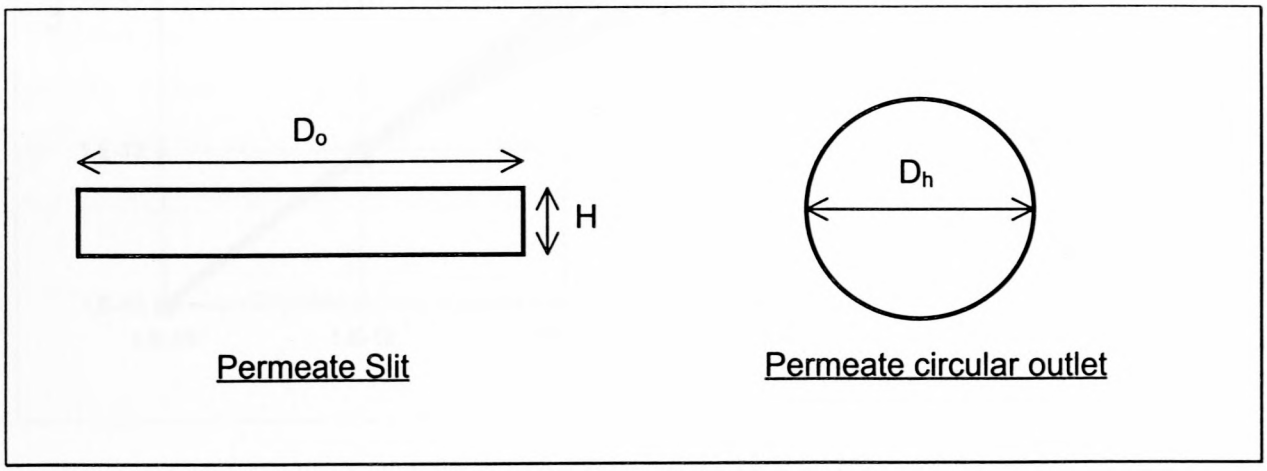

Fig. 23 : Dimensions of permeate slit and equivalent circular outlet.

The exact size of the slit is not that critical, as is illustrated by fig. 24. The membrane permeability determination as discussed in section 6.2 was done for slit sizes of 1 mm (blue) and 5 mm (red), which imply circular permeate outlets having diameters of 18.97 mm and 42.43 mm respectively. The flow configurations in fig. 21 were used for a module outer diameter of 90 mm. The results were almost identical, with only slight differences for $L_p > 1 \times 10^{-10}$m.

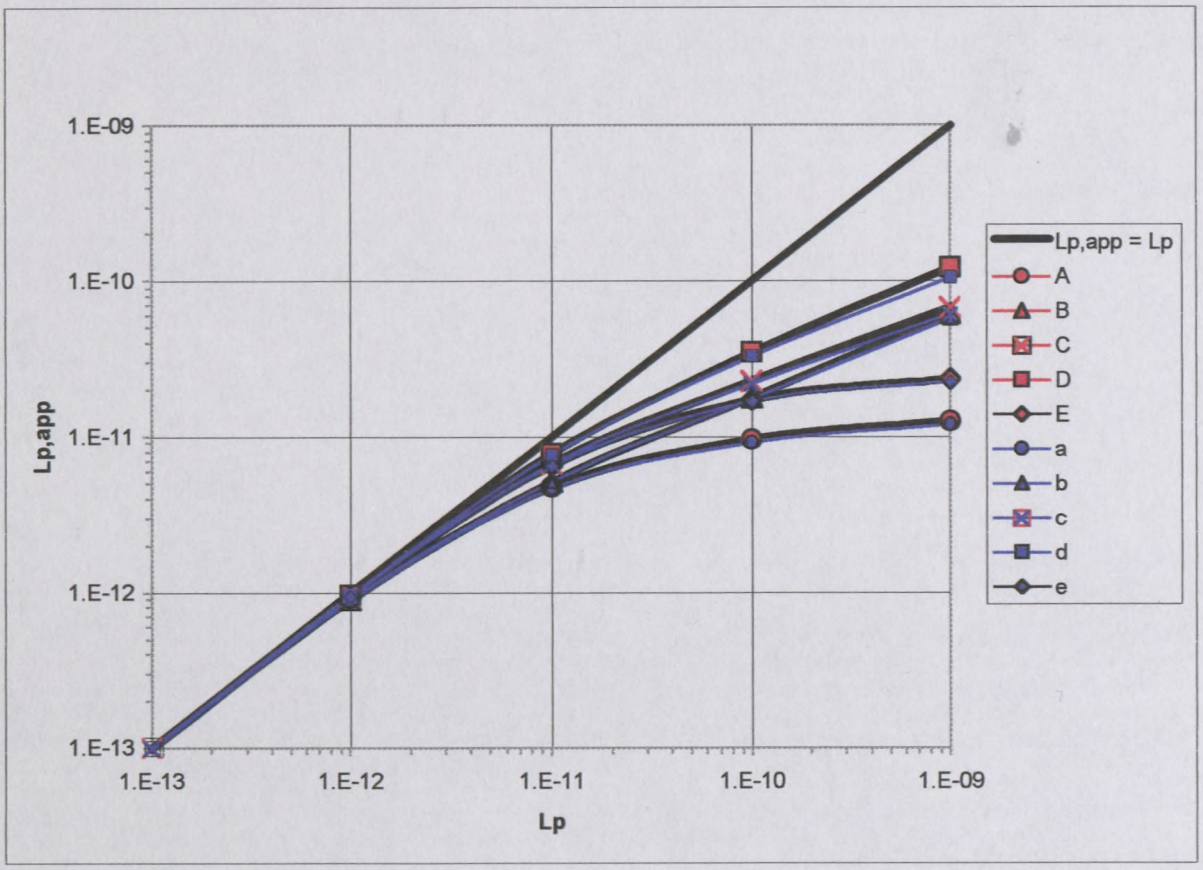

Fig. 24 : Permeability correction plot using different permeate slit sizes.

6.6 COMPARISON OF FLUX FOR VARIOUS MODULE GEOMETRIES

The numerical simulation software was used to predict the permeate flux for modules with lengths ranging from 0.5 m to 1.2 m and outer diameters ranging from 20 mm to 400 mm. Inlet conditions were 100 000 Pa feed pressure and 1.2 m/s flow rate. The effect of the positioning of the permeate outlet (fig. 25) was also investigated. Three outlet positions were tested: 1) in the upstream position, i.e. near the lumen inlet, 2) in the downstream position, i.e. near the lumen outlet and 3) halfway down the length of the module.

The upstream positioning yielded the highest permeate flux (in units of litres per m^2 per hour, abbreviated as LMH), as can be seen in fig. 29 for the case of a module with 1.2m length and 90mm outer diameter.

The reason for this is that the fluid encounters the least resistance in this arrangement, as some of the fluid bypasses directly into the permeate outlet, which is located almost next to the lumen inlet. In the downstream outlet positioning, fluid on the shell side has to travel a longer distance down the length of the module to the permeate outlet, thus yielding the lowest flux. The middle permeate outlet seems to be producing flux values that are the average of the fluxes predicted by the upstream and downstream permeate outlets. It is also evident from fig. 26 that as the module length increases, the three lines move further away from each other, indicating that the positioning of the permeate outlet becomes more critical as would be expected. These results are for pure water fluxes however, without the consideration of the effects of fouling and backwash, which may have a significant influence on the permeate outlet positioning. Permeate outlet positioning would be critical when considering procedures such as backwash to clean clogged fibres.

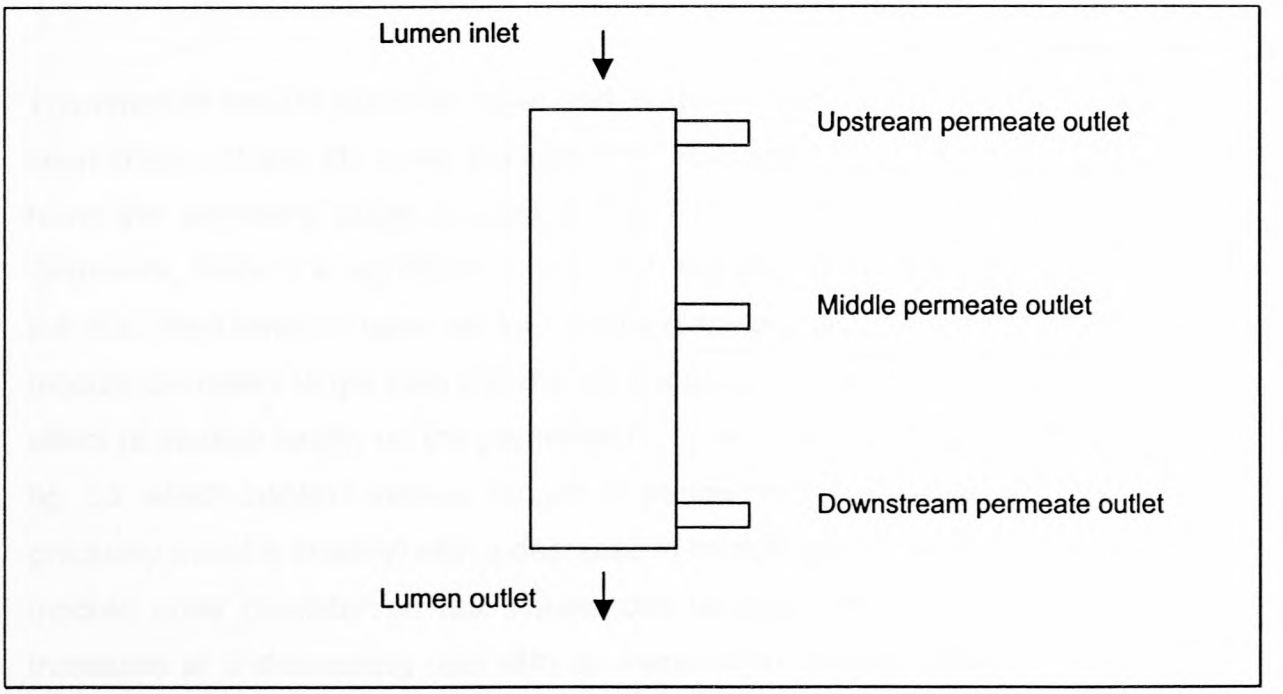

Fig. 25 : Various permeate outlet positions.

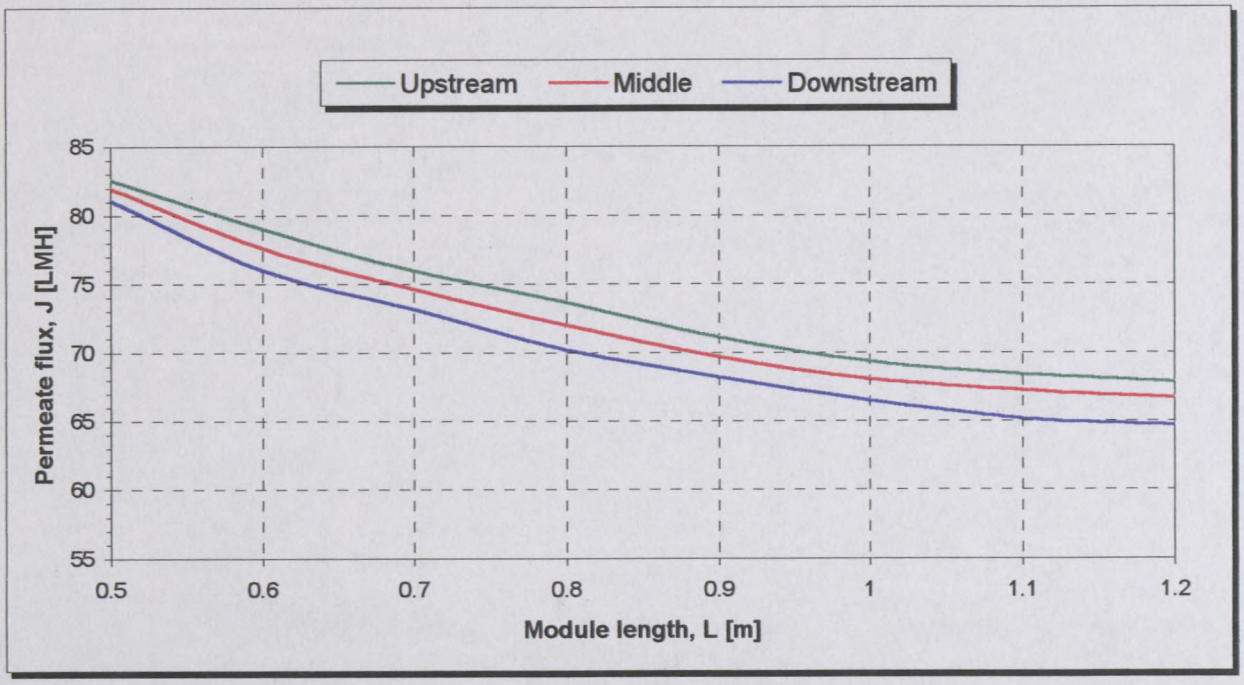

Fig. 26 : Effect of permeate outlet position on permeate flux.

The effect of module outer diameter and length on permeate flux predictions can be seen in figs. 27 and 28, using the inlet conditions given on pp. 64 – 65. All modules have the permeate outlet located in the middle position. For small module diameters, there is a significant increase in flux as the module diameter increases, but this effect tends to taper off for module diameters above 50 mm. It is clear that module diameters larger than 200 mm do not produce a notable increase in flux. The effect of module length on the permeate flux prediction can be seen more clearly in fig. 28, which displays various ranges of permeate flux predictions. The flux rises gradually (roughly linearly) with a decrease in module length, while the same effect of module outer diameter on flux values can be seen as in fig. 27. That is, flux increases at a decreasing rate with an increase in module outer diameter. When looking at the number of divisions along the y-axis in the various flux ranges, it is clear that there is a greater range of module diameters in the light green band (65 – 70 LMH) than in the yellow (60 – 65 LMH) or maroon (55 – 60 LMH) bands.

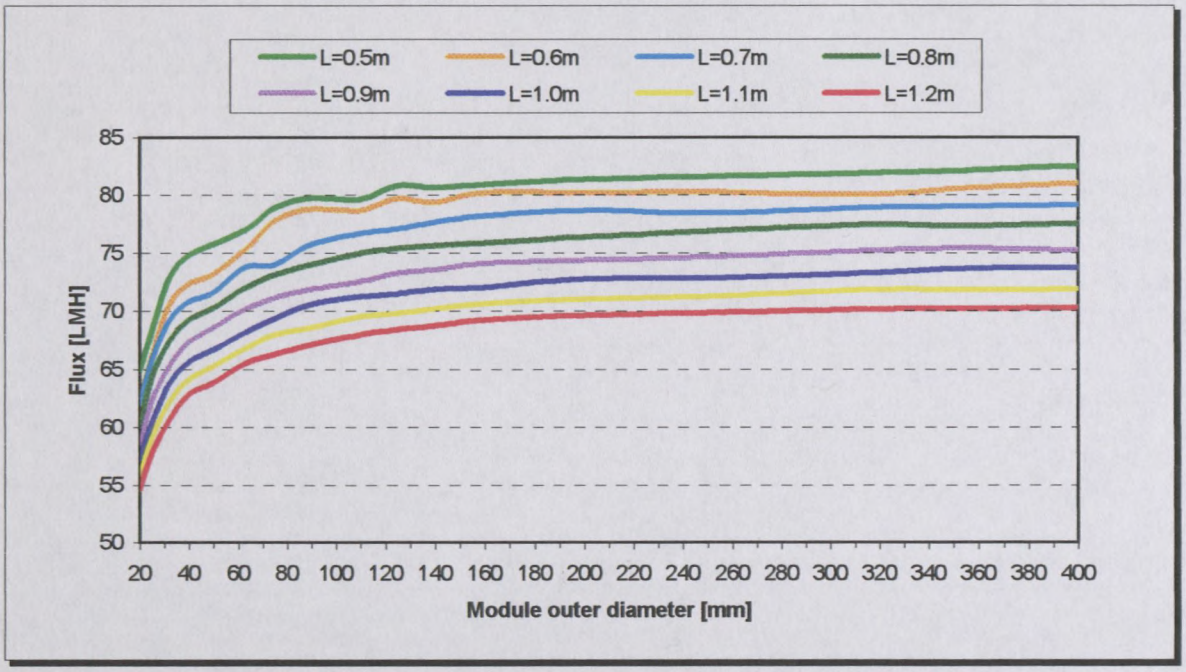

Fig. 27 : Effect of module outer diameter on flux prediction.

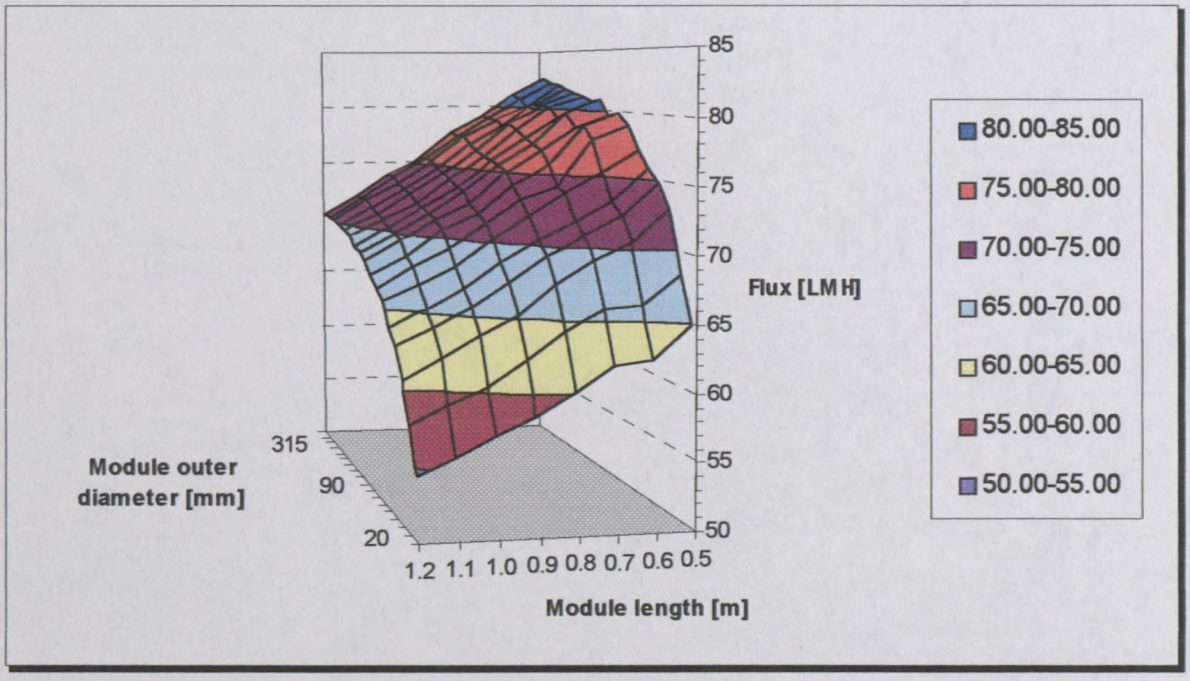

Fig. 28 : Effect of module length on flux prediction.

6.7 COST CALCULATIONS

Although the flux for various module geometries was predicted, we need to know which module size would be the most economical. We can do this by expressing the cost of each module in terms of a cost per unit volume permeate produced. The cost of each module comprised two components. The *capital cost* includes the cost of the module outer shell and hollow fibres, while the *operating cost* is the cost of pumping energy. The cost of pumps, piping and pipefittings are excluded for simplification.

6.7.1 Time value of money and discount factors

When performing cost calculations, we often encounter the problem of having to combine capital and operating costs. Capital costs are fixed and are measured in Rands, whereas operating costs are measured in Rands per unit time, typically Rands per year. These two costs must be placed on the same basis and we do this by making use of the time value of money (TVM). The easiest method is to annualise the capital costs and report all costs on an annual basis. The TVM is determined by expressing a single capital expenditure/investment as a series of equal payments (PMT), or annuities, spread over a certain number of years. These annual payments have the same units as operating costs. Douglas (1988) uses a discount factor, the capital charge factor (CCF), to account for the TVM. The present value (PV) of the capital investment is multiplied by the CCF to obtain an annuity. The CCF is given by:

$$CCF = \frac{[0.25(1+i)^4 + 0.295i - 0.298](1+i)^N - 0.225i + 0.048}{0.676[(1+i)^N - 1]} \qquad [6.1]$$

where i = interest rate per year and N = years of operation of the membrane plant.

Assuming the interest rate to be 15% per year and that the membrane plant will be in operation for 5 years, this yields a CCF = 0.57. However, CCF is intended for performing cost calculations of large chemical plants as it includes revenue, working capital, start-up costs and total production costs.

A membrane filtration plant is much smaller and simpler in comparison and the capital recovery factor, CRF (Turton *et al.* 1998), would be a more suitable discount factor. The PV of an annuity is given by (Brigham & Houston, 1998) :

$$PV = PMT\left[\frac{1}{i} - \frac{1}{i(1+i)^N}\right] \quad [6.2]$$

or

$$PV = PMT\left[\frac{(1+i)^N - 1}{i(1+i)^N}\right] \quad [6.3]$$

Capital cost is thus annualised by multiplying the PV by the CRF:

$$\text{PMT (R/yr)} = \text{PV (R)} \times \text{CRF (1/yr)} \quad [6.4]$$

where

$$CRF = \left[\frac{i(1+i)^N}{(1+i)^N - 1}\right] \quad [6.5]$$

Using an interest rate of 15% and a plant life of 5 years, this gives a CRF = 0.3. This value will be used to annualize capital costs in this study.

6.7.2 Cost comparisons

In order to find the most cost effective module in terms of cost per unit volume permeate produced, a spreadsheet was used as shown in Appendix I. The optimum module geometry, and thus cost, will depend on the product flow rate required. For the purpose of this study, it was assumed that the required product flow rate is 1 000 L/h. Capital cost consists of the cost of fibres and module housing, while operating cost is determined by the pumping energy. Details of all costs involved are set out in Appendix I. The following assumptions were also made:

- Inlet flow rate = 1.2 m/s
- Inlet lumen pressure = 100 kPa
- Operating time = 8000 hours per year
- Pump efficiency = 70%
- Cost of electricity = 30.27c per kWh

For each combination of module length and outer diameter, the cost per kL permeate produced was calculated by first determining the membrane area required to produce the desired product flow rate:

$$A_{req} = \frac{\text{Required product flow rate}}{Flux} = \frac{Q_{req}}{J} \qquad [6.6]$$

From this, the number of modules (rounded up to the nearest integer) that must be used, can be determined:

$$N = \frac{\text{Required membrane area}}{\text{Membrane area per module}} = \frac{A_{req}}{A_m} \qquad [6.7]$$

The actual membrane area used will always be more than that required, although the ratio between the two will in some cases be close to unity. The actual membrane area is given by:

$$A_{tot} = N \times A_m \qquad [6.8]$$

Similarly, the actual *permeate* flow rate that can be produced, will be more than that required:

$$Q_{act} = J \times A_{tot} \qquad [6.9]$$

The total *feed* flow rate to the system depends on the number of modules to be used:

$$Q_{feed} = u \times A_{flow} \times N \qquad [6.10]$$

The energy consumption can now be calculated:

$$E = C\frac{\Delta P \times Q_{feed}}{\eta} \qquad [6.11]$$

The operating cost per year is calculated by considering the cost of electricity and the operating time per year :

$$C_{yr} = E \times C_{kWh} \times \theta \qquad [6.12]$$

This can be expressed as a cost per kL permeate produced :

$$C_{pump} = \frac{C_{yr}}{\theta \times Q_{req}} \qquad [6.13]$$

Lastly the capital cost must be converted to the same basis as operating cost by making use of the capital recovery factor :

$$C_{cap} = \frac{C_{\mathrm{mod}} \times N}{\theta \times Q_{act}} \qquad [6.14]$$

Thus the total cost is the sum of operating cost and capital cost, expressed in cents per kL permeate. The results are graphically portrayed in fig. 32.

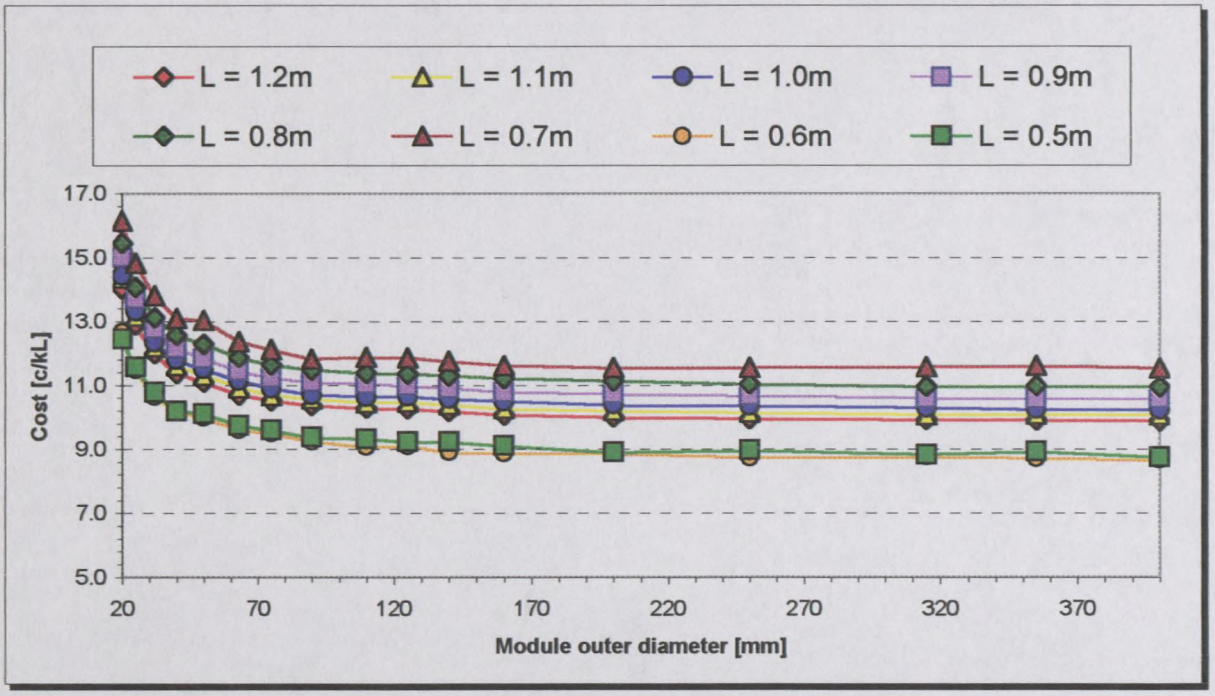

Fig. 29 : Actual cost chart for various module configurations for a required product flow rate of 1000 L/h

From fig. 29 one can see that modules with small diameters are very uneconomical, irrespective of their length. As the module diameter increases, cost decreases, but at a slowing rate. It appears that there is no benefit from using module diameters in excess of 160mm, as all the cost curves remain relatively flat above this diameter. On the flipside of the coin, modules with a diameter less than 90mm are too expensive. Another characteristic that is not easily observable in fig. 29, is the cost of modules with lengths of 0.5m and 0.6m, relative to other module lengths. This is shown more clearly in fig. 30, which shows the inverse relationship between cost and module length. The reason for the sudden drop in cost for module lengths of 0.5m and 0.6m, is explained by the manufacturing process of the hollow fibres. After the fibres are spun, they are cut into standard lengths of 1.4m for drying. It is obvious that for the 0.5m and 0.6m lengths, two fibre units can be cut from a standard 1.4m fibre length, allowing a few extra centimetres at both ends for potting into the modules. For these two lengths, the wastage is minimal. Fig. 31 shows how this is done. For any module length of 0.7m and longer, only one fibre unit can be cut from the standard 1.4m length. Much fibre is wasted for the 0.7m length, but the wastage decreases with an increase in module length. This is summarized in table 12.

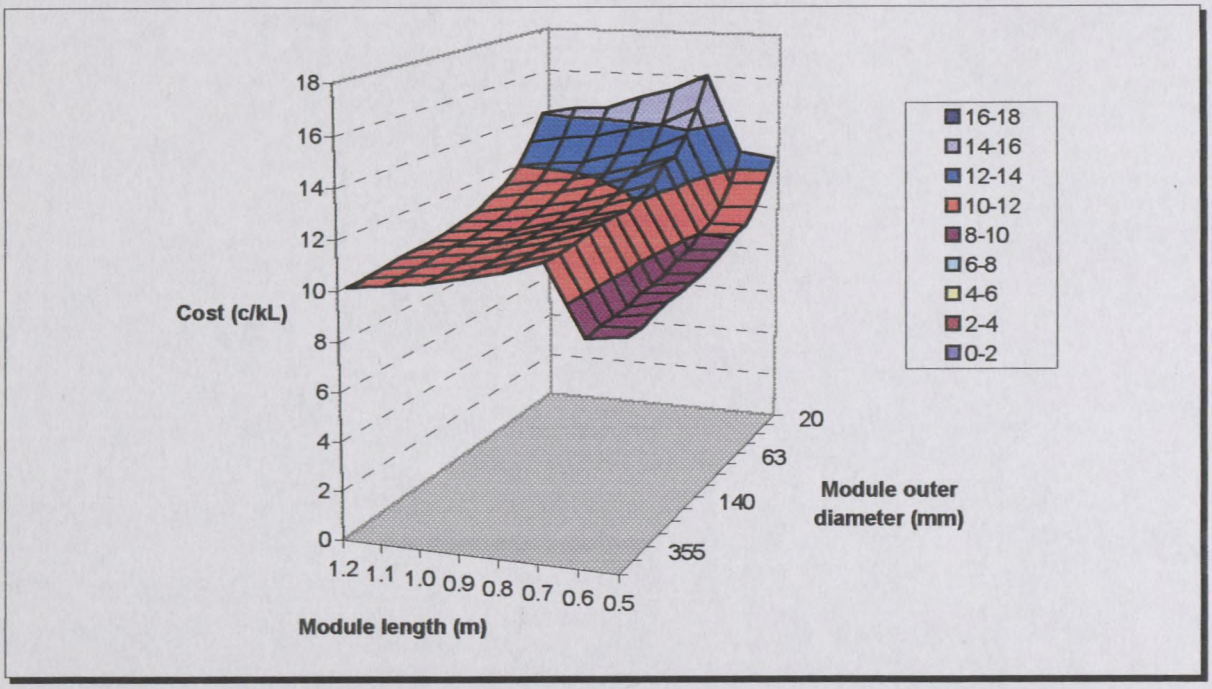

Fig. 30 : Surface chart for various module configurations for a required product flow rate of 1000 L/h.

Table 12 : Fibre wastage as a function of module length

Module length (m)	Wastage (m)	% wastage
2 × 0.5	0.4	28.6%
2 × 0.6	0.2	14.3%
1 × 0.7	0.7	50.0%
1 × 0.8	0.6	42.9%
1 × 0.9	0.5	35.7%
1 × 1.0	0.4	28.6%
1 × 1.1	0.3	21.4%
1 × 1.2	0.2	14.3%

Although the wastage of the two 0.6m lengths and the one 1.2m length is exactly the same, the overall cost also depends on other factors, such as the cost of the module itself.

From this discussion one can thus conclude that it would be best to use a module or series of modules having an outer diameter of between 90mm and 160mm and a length of 0.6m.

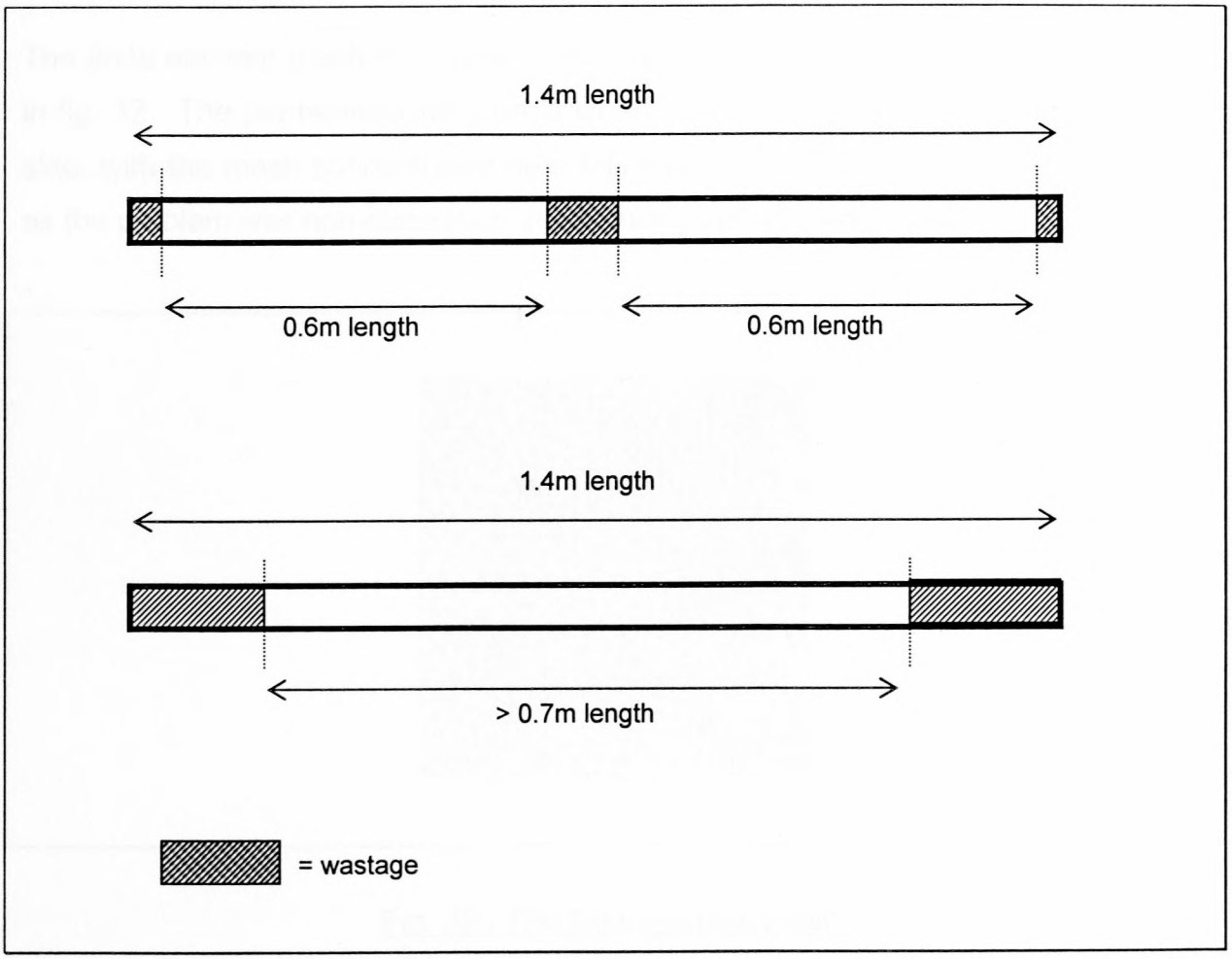

Fig. 31 : Fibre lengths and wastage.

6.8 PRESSURE DISTRIBUTIONS

Although *Fastflo* failed to solve an important part of the problem, we can still obtain valuable clues about the flow behaviour inside a hollow-fibre membrane module by looking at the shade plots of the pressure distributions.

The finite element mesh for a typical module installed in a vertical position is shown in fig. 32. The permeate outlet port is clearly visible in the middle on the right-hand side, with the mesh concentrated near this outlet. The module geometry is square, as the problem was non-dimensionalised during the solution process.

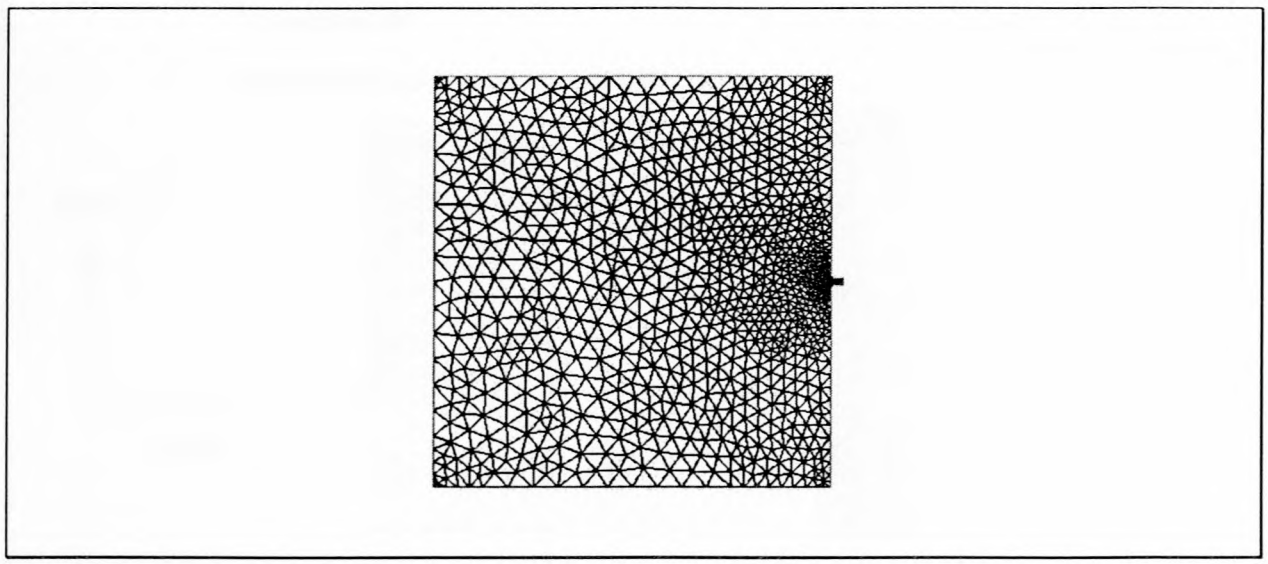

Fig. 32 : The finite element mesh.

6.8.1 Pressure distributions during cross-flow filtration

When solving for the lumen and shell side pressure distributions, a shade plot of these distributions can be drawn, giving the user a visual impression of what the pressure gradients on the lumen and shell sides look like. This is useful to give the user a snapshot of the flow patterns inside the module, as well as of the existence of dead spaces, if any. "Cold" colours (blue) denote low pressures, while "warm" colours (red) denote high pressures. For all shade plots, a key is given at the right-hand side. The numerical values are non-dimensional and should be multiplied by $P_{L,in}$ = 150 kPa. The lumen side pressure distribution for cross-flow filtration is shown

in fig. 33. As mentioned before, the module is installed in a vertical position, with the feed stream entering at the top and exiting at the bottom. Shell side permeate is withdrawn from the outlet at the side of the module. The highest lumen pressure (red) is near the inlet and drops as the fluid travels down the length of the module. The shade plot clearly shows that the lumen outlet pressure is still relatively high. It is also clear from fig. 33 that there is no radial lumen pressure gradient, confirming eqn. [3.37]. Thus one can deduce that the lumen pressure at a specific axial position is the same in all fibres, whether the fibres are located at the centre of the module or near the circumference.

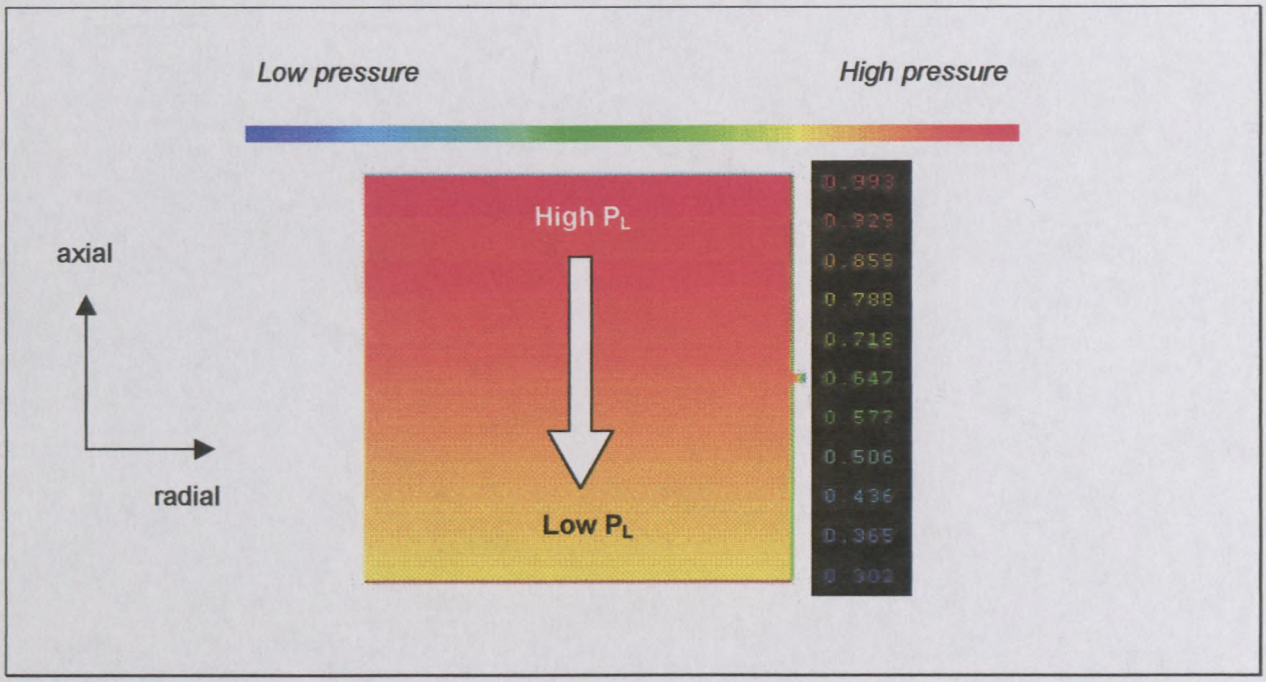

Fig. 33 : Shade plot of lumen side pressure distribution (cross-flow, downflow).

Fig. 34 shows the shell side pressure distribution. Red to orange indicates regions of high pressure, while blue denotes low pressures. The radial pressure distribution is once again uniform. This leads one to believe that at a specific axial position, filtering is equally efficient near the centre of the module than near the circumference. Hence no stagnant flow regions. As one would expect, the region of lowest pressure is in the vicinity of the permeate outlet.

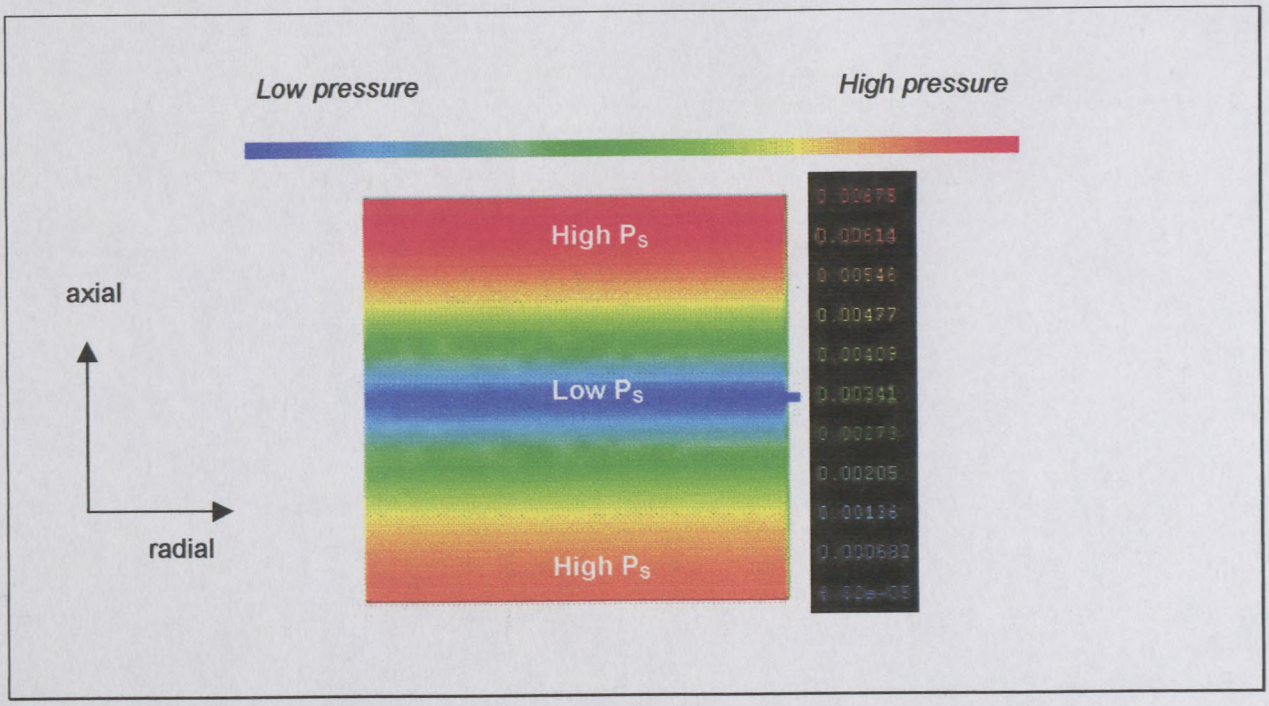

Fig. 34 : Shade plot of shell side pressure distribution (cross-flow, downflow).

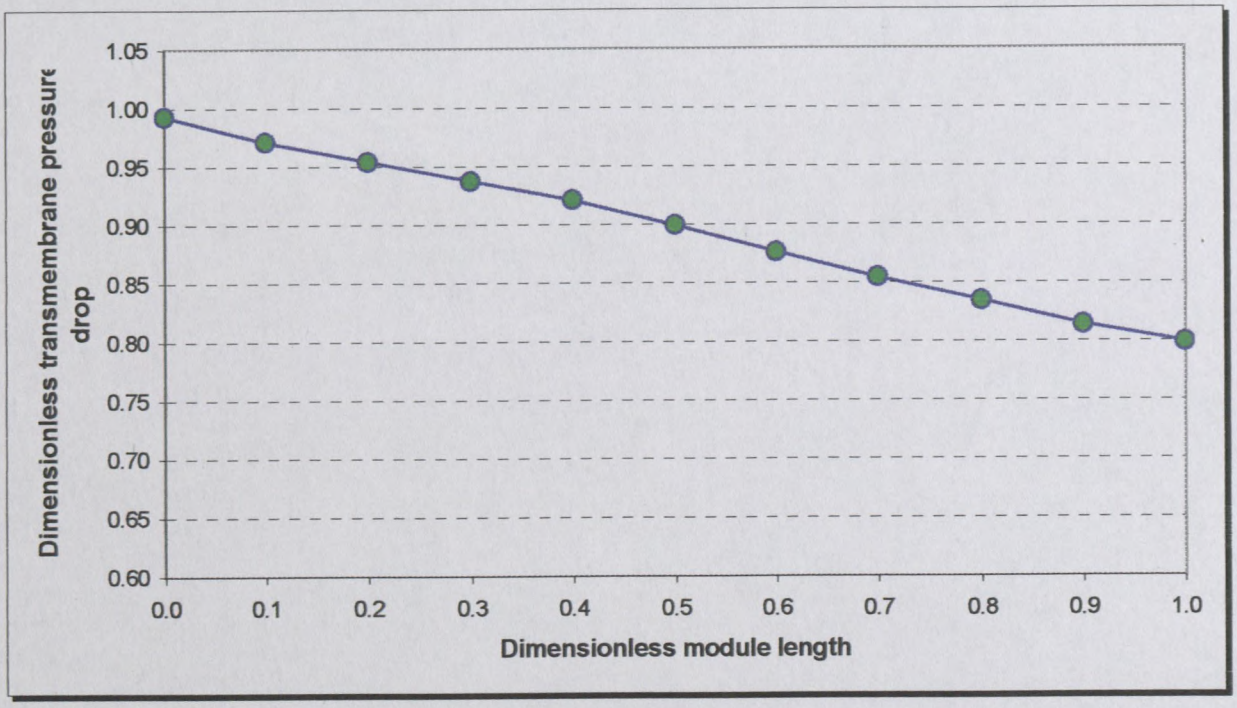

Fig. 35 : Transmembrane pressure drop as a function of module length (cross-flow, downflow).

The driving force of filtration is the difference between the lumen and shell side pressures. In fig. 35 one can see the gradual fall in transmembrane pressure drop down the module length. The lumen pressure totally dominates the shell side pressure and one has to look at fig. 36 to see the pressure distribution on the shell side. It is clear that the lowest pressure occurs at the permeate outlet, which is situated halfway down the length of the module. The shell side pressure near the lumen exit is slightly lower than the shell side pressure near the lumen inlet due to the drop in lumen pressure.

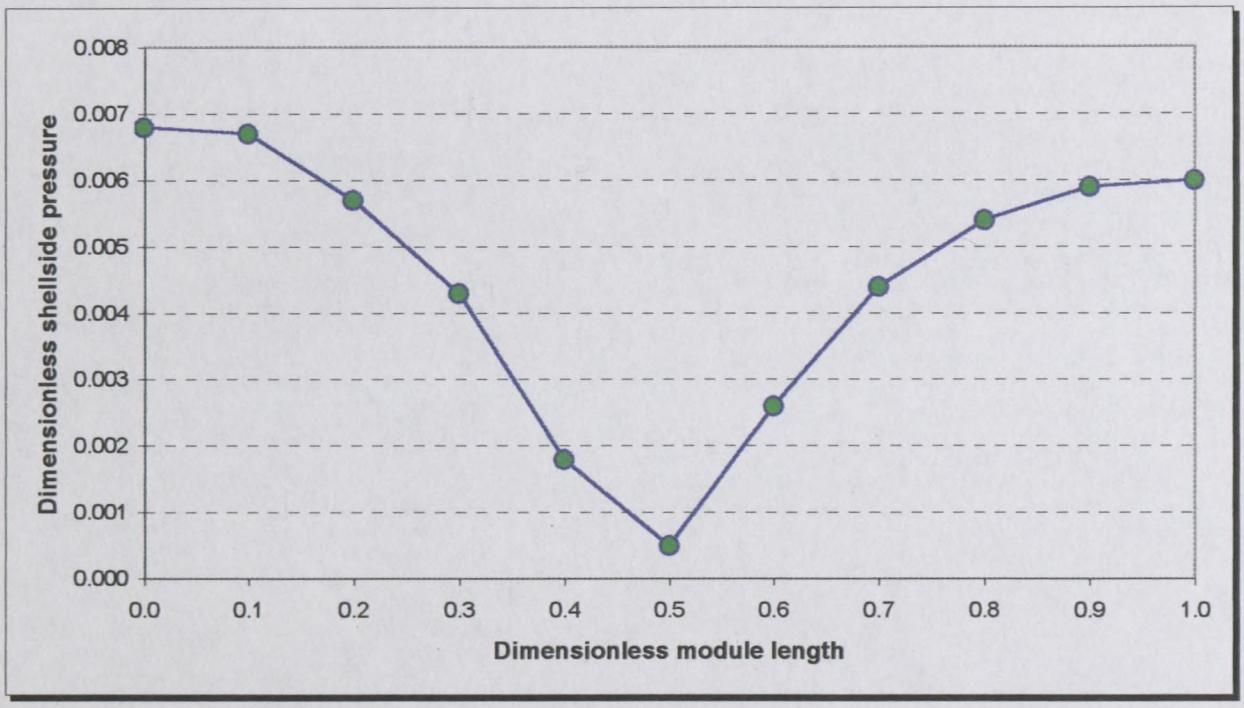

Fig. 36 : Shell side pressure as a function of module length (cross-flow, downflow).

Fastflo can also draw velocity arrows for the flows on the lumen and shell sides. The longer the arrows, the bigger the flow velocity. From fig. 37, one can see the lumen flow is more or less uniform throughout the module, except for the region near the permeate outlet, where there is a significant concentration of the arrows. The reason for this is probably because of the suction effect at the permeate outlet, which causes the fluid on the lumen side near the permeate outlet to temporarily experience an increase in velocity. This increase in velocity makes the arrows longer, which could be an explanation for the concentration.

The velocity arrows of flow on the shell side are very different from those on the lumen side. Fig. 38 shows that the shell side flow is much slower (very short arrows) than the lumen side flow, with almost no flow near the module lumen inlet and lumen exit. Thus the existence of dead spaces on the shell side in these regions cannot be ruled out. There is a notable increase in velocity (longer arrows) near the permeate outlet as fluid accelerates towards the draw-off point, hence the concentration of arrows in that region.

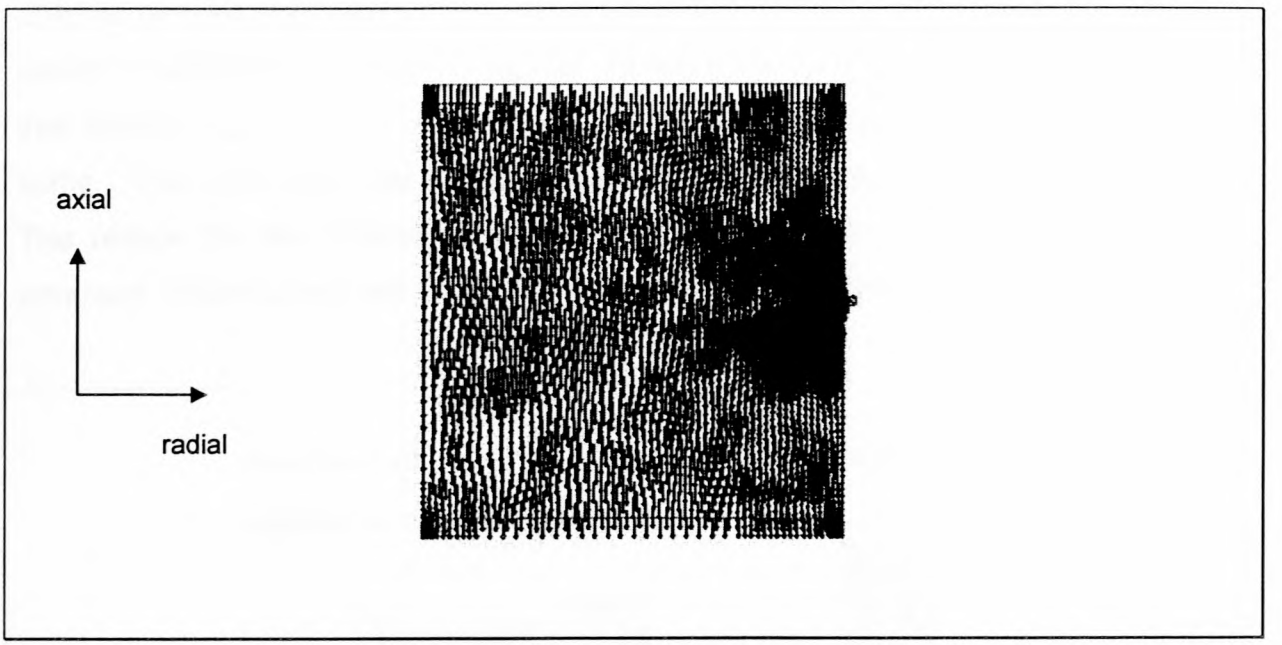

Fig. 37 : Velocity arrows of flow on the lumen side (cross-flow, downflow).

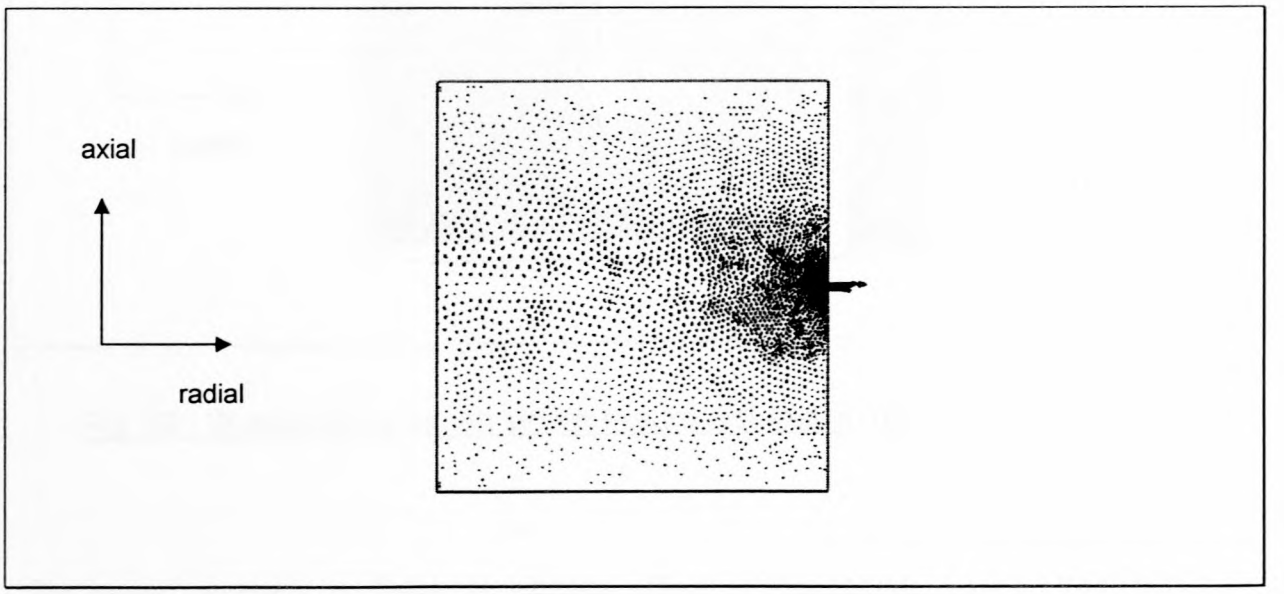

Fig. 38 : Velocity arrows of flow on the shell side (cross-flow, downflow).

6.8.2 Pressure distributions during backwash

It is also possible to investigate the backwash process by looking at the pressure distributions. In order to backwash, the pressure on the shell side is increased so that it exceeds the lumen side pressure, resulting in reverse-filtration. In all the following examples, the shell side inlet pressure was set to 200 kPa, compared to the lumen inlet pressure of 150 kPa. Shell side fluid is forced back into the lumen in order to remove the fouling layer from the membranes on the lumen side. The lumen pressure distribution is shown in fig. 39. At first it seems that the pressures are lower than those in fig. 33, but a closer inspection reveals that the numerical values are the same. The inlet and outlet lumen pressures in fig. 39 are equal to those in fig. 33. The reason for the difference in shading is that red is assigned to the highest pressure, which is the shell side backwash feed pressure, as shown in fig. 40.

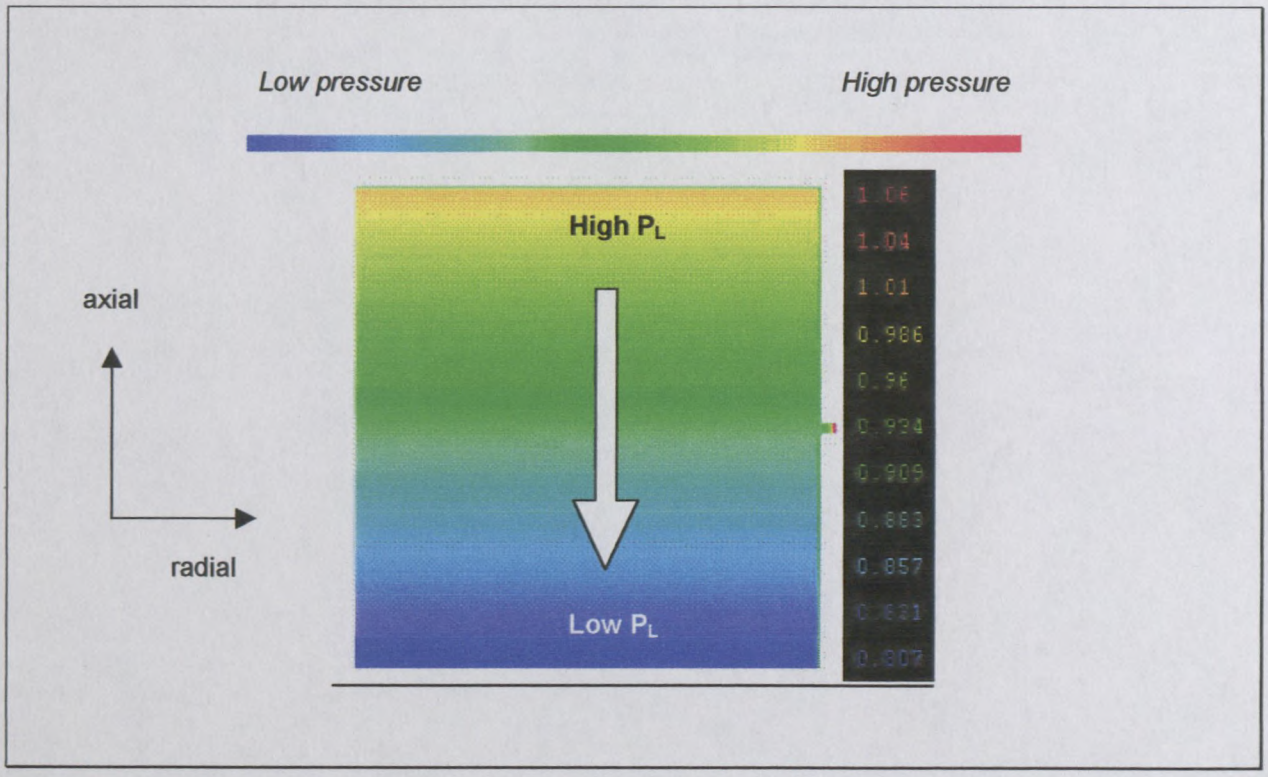

Fig. 39 : Shade plot of lumen side pressure distribution (backwash, downflow).

Backwash appears to have its biggest effect in the region around the permeate outlet, as the pressure is the highest there. The axial pressure distribution is

symmetric, even though a lighter shade of blue is observed near the lumen exit in fig. 40 Fig. 41 reveals this symmetry.

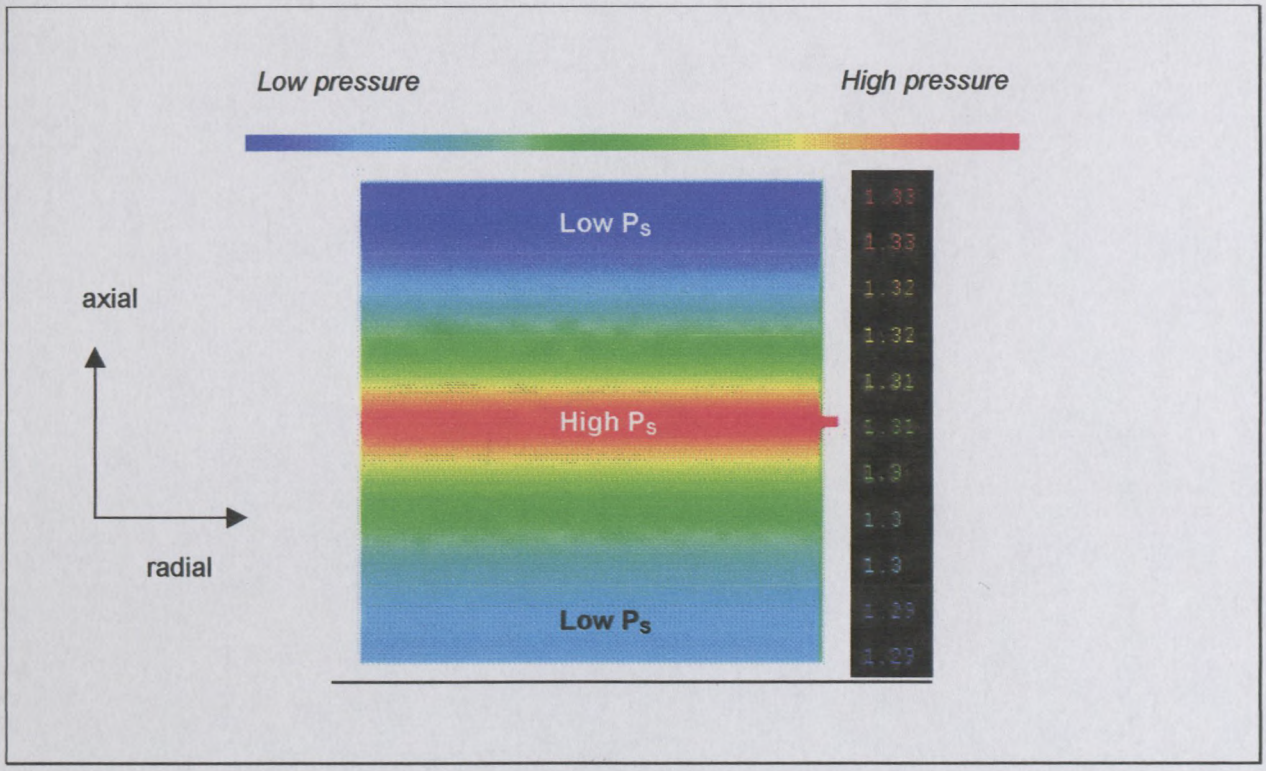

Fig. 40 : Shade plot of shell side pressure distribution (backwash, downflow).

Fig. 41 : Shell side pressure as a function of module length (backwash, downflow).

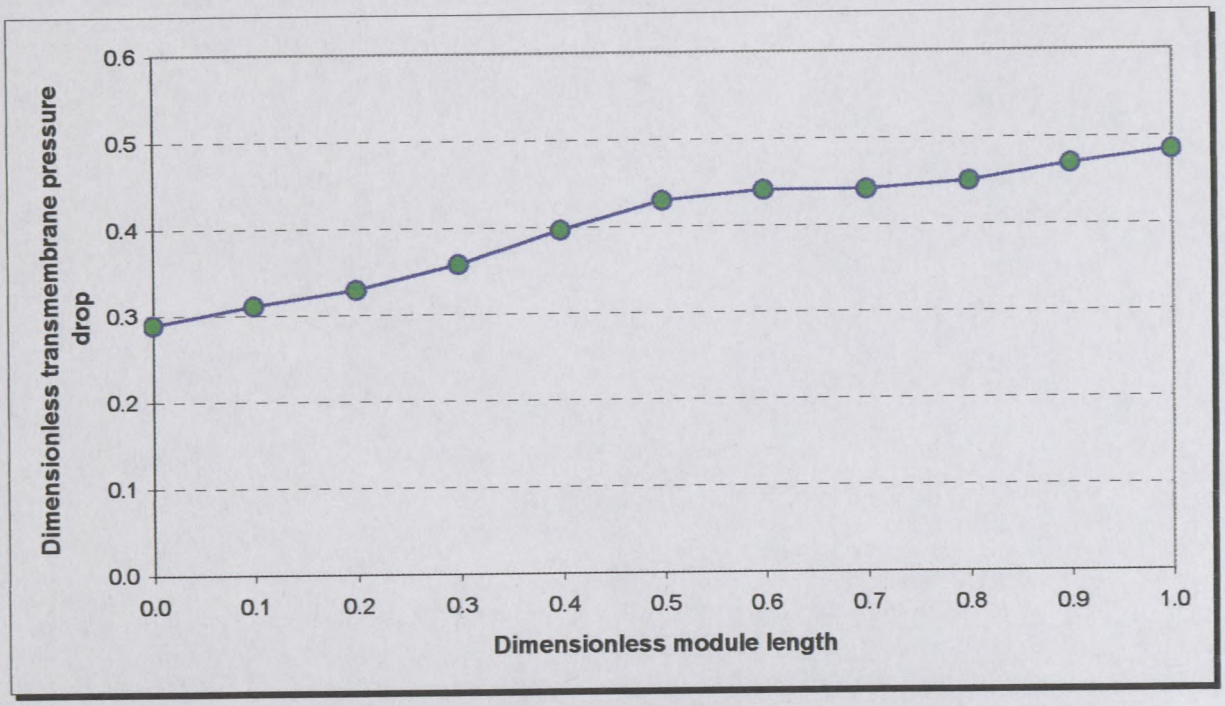

Fig. 42 : Transmembrane pressure drop as a function of module length (backwash, downflow).

However, from fig. 42 it is clear that backwash exerts its greatest effect near the lumen exit. The effect of the "spike" in shell side pressure halfway down the length of the module in fig. 41 can also be seen in fig. 42. As the shell side pressures near the lumen inlet and exit are the same and the lumen exit pressure is significantly lower than the lumen inlet pressure, the greatest transmembrane pressure drop occurs near the lumen exit. Backwash would thus be the most effective near the lumen exit for lumen flow that enters the module at the top end and leaves at the bottom end. From this it is logical to conclude that the lumen flow direction should be reversed from downflow to upflow in order for backwash to have its greatest effect at the opposite (top) end of the module. This is shown in fig. 43. Lumen flow now exits the module at the top end, where the biggest transmembrane pressure drop occurs. As the shell side pressure distribution is still the same (fig. 41), the effect of the "spike" can once again be seen in fig. 43, halfway down the length of the module.

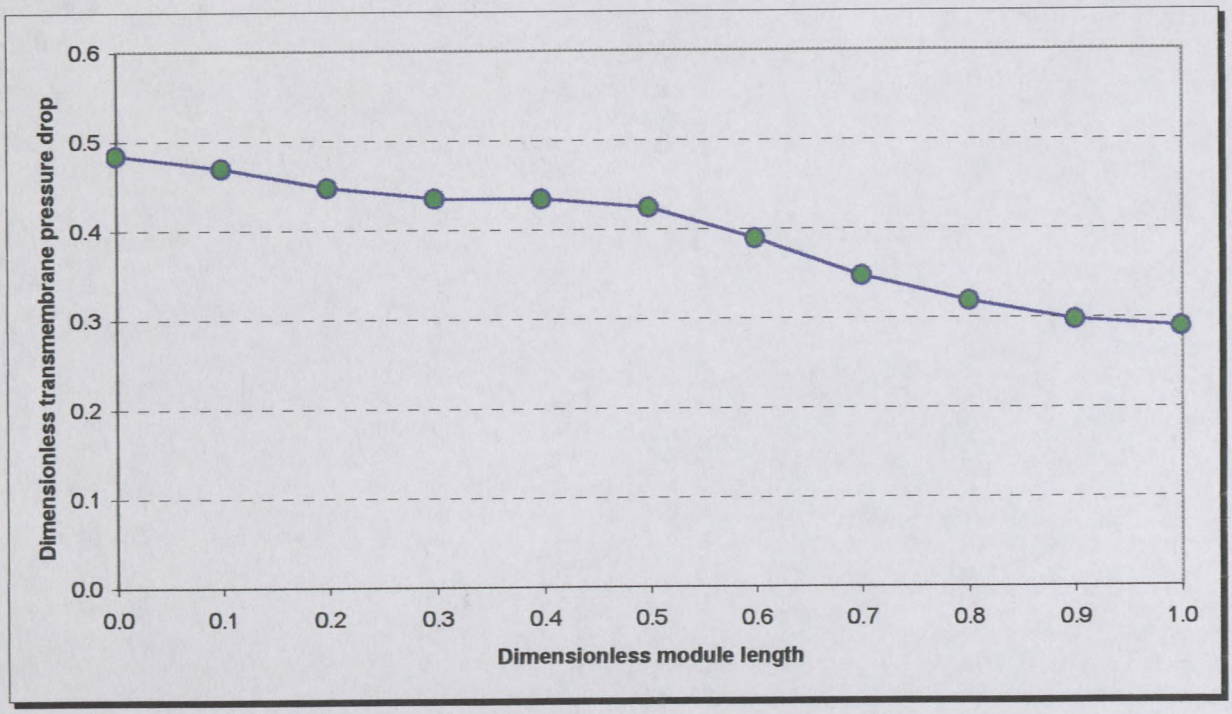

Fig. 43 : Transmembrane pressure drop as a function of module length (backwash, upflow).

In addition to switching the lumen flow direction from downflow to upflow, the position of the permeate outlet port, through which backwash fluid is pumped, can also be changed.

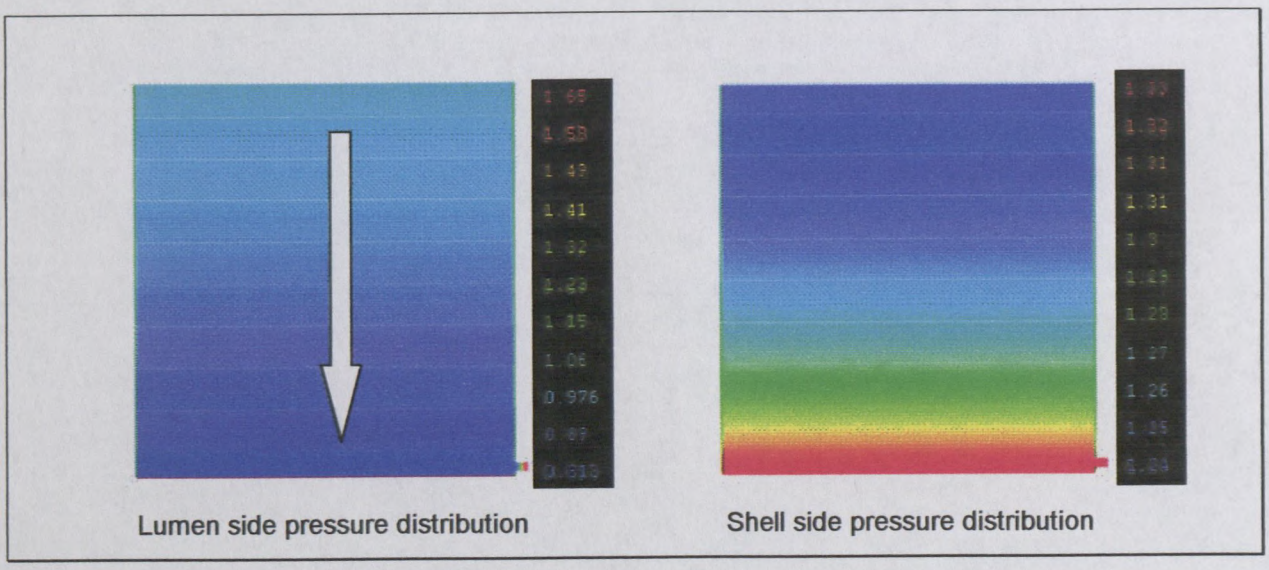

Fig. 44 : Pressure distributions for backwash at the bottom end.

Fig. 44 shows the pressure distributions for the backwash process with the permeate outlet port located near the bottom end of the membrane module. Note that the dark blue on the lumen side has a different numerical value than the dark blue on the shell side. The different colours merely indicated regions of high and low pressures. The colours of each flow region (i.e. lumen side or shell side) have their own numerical values. In fig. 45, it is clear that the highest backwash pressure occurs near the permeate outlet port and then gradually drops toward the top end of the module. The "spike" in fig. 41 has now moved to the bottom end of the module.

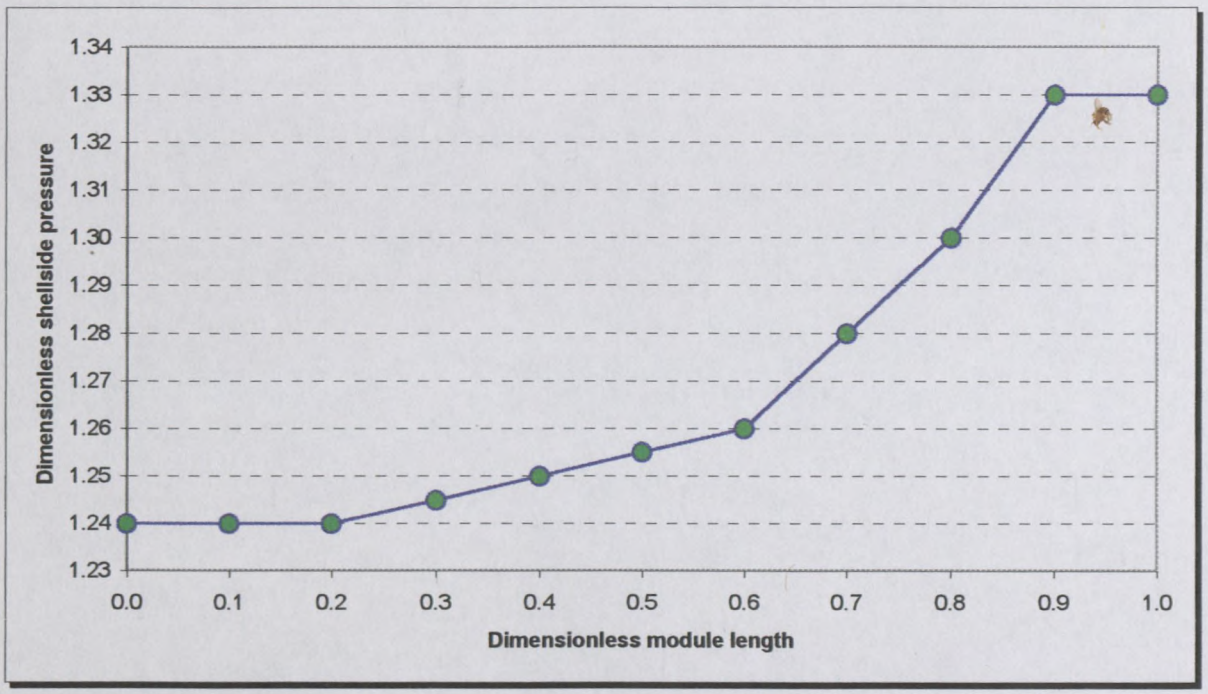

Fig. 45 : Shell side pressure as a function of module length (backwash, bottom end).

The net effect of backwash is shown in fig. 46. Since the shell side pressure rises and the lumen side pressure drops from the top end of the module toward the bottom end, the net effect is a rise in transmembrane pressure drop along the length of the module from top to bottom. This is because the shell side pressure exceeds the lumen side pressure. The backwash is thus most efficient near the bottom end of the module.

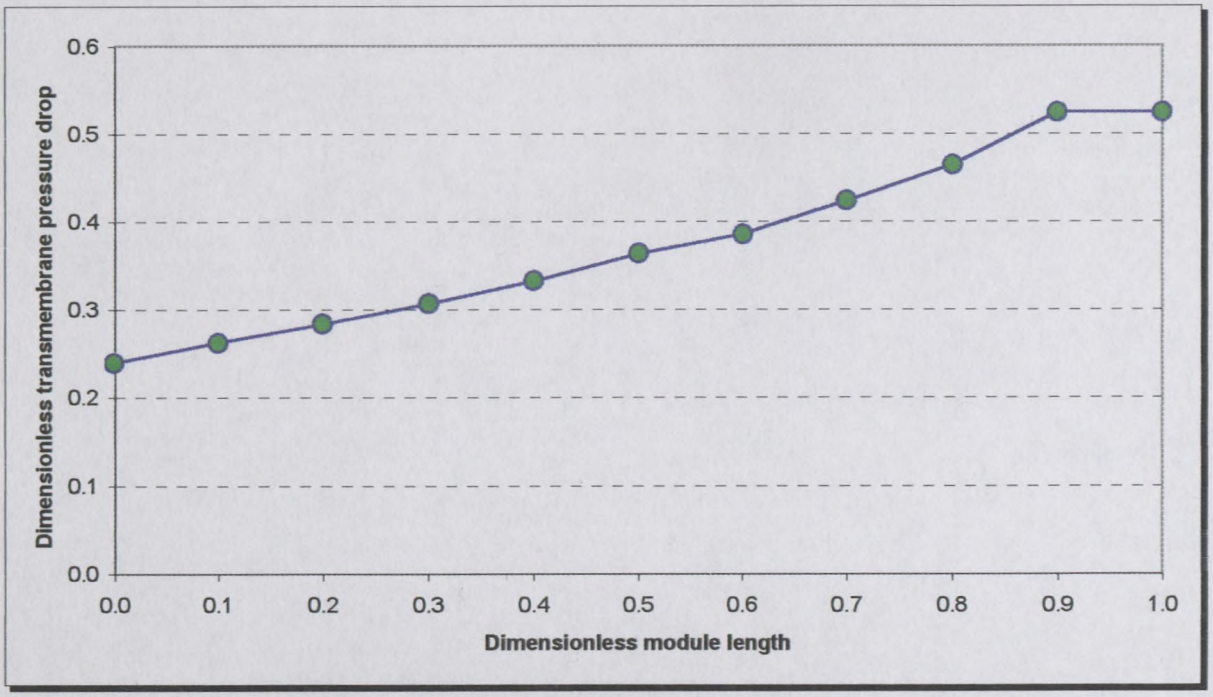

Fig. 46 : Transmembrane pressure drop as a function of module length (backwash, bottom end).

Next, the permeate outlet port is moved to the top end of the module, with lumen side flow still flowing in a downward fashion. This is shown in fig. 47 below. As backwash fluid enters the module near the top end, both the lumen side and shell side pressures drop from the top end of the module towards the bottom end.

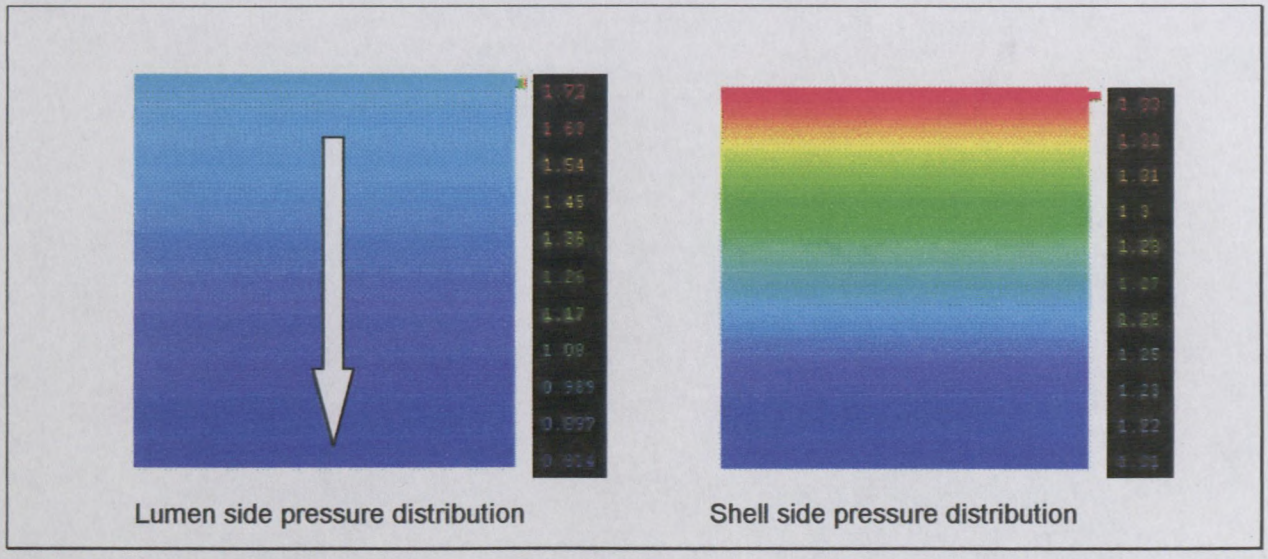

Fig. 47 : Pressure distributions for backwash at the top end.

Fig. 48 shows how the shell side pressure drops down the length of the module. The pressure drop in the first half of the module length is relatively steep, but slows down in the second half, until the pressure reaches a constant value in the bottom 20% of the module length.

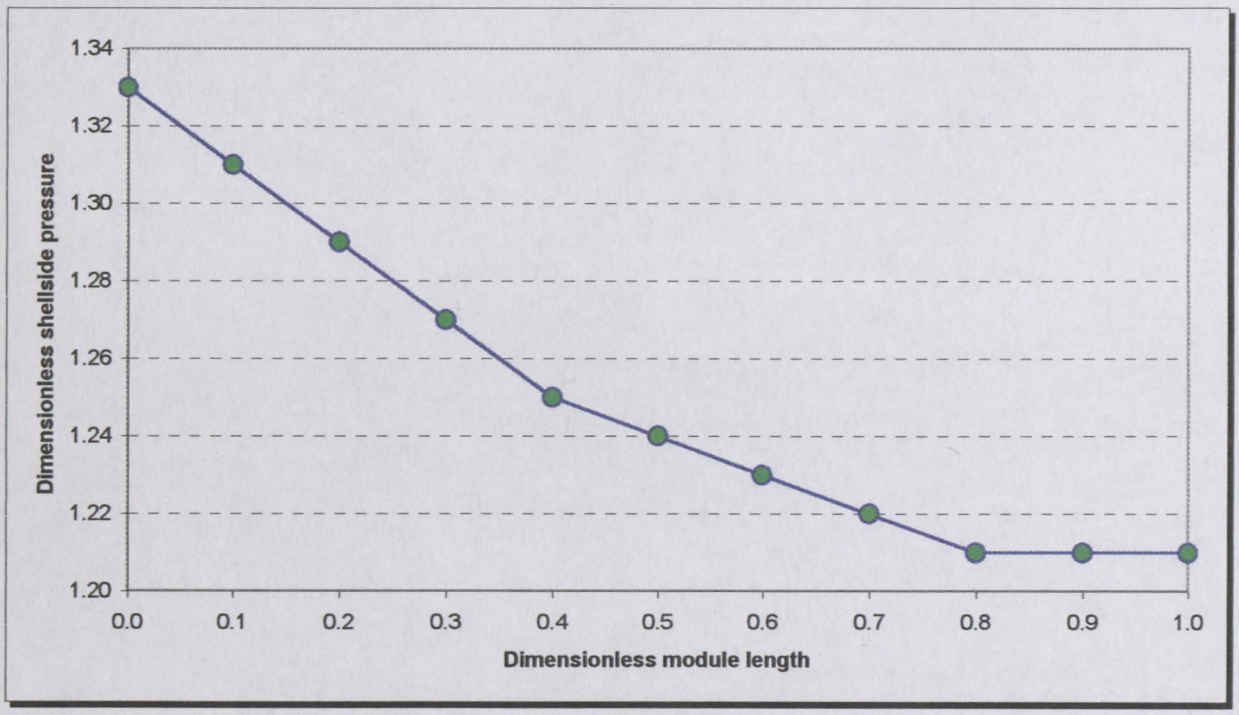

Fig. 48 : Shell side pressure as a function of module length (backwash, top end).

Fig. 49 shows the net effect of backwash. One would have expected the highest transmembrane pressure drop near the top end of the module, but fig. 49 shows that backwash is once again most efficient near the bottom end of the module. However, when comparing fig. 49 with fig. 46, it is clear that there is less variation in transmembrane pressure drop between the top end and the bottom end, when using the permeate outlet near the top end of the module for backwash.

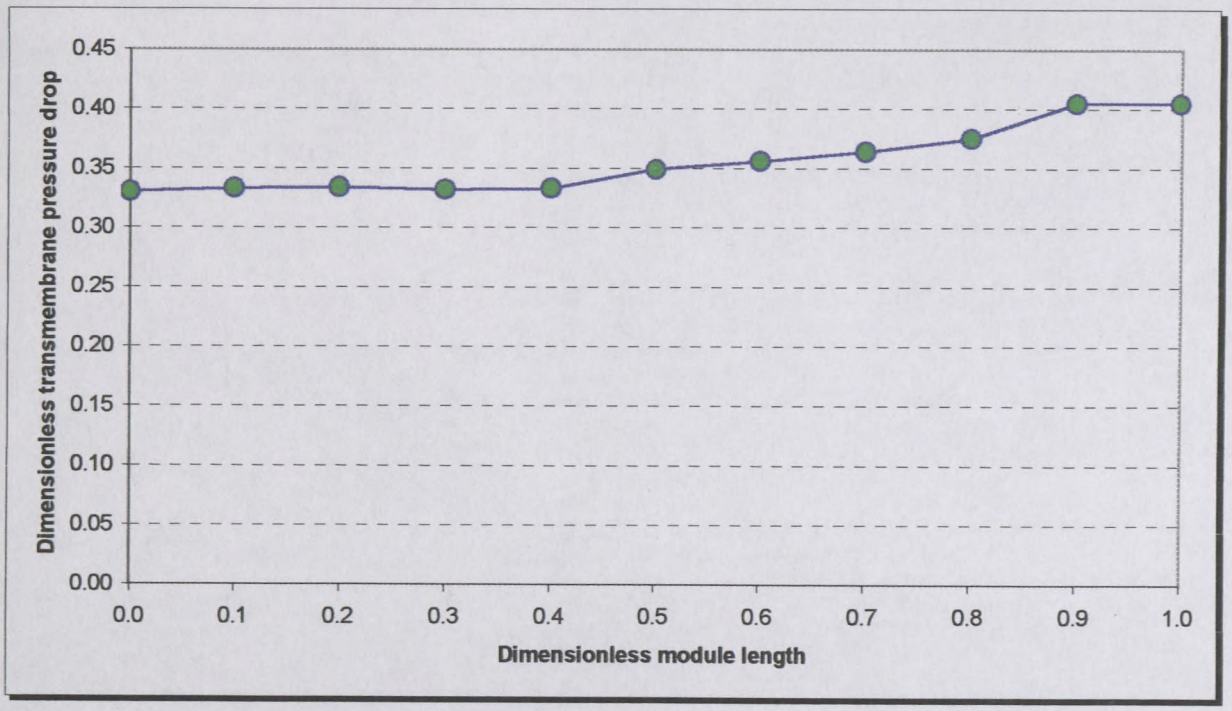

Fig. 49 : Transmembrane pressure drop as a function of module length (backwash, top end).

6.8.3 Effect of changing membrane permeability

It is clear from the previous discussions that the model is essentially one-dimensional, i.e. no radial pressure gradients on the shell side. At a membrane permeability of 2.3 $\times 10^{-13}$ m, the membranes are not very porous. Increasing the membrane permeability will result in more porous membranes and this could show if the shell side pressure distribution is still one-dimensional at high permeabilities. Figs. 50, 51 and 52 shows the effect of changing membrane permeability. In fig. 50 (L_p = 1 $\times 10^{-12}$ m), the permeability is still relatively low and the transmembrane pressure drop is quite significant. This is also evident from the numerical values in the column to the right of each figure. Increasing the permeability to 1 $\times 10^{-10}$ m in fig. 51, a difference can already be seen in the shade plots of the lumen side pressure distribution. The lumen pressure distribution is starting to look more like that on the shell side, with a minimum pressure observable halfway down the length of the module, instead of just a gradual decrease in pressure as in fig. 50. At very low membrane permeabilities, there is a linear decrease (fig. 50) in lumen pressure in the axial direction, but as the permeability is increased, the lumen pressure drops to a

minimum halfway down the length of the module before increasing again (fig. 51). Comparing the numerical values of the pressures on the shell side in figs. 50 and 51, it is clear that the pressures on the shell side are significantly higher in fig. 51. This shows that fluid flows much easier to the shell side at higher permeabilities, resulting in a smaller difference between the pressures on the lumen and shell sides.

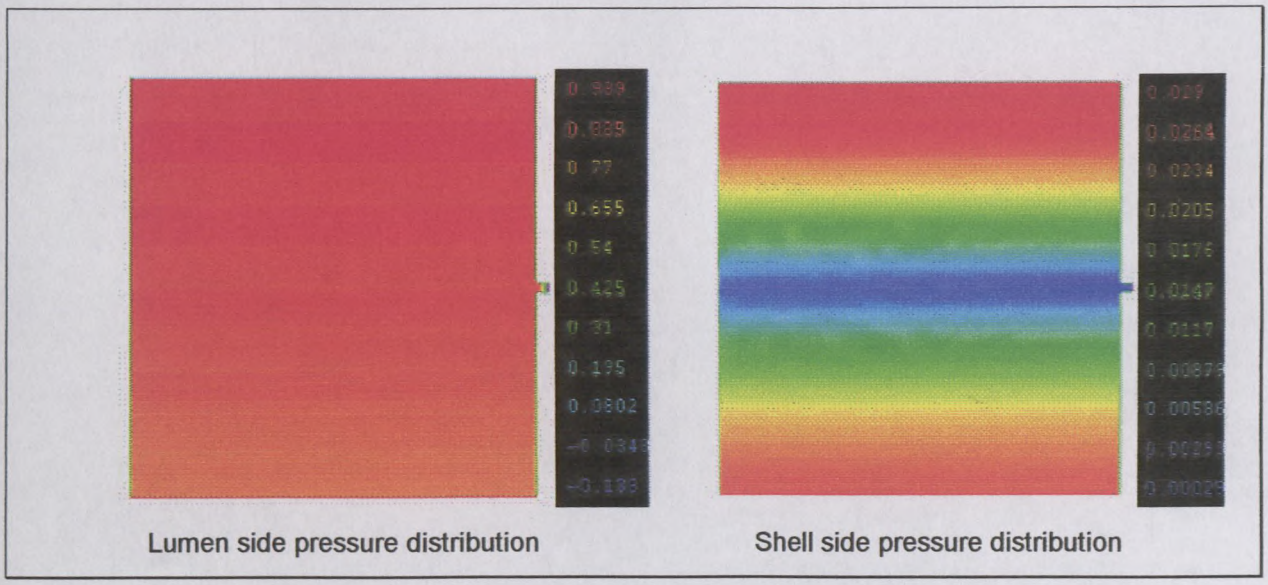

Fig. 50 : Pressure distributions for a membrane permeability of 1 $\times 10^{-12}$ m.

Finally the membrane permeability is increased to 1 $\times 10^{-08}$ m, with the result shown in fig. 52. The membranes are now so porous, that they basically do not exist anymore. The pressures on the lumen and shell sides are almost equal (see numerical values), as are the pressure distributions. Both the lumen and shell side pressures experience a minimum pressure halfway down the length of the module near the permeate outlet. However, it is clear that even at a very high membrane permeability, the model is still one-dimensional, as transmembrane pressure drop is small compared to the shell side pressure drop. When looking at the Darcy permeabilities, $k_{x,L}$ and $k_{r,S}$, only $k_{x,S}$ is significant, probably due to the aspect ratio, $\left(\frac{L_{eff}}{r_c}\right)^2$.

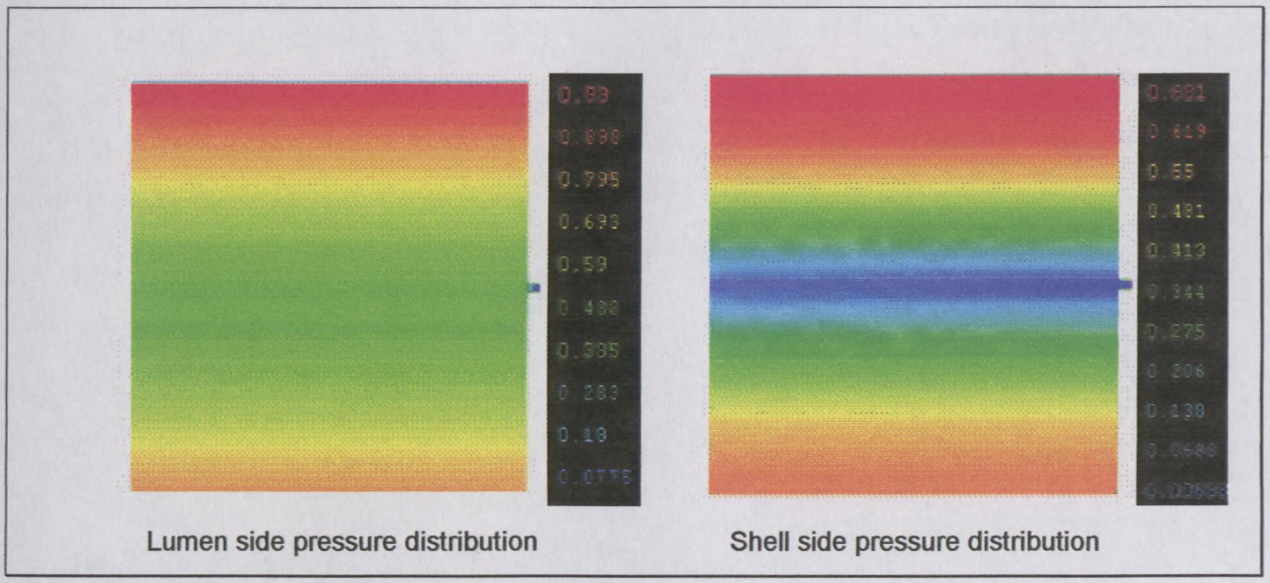

Fig. 51 : Pressure distributions for a membrane permeability of 1 $\times 10^{-10}$ m.

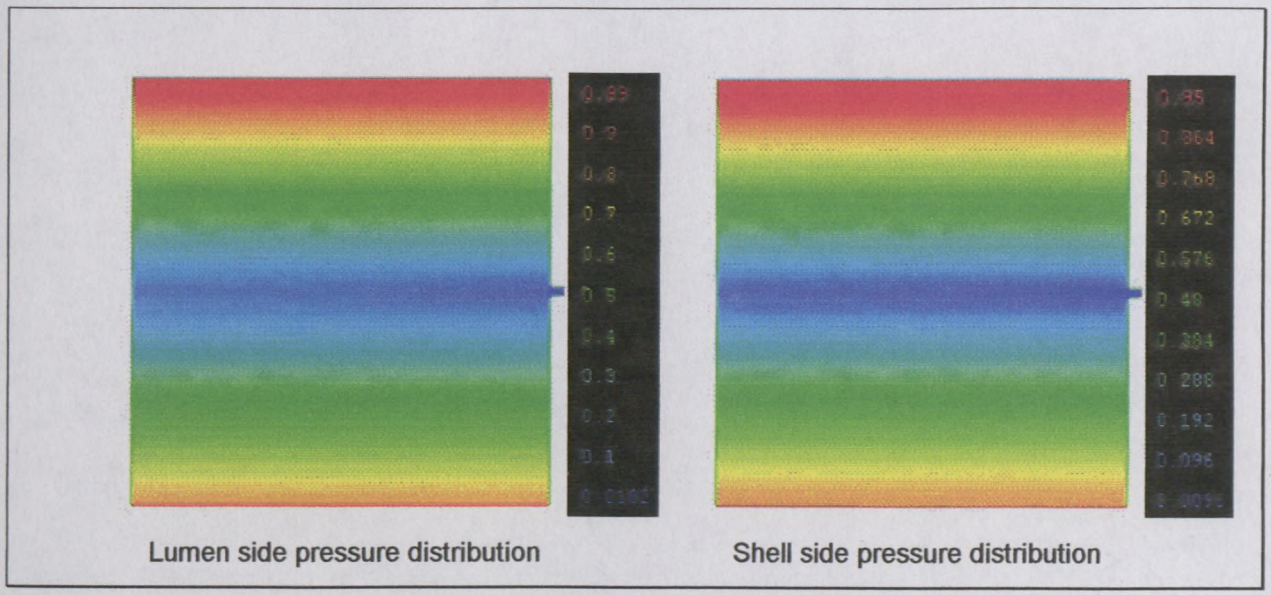

Fig. 52 : Pressure distributions for a membrane permeability of 1 $\times 10^{-08}$ m.

~~~
~~~

Chapter 7

CONCLUSIONS AND RECOMMENDATIONS

This project was mostly a theoretical study to simulate the ultrafiltration of potable water through a hollow-fibre membrane module. Various hydrodynamic models were considered for modelling purposes. Most of these models were based on the Krogh cylinder model (KCM), where one fibre is representative of the whole fibre bundle. The advantage of the KCM is that it is simple to use and produces an analytical result. The drawback however, is that it cannot account for macroscopic radial gradients, nor can it take into account the effect of wet fibre expansion. The fibres were found to expand an average of 0.67% in the axial direction when wetted. An improved model, the Porous Medium Model (PMM), does consider these effects and it was thus used in this study to model the flow through a hollow-fibre membrane module. Also, the PMM can be extended to account for any specific detail of module design.

The PMM is more complex than the KCM to use, since it does not produce an analytical solution, but two second-order coupled partial differential equations. Therefore numerical methods like the finite difference method or the finite element method must be used. The finite element method was chosen in this study, since it is more flexible than the finite difference method in modelling complex geometries. The finite element software package *Fastflo* was used in this study, as it can handle domains with complex shapes and uses its own high level language by which PDEs are solved.

The following two PDEs formed the basis of the PMM in this study:

$$k_{x,L}\frac{\partial^2 p_L}{\partial x^2} = L_p A_v (p_L - p_S)$$

and

$$-k_{r,S}\frac{1}{r}\frac{\partial}{\partial r}\left(r\frac{\partial p_S}{\partial r}\right)-k_{x,S}\frac{\partial^2 p_S}{\partial x^2}=L_p A_v(p_L-p_S)$$

Since the PMM is a two-dimensional model, the permeate outlet had to be modelled as a slit right around the module, to change the actual geometry from 3-D to 2-D. The result was that the module was axisymmetric and only one half of the module (in the radial direction) needed be considered for modelling purposes. The necessary boundary conditions were applied and the PDEs were solved for the lumen and shell side pressure distributions.

However, the membrane permeability, L_p, had to be determined first and this was done through a combination of numerical and experimental work, using the dead-end configuration. A correction plot was obtained and L_p was found to be 2.3×10^{-13} m. At this value, the Krogh Cylinder Model can be used, but the PMM was chosen as it is more flexible with regards to module design.

Having obtained L_p, the PMM was numerically solved for various combinations of module outer diameter and length, keeping all other variables constant. The PMM results were obtained in terms of permeate flux predictions. A physical experiment was also done to validate the model. Different inlet conditions of pressure and flow rate was used and it was found that the average error between the numerical and experimental results was only 2.6%. This confirmed the suitability of the PMM to simulate the actual filtration process.

The effect of the positioning of the permeate outlet was investigated. The upstream and downstream positions were used, as well as halfway down the length of the module. It appeared that the position becomes more important as the module length increases, as the difference between flux predictions for the various permeate outlet positions became greater with an increase in module length. The upstream outlet position produced the highest flux, which can be attributed to the fact that some of the fluid bypasses directly from the lumen inlet to the permeate outlet. The further from the lumen inlet the permeate outlet position is, the more resistance to flow there is, resulting in a lower flux.

The permeate flux increased sharply with an increase in module outer diameter, but tapered off from a diameter of 50mm and larger. There was no noticeable increase in flux for module outer diameters greater than 200mm.

In order to find which module length and outer diameter would be the most economical, the permeate flow rate produced by each module geometry was expressed in terms of a cost per unit volume permeate produced (cent per kL). Cost was calculated from the cost of pumping energy (operating cost) and the cost of the membranes and modules (capital cost). The capital cost was multiplied by a capital recovery factor (CRF) of 0.3 to place it on the same basis as operating cost. It was found that the optimum module dimensions are a length of 0.6m and an outer diameter between 90mm and 160mm. Module diameters smaller than 90mm are too expensive, while no benefit is obtained from diameters in excess of 160mm.

Finally, some clues about filtration could be obtained by looking at the visual representation of the pressure distributions and velocity arrows of flows on the lumen and shell sides. Shade plots are useful to show how pressure is distributed on the lumen side and especially on the shell side, in order to identify stagnant flow areas and to see where the most filtering is being done. Velocity arrows indicate the speed and direction of fluid flow, but can also indicate regions of stagnant flow. The pressure distributions obtained during the backwash process showed that the backwash process is most effective at the downstream end of the lumen flow, when the backwash fluid enters the module halfway down its length. This means that the lumen flow should be reversed in order to clean both ends of the hollow fibres properly. Instead of reversing the lumen flow direction, the effect of permeate outlet position on the effectiveness of backwash, was also investigated. It was found that the greatest transmembrane pressure drop during backwash occurred at the lumen downstream end, irrespective of whether the permeate outlet port was located near the lumen inlet or outlet. However, there was less variation in transmembrane pressure drop down the length of the module when the backwash fluid entered the module near the lumen inlet end of the module.

Since this study only involved pure water without any foulants, it is recommended that further work be done to include the effects of fouling and concentration

polarisation, so as to more closely simulate a real world scenario. A time variable must also be introduced, which will have a significant impact on the format of *Fastflo*'s problem file. The work by Serra *et al.* (1995) can be used as a basis for the above. They simulated fouling during the filtration phase and cleaning during the backwash phase to predict the net production rate during an operating cycle. The main module characteristics, namely fibre outer diameter, fibre length, packing density, membrane permeability and fibre wall thickness must be varied to find the combination that maximizes the net production rate. The effects of operating conditions (such as threshold pressure and feed flow rate) and feed properties (such as temperature and concentration of feed suspension) can also be investigated. Finally, the economics of such a process can be calculated by incorporating energy costs.

~~~
~~~

References

Aimar, P., Howell, J.A., Clifton, M.J., & Sanchez, V. (1991). Concentration polarisation build-up in hollow-fibres: a method of measurement and its modelling in ultrafiltration. J. Membrane Sci., 59, 81-99.

Anderson, J.D., Jr. (1995). Computational Fluid Dynamics: The basics with applications. New York: McGraw-Hill, Inc.

Apelblat, A., Katzir-Katchalsky, A., & Silberberg, A. (1974). A mathematical analysis of capillary-tissue fluid exchange. Biorheology, 11, 1-49.

Belfort, G. (1989). Fluid mechanics in membrane filtration: recent developments. J. Membrane Sci., 40, 123-147.

Bird, R.B., Stewart, W.E., & Lightfoot, E.N. (1960). Transport Phenomena. New York: John Wiley & Sons.

Bosch, J.P. (1993). Hemodialysis. High-efficiency treatments. New York: Churchill Livingstone.

Botes, J.P. (1995). UF as a single-step clarification and disinfection process for potable water supply to rural or farming communities. Unpublished research report, University of Stellenbosch.

Botes, J.P. (2000). Flux enhancement using flow destabilisation in capillary membrane ultrafiltration. Masters thesis, University of Stellenbosch.

Breslau, B.R., Testa, A.J., Milnes, B.A., & Medjanis, G. (1980). Advances in hollow-fibre UF technology. In A.R. Cooper (ed.), Polymer Science and Technology (vol. 13). New York: Plenum Press.

Brigham, E.F., & Houston, J.F. (1998). Fundamentals of Financial Management (8th ed.). Fort Worth, Texas: The Dryden Press.

Brinkman, H.C. (1947). A calculation of the viscous force exerted by a flowing fluid on a dense swarm of particles. Appl. Sci. Res., A1, 27-34.

Bruining, W.J. (1989). A general description of flows and pressures in hollow-fibre membrane modules. Chem. Engng Sci., 44, 1441-1447.

Cabassud, C., Anselme, C., Bersillon, J.L., & Aptel, P. (1991). UF as a nonpolluting alternative to traditional clarification in water treatment. Filtration & Separation, May/June 1991, 194-198.

Cabassud, C., Laborie, S., & Lainé, J.M. (1997). How slug flow can improve UF flux in organic hollow fibres. J. Membrane Sci., 128, 93-101.

Carey, G.F., & Oden, J.T. (1986). Finite Elements : Fluid Mechanics. Englewood Cliffs, New Jersey: Prentice-Hall.

Carman, P.C. (1937). Fluid flow through granular beds. Trans. Instn Chem. Engrs, 15, 150-166.

Cheryan, M. (1998). UF and Microfiltration Handbook. Pennsylvania: Technomic Publishing Co., Inc.

Chick, W.L., Like, A.A., & Lauris, V. (1975). Beta cell culture on synthetic capillaries: an artificial endocrine pancreas. Science, 187, 847-849.

Connor, J.J., & Brebbia, C.A. (1976). Finite Element Techniques for Fluid Flow. London: Butterworth & Co. (Publishers) Ltd.

Coulson, J.M., & Richardson, J.F. (1991). Chemical Engineering (vol. 2). Oxford: Butterworth-Heinemann.

CSIRO. (1997). Fastflo Tutorial Guide. Oxford: Numerical Algorithms Group Ltd.

Cui, Z.F., & Wright, K.I.T. (1996). Flux enhancements with gas sparging in downward cross-flow UF : performance and mechanism. J. Membrane Sci., 117, 109-116.

De Nevers, N. (1991). Fluid mechanics for Chemical Engineers. Singapore: McGraw-Hill, Inc.

Douglas, J.M. (1988). Conceptual design of chemical processes. Singapore: McGraw-Hill, Inc.

Fletcher, C.A.J. (1991). Computational Techniques for Fluid Dynamics (vol. 1). Berlin: Springer-Verlag.

Happel, J. (1959). Viscous flow relative to arrays of cylinders. A.I.Ch.E.J., 5, 174-177.

Henwood, D., & Bonet, J. (1996). Finite Elements: A Gentle Introduction. London: Macmillan.

Iritani, E., Hayashi, T., & Murase, T. (1991). Analysis of filtration mechanism of cross-flow upward and downward UF. J. Chem. Engng Japan, 24, 39-44.

Jacobs, E.P. (1998). Personal communication.

Kelsey, L.J., Pillarella, M.R., & Zydney, A.L. (1990). Theoretical analysis of convective flow profiles in a hollow-fibre membrane bioreactor. Chem. Engng Sci., 45, 3211-3220.

Kleinstreuer, C., & Agarwal, S.S. (1986). Analysis and simulation of hollow-fibre bioreactor dynamics. Biotechnol. Bioengng, 28, 1233-1240.

Krogh, A. (1919). The number and distribution of capillaries in muscles with calculations of the oxygen pressure head necessary for supplying the tissue. J. Physiol., 52, 409-415.

Labecki, M., Piret, J.M., & Bowen, B.D. (1995). Two-dimensional analysis of fluid flow in hollow-fibre modules. Chem. Engng Sci., 50, 3369-3384.

Lee, Y., & Clark, M.M. (1997) A numerical model of steady-state permeate flux during cross-flow UF. Desalination, 109, 241-251.

Matsumo, K., Katsuyama, M., & Ohya, H. (1987). Separation of yeast by cross-flow filtration with back-washing. J. Ferment. Technol., 65 (1), 77-83.

Matsumo, K., Katsuyama, M., & Ohya, H. (1988). Cross-flow microfiltration of yeast by microporous ceramic membrane with backflushing. J. Ferment. Technol., 65 (2), 199.

Mercier, M., Fonade, C., & Lafforgue-Delorne, C. (1997). How slug flow can enhance the ultrafiltration flux in mineral tubular membranes. J. Membrane Sci., 128, 103-113.

Mulder, M. (1991). Basic principles of membrane technology. Boston: Kluwer.

Nakatsuka, S., Nakate, I., & Miyano, T. (1996). Drinking water treatment by using UF hollow-fibre membranes. Desalination, 106, 55-61.

Norrie, D.H., & De Vries, G. (1973). The Finite Element Method. New York: Academic Press, Inc.

Pangrle, B.J., Alexandrou, A.N., Dixon, A.G., & DiBiasio, D. (1991). An analysis of laminar fluid flow in porous tube and shell systems. Chem. Engng Sci., 46, 2847-2855.

Patkar, A.Y., Koska, J., Taylor, D.G., Bowen, B.D., & Piret, J.M. (1995). Protein transport in UF hollow-fibre bioreactors. A.I.Ch.E.J., 41, 415-425.

Park, J.K., & Chang, H.N. (1986). Flow distribution in the fibre lumen side of a hollow-fibre module. A.I.Ch.E.J., 32, 1937-1947.

Piret, J.M., & Cooney, C.L. (1990). Mammalian cell and protein distributions in UF hollow-fibre bioreactors. Biotechnol. Bioengng, 36, 902 – 910.

Redkar, S.G., & Davis, R.H. (1993). Cross-flow microfiltration of yeast suspensions in tubular filters. Biotechnol. Prog., 9, 625.

Redkar, S., Kuberkar, V., & Davis, R.H. (1996). Modeling of concentration polarisation and depolarisation with high-frequency backpulsing. J. Membrane Sci., 121, 229-242.

Roos, L.I. (1992). Mathematical modelling of synthetic membrane morphology. Masters thesis, University of Stellenbosch.

Salmon, P.M., Libicki, S.B., & Robertson, C.R. (1988). A theoretical investigation of convective transport in the hollow-fibre reactor. Chem. Engng Commun., 66, 221-248.

Serra, C., Clifton, M.J., Moulin, P., Rouch, J.-C., & Aptel, P. (1998). Dead-end UF in hollow-fibre modules : module design and process simulation. J. Membrane Sci., 145, 159-172.

Smart, J., Starov, J.M., & Lloyd, D.R. (1996). Performance optimization of hollow-fibre reverse osmosis membranes. Part II. Comparative study of flow configurations. J. Membrane Sci., 119, 117-128.

Starov, V.M., Smart, J., & Lloyd, D.R. (1995). Performance optimization of hollow-fibre reverse osmosis membranes. Part I. Development of theory. J. Membrane Sci., 103, 257-270.

Turton, R.B., Bailie, R.C., Whiting, W.B., & Shaeiwitz. (1998). Analysis, synthesis and design of chemical processes. Upper Saddle River, New Jersey: Prentice Hall.

Wetterau, G.E., Clark, M.M., & Anselme, C. (1996). A dynamic model for predicting fouling effects during the UF of a groundwater. J. Membrane Sci., 109, 185-204.

Wijmans, J.G., Nakao, S., Van den Berg, J.W.A., Troelstra, F.R., & Smolders, C.A. (1985). Hydrodynamic resistance of concentration polarisation boundary layers in UF. J. Membrane Sci., 22, 117-135.

Wolf, C.F.W. (1980). Liver tumour cells grown on hollow-fibre capillaries : a prototype liver assist device. Polym. Sci. Technol., 13, 557-564.

Yeh, H.M., & Wu, H.H. (1997). Membrane UF in combined hollow-fibre module systems. J. Membrane Sci., 124, 93-105.

Yoshikawa, S., Ogawa, K., Minegishi, S., Eguchi, T., Nakatani, Y., & Tani, N. (1992). Experimental study of flow mechanics in a hollow-fibre membrane module for plasma separation. J. Chem. Engng Japan, 25, 515-521.

Yoshikawa, S., Ogawa, K., & Minegishi, S. (1994). Distributions of pressure and flow rate in a hollow-fibre membrane module for plasma separation. J. Chem. Engng Japan, 27, 385-390.

Yuan, S.W., & Finkelstein, A.B. (1956). Laminar pipe flow with injection and suction through a porous wall. Trans. ASME, 78, 719-724.

~~~
~~~

APPENDIX A : *FASTFLO* FEATURES

Main features of *Fastflo*

Fastflo's main advantage in solving PDEs is its flexibility in specifying models and algorithms to solve them. Timestepping algorithms can be used to solve time-dependent PDEs, while non-linear PDEs are solved by an iterative strategy. A PDE problem is presented to *Fastflo* via two files, one for the mesh and one for the problem specification. The use of unstructured meshes enables *Fastflo* to handle complex geometrical shapes. Systems of PDEs are also easily handled, such as the problem encountered in this study. Other PDEs which can be solved by *Fastflo*, are those encountered in fluid flow, acoustics, eigenvalue problems, elasticity and convection. In *Fasttalk*, programming is very concise, liberating the user from having to use time-consuming languages like FORTRAN. However, new users need to spend some time initially to get to know the language and all its various elements.

Fastflo operators and commands

Fastflo uses a wide range of unary and binary operators. Some binary operators involve vector operations and thus have unfamiliar meanings. They are represented by the following:

.	dot product over all scalar components yielding a single number result
@	dot product over vector components yielding a vector with one scalar value per node
p	matrix-vector product
P	matrix-matrix product
t	dyadic product of vectors
c	vector cross product

Fasttalk has a range of commands to display output for 2D problems:

- **arrow** produces an arrow diagram of two components of a vector;
- **clear** clears the graphic screen (**black** is equivalent);
- **contour** produces a contour plot of the vector;
- **prim** displays the mesh;
- **shade** produces a Gouraud shaded plot of the vector; and
- **show** (followed by an expression) gives an output describing the value of the expression.

Fastflo codes

In specifying PDE problems, certain codes are used to tell *Fastflo* how a statement must be handled. The code **e** is used when specifying equations in PDE problems. Equations may contain derivative operators, expressions involving parameters and known vectors, as well as unknowns. The code **b** indicates boundary conditions. A tag is assigned to each boundary condition, linking them to tagged sections of the boundary. Other statement codes are **A** for announcing problems, **D** for making aliases, **F** for file inclusions, **N** for naming vectors and **P** for defining parameters.

The vector stack

Global vectors are collections of numbers, with one set of components for each node. They are referred to by names such as v101, v102, v201, etc. The vector stack contains most of the information created and used by *Fastflo*. Each vector consists of a set of scalar values for each of the nodes, for example an x- and y-component for a 2-D problem. The vector stack is segmented into levels :

...	...	...
v301	v203	v303
v201	v202	v302
v101	v201	v301

Each level of the vector stack has a size equal to the number of degrees of freedom for the problem. For example, if the problem involves two velocity coordinates, then each level of the stack consists of two vectors representing the two velocity components. If there is more than one problem, the levels will be made large enough to accommodate the largest of the problems.

The first digit indicates the level of the vector stack in which the vector appears, while the last digit is used to distinguish components. When the last digit is 0, the vector refers to all components on a particular level. Thus v300 would refer to all components on level 3 of the vector stack. Local vectors are referenced by v000 and are used to write the result of a calculation to the righthand side, appearing in v100. The vector stack can be manipulated by commands like **nostack**, **push** and **popp**. **Push** increases all vectors by one level in the stack, i.e. v100 moves to v200, v200 to v300, etc. **Popp** is the inverse action of **push**, while **nostack** disables the automatic pushing and popping of the stack. The command **nostack-1** restores the default mode. The coordinate vectors **X1**, **X2** are not part of the vector stack, but can be used in expressions in the same way as vectors. They too each have one entry per node.

Vectors may be used in expressions and are the basis of many calculation procedures and graphical outputs. Global vectors will acquire values either by assembly or solution processes, or by being assigned the value of an expression. Local vectors (v000) exist only briefly during assembly and can also be assigned values within a problem environment. Once assembly is complete, the information is lost. Assignments must appear before the results are used. Boundary condition statements are implemented after element statements, so the result of an assignment on a line beginning with **b** in a statement on a line beginning with **e** cannot generally be used. Parameter values can also be set by assignment at global level.

During assembly, a sparse matrix, representing the lefthandside of an equation, and a vector, representing the righthandside, are produced. These matrices are the input to the solution procedure.

Macros

Macros are subroutines of global commands. They are used for sections of code that need to be used many times or as a collection of *Fasttalk* commands that can alternatively be entered individually in the input window. An example is:

```
< run
   Pressure
   solve
   show v100
   shade
>
```

This macro assembles the problem whose name is *Pressure*, solves the matrix system that results, prints out information about the solution (which is in the vector v100) and displays its shade plot. It is invoked by typing the name *run*. Macros are delimited by < and >.

Working with *Fastflo*

Fastflo is a general purpose PDE solver based on finite elements. Two files are used as input to *Fastflo*, one for the mesh (with the suffix ***.msh**) and one for the problem specification (with the suffix ***.prb**). These are text files which can be created in a text editor like Microsoft® Notepad. The only connection between the mesh and the problem is the set of boundary conditions applied on tagged sections of the boundary. The PDE problem needs to be well specified. *Fastflo*'s internal mesh generator provides an unstructured triangular mesh for 2-D problems. The mesh can be concentrated in various areas of the domain and elements with linear or quadratic approximation can be specified. The linear approximation involves nodes on the corners of the triangles, while the latter involves nodes on the mid points of the triangle sides. Any type of computational domain can be represented, including boundaries which comprise circular arcs. The special command *curv* forces the boundary with a specified tag to conform to an arc of a circle. A negative value will result in a concave curvature, while a positive value will produce a convex curvature, as shown in fig. A.1.

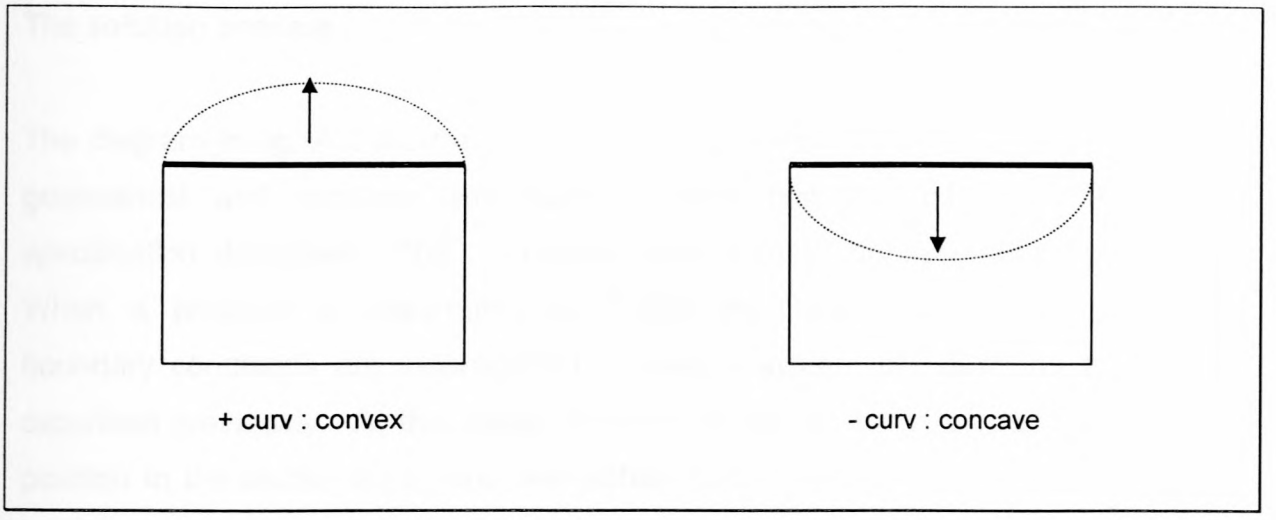

Fig. A.1 : Positive and negative curvatures.

Consider the example below:

P curv 0.2071
b 3 curvature = {curv}

The parameter *curv* has the numerical value for the curvature of the boundary segment with tag 3. This is equal to the ratio of the maximum deviation of the curve from the line segment to the length of the line segment itself, or alternatively, 0.5 tan (*a*/4), where *a* is the angle subtended at the centre of curvature. In the case of a semicircle, this angle is 90°, so 0.5 tan (*a*/4) = 0.5 tan (90°/4) = 0.5 tan 22.5° = 0.2071.

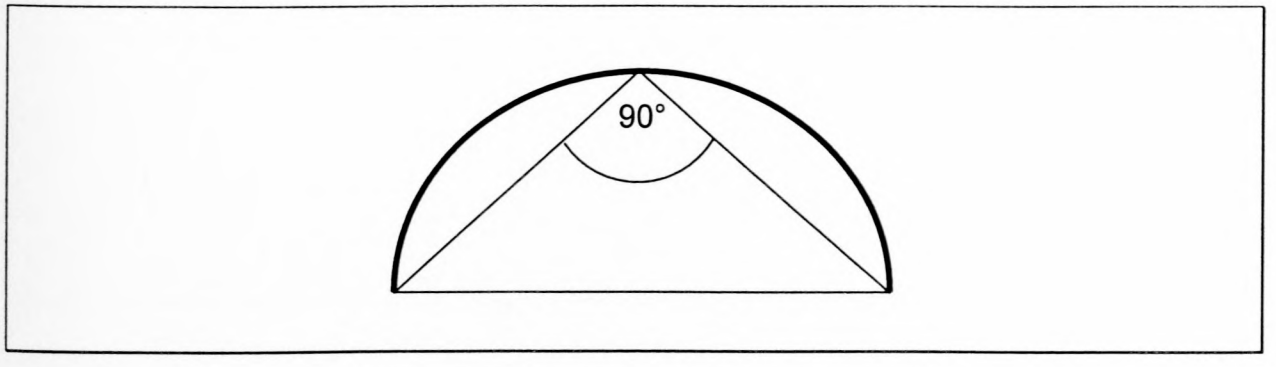

Fig. A.2 : Angle subtended under a semicircle.

The solution process

The diagram in fig. A.3 illustrates the solution process. In order to run *Fastflo*, the geometrical and problem specifications must first be loaded. The problem specification describes PDE problems that need to be assembled and solved. When a problem is assembled in *Fastflo*, the Galerkin method is applied, and boundary conditions are incorporated to yield a system of equations of the form described previously. At this stage, the RHS vector is stored by default in the first position in the vector stack, and the global matrix is stored in a separate memory location. On solving the global system, the nodal values replace the RHS vector in the first position in the stack. The stack is pushed, with the former RHS vector pushed into the second position. *Fastflo* also stores various parameters (defined in **P** statements) and the factors of the last-solved global matrix. Results can be obtained by including all *Fasttalk* commands in the ***.prb** file for the problem, or the buttons on the menu bar in the Graphical User Interface can be clicked, or the necessary *Fasttalk* commands can be typed directly in the input window.

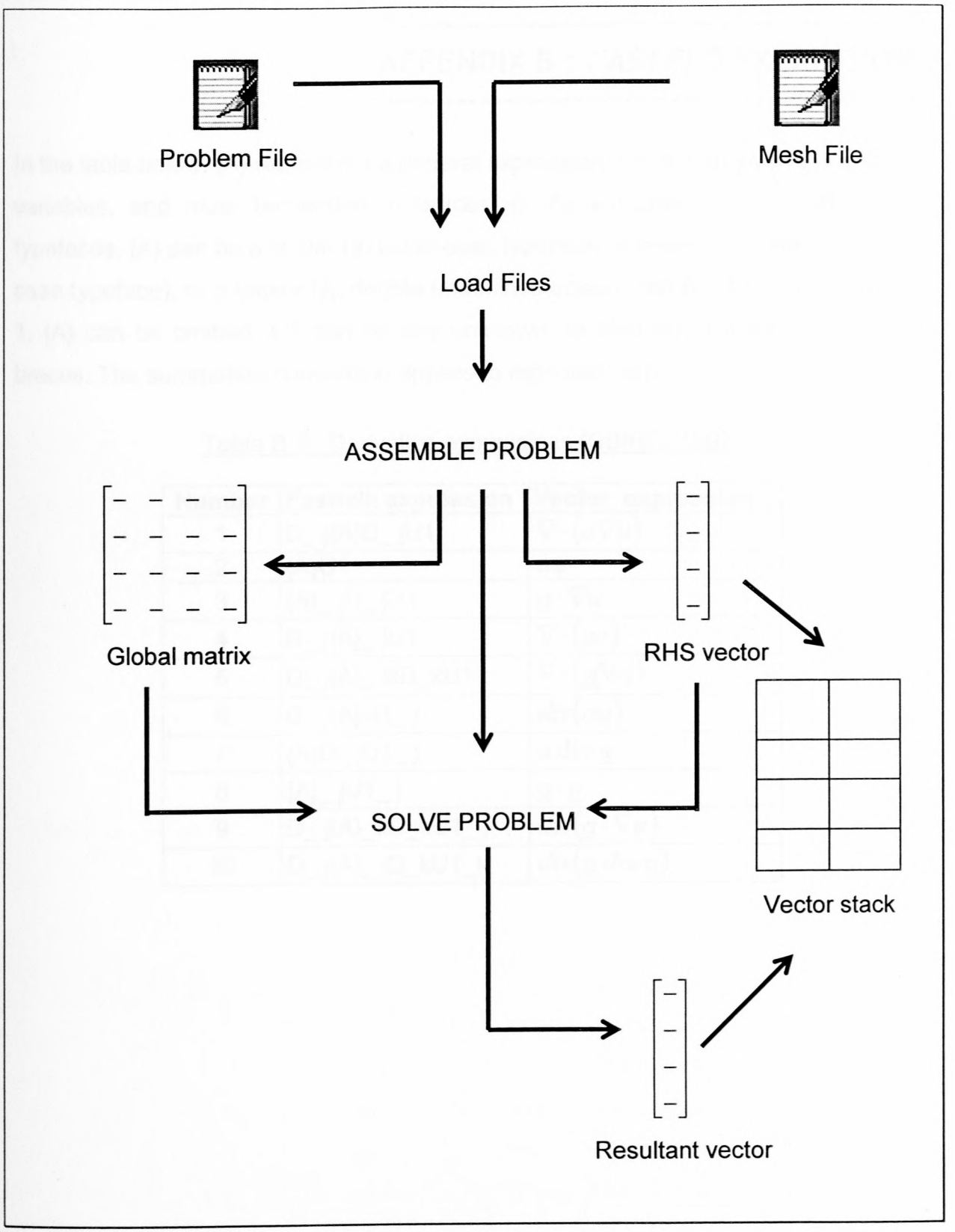

Fig. A.3 : *Fastflo*'s solution process.

APPENDIX B : *FASTFLO* EXPRESSIONS

In the table below, {A} represents a general expression, which can involve any known variables, and must be written in braces, {}. As indicated by the suffices and typefaces, {A} can be a scalar (a, lower-case typeface), a vector (a, underlined lower-case typeface), or a tensor (A, double underlined upper-case typeface). If its value is 1, {A} can be omitted. U1 can be any unknown, or also any expression written in braces. The summation convention applies to repeated suffices.

Table B.1 : Derivative expressions (CSIRO, 1997)

Number	Fasttalk expression	Vector expression
1	D_ j{A}D_ jU1	$\nabla \cdot (a \nabla u)$
2	{A}U1	au
3	{A}_ jD_ jU1	$\underline{a} \cdot \nabla u$
4	D_ j{A}_ jU1	$\nabla \cdot (\underline{a} u)$
5	D_ j{A}_ jkD_kU1	$\nabla \cdot (\underline{\underline{A}} \nabla u)$
6	D_ j{A}U1_ j	$div(a \underline{u})$
7	{A}D_ jU1_ j	$a \,\mathrm{div}\, \underline{u}$
8	{A}_ jU1_ j	$\underline{a} \cdot \underline{u}$
9	D_ j{A}_kD_kU1_ j	$div(\underline{a} \cdot \nabla u)$
10	D_ j{A}_ jD_kU1_k	$div(\underline{a}\, div\, \underline{u})$

APPENDIX C : VERTICES AND BOUNDARIES

Although modules of different sizes were used, only one mesh file can be used for all of them. The only adjustment will be the list of vertices. All vertices are numbered in a clockwise fashion, starting at the bottom lefthand corner at (0; 0), as in fig. C.1. Boundary sections between vertices carry tags, with the same tag number used for boundaries with similar boundary conditions. Boundary tags are given in table C.1. These tags connect the mesh file to the problem file.

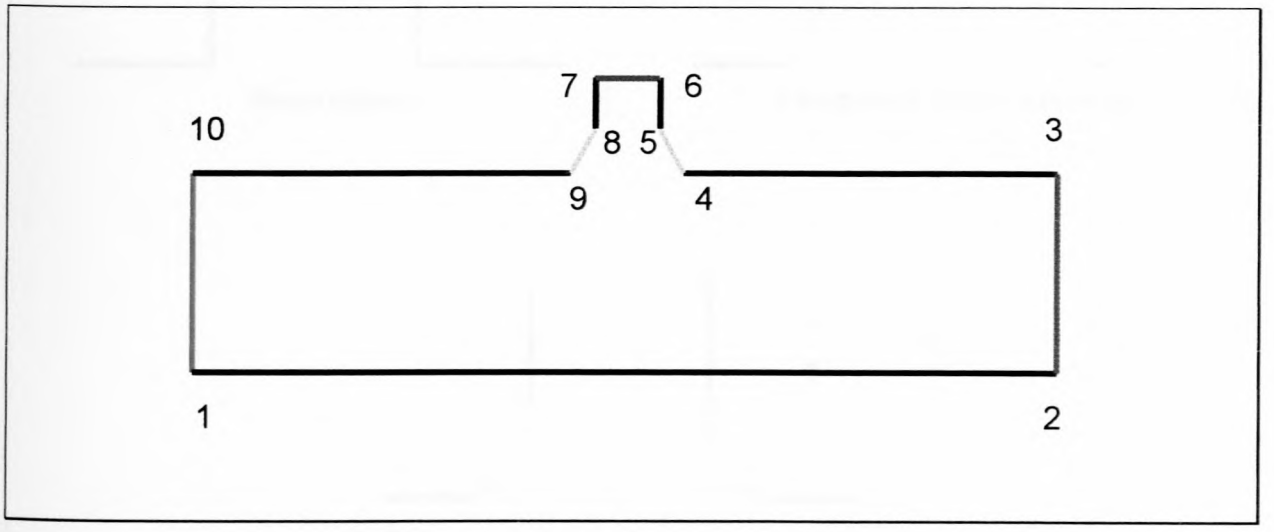

Fig. C.1 : Vertices and boundary sections.

Table C.1 : Vertices and boundary tags

Vertices	Boundary tag	Boundary condition
1-2	wall	No flux over axis of symmetry
2-3	Lout	Known outlet lumen pressure
3-4	wall	No flux over module inner wall
4-5	conv	No flux over convex boundary
5-6	wall	No flux over module inner wall
6-7	Sout	Known outlet shell pressure
7-8	wall	No flux over module inner wall
8-9	conv	No flux over convex boundary
9-10	wall	No flux over module inner wall
10-1	Lin	Known inlet lumen pressure

The numerical simulation had difficulty in coping with sharp edges such as those found at the permeate outlets, due to the sudden discontinuity. The remedy to this problem was to make the edges smooth by using the *curv* command, discussed in Appendix A. First an extra boundary must be inserted. A positive value for *curv* is then used to make this boundary convex. Fig. C.2 shows how this is done.

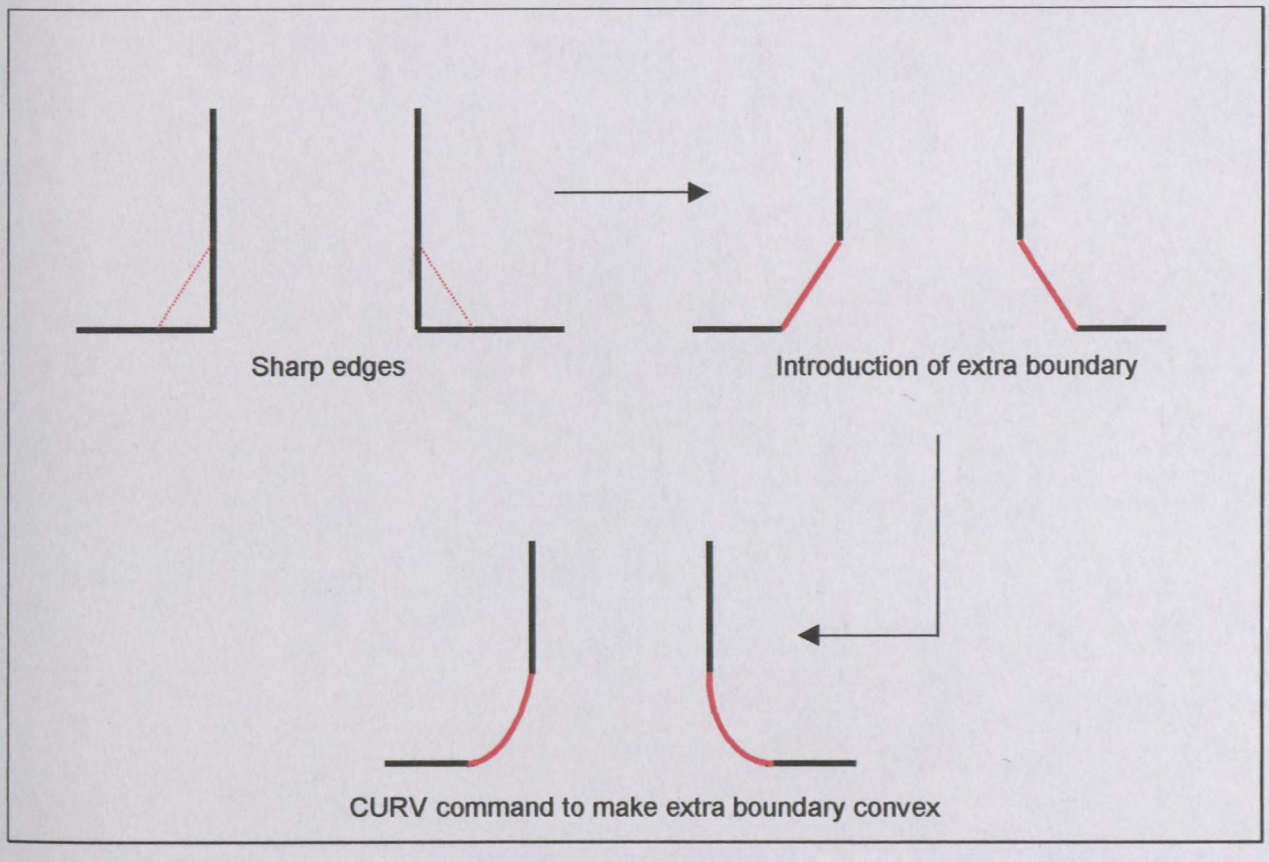

Fig. C.2 : Using the *curv* command to smoothen sharp edges at the permeate outlet (enlarged).

The convex boundaries can be approximated by a quarter of a circle. Using the same methodology as in Appendix A, the angle subtended under the curvature is 135° (see fig. C.3), which yields a value of 0.3341 for the curvature : 0.5 tan ($a/4$) = 0.5 tan (135°/4) = 0.5 tan 33.75° = 0.3341.

The actual computational domain is rectangularly shaped, but because eqns. [5.1] and [5.2] were non-dimensionalised, the same must be done to the computational domain. This will result in a square domain, with all sides equal to unity.

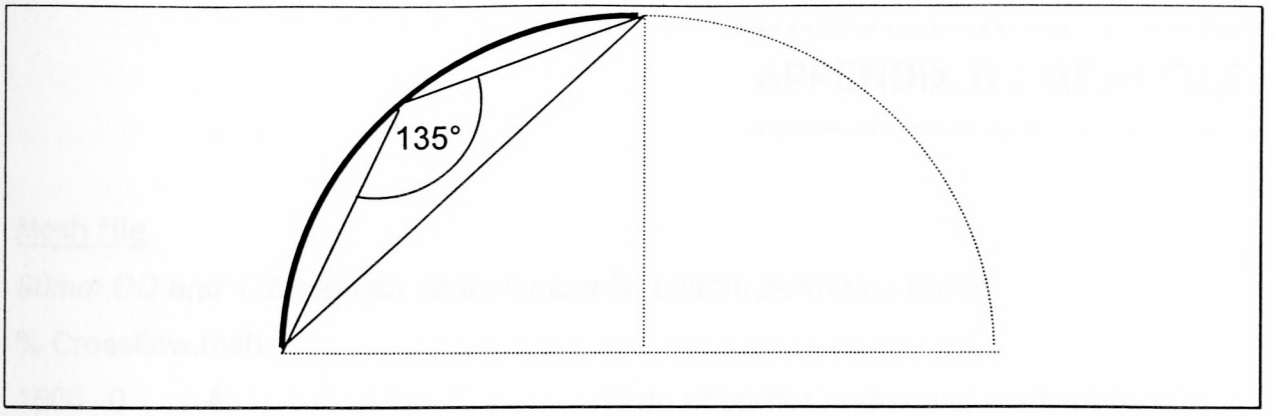

Fig. C.3 : Angle subtended under a quarter of a circle.

APPENDIX D : MESH FILE

Mesh file

90mm OD and 1.2m length vertical module; bottom permeate outlet

% Crossflow.msh

1500 0 4 % nr. of corner nodes and element type

-8 0 0 0 0 % mesh concentrated *at* 8 vertices

1 2 3 4 7 8 9 10 % points of concentration

List of vertices

% Dimensionless radius (column 1) and length (column 2)

%

0.0 0.0

0.96970 0.0

0.96970 0.0049907

0.97576 0.0094907

1.0 0.0094907

1.0 0.0105185

0.97576 0.0105185

0.96970 0.0150185

0.96970 1.0

0.0 1.0

List of boundary tags

1 1

2 2

3 3

4 2

5 4

6 2

7 3

8 2

9 5

10 2

End of boundary list

Discussion

Mesh data for *Fastflo*'s triangular mesh generator contains a complete mesh specification defining each node and element commands which invoke *Fastflo*'s internal mesh generator. The user specifies which triangular element is to be used, a set of vertices which define the boundary of the region, and a series of boundary tags.

The mesh file is divided into three distinct blocks, each containing a series of numbers and separated by lines of text. The first block contains information regarding the nature of the mesh and the elements, the second lists the vertices of the computational domain, and the third is used to tag the boundary segments. The basic format of each block is set out below.

Block 1

I1 I2 I3
J1 J2 J3 J4 J5

I1 indicates the number of corner nodes within the mesh. For triangular elements, each element will have three corner nodes, which it will share with neighbouring elements. I2 is the number of elements within the mesh. Usually, it is set to zero to invoke the internal mesh generator. I3 determines what kind of element will be used. There are two types of triangular elements available in the mesh generator:

I3 = 3 corresponds to 3-noded triangles, where the nodes are the corners of the triangles.
I3 = 4 corresponds to 6-noded triangles, where 3 nodes are the corners of the triangles and 3 nodes are located on the midpoints of the sides of the triangles.

J1 controls the way in which the mesh is to be concentrated.
J1 = 0 means that the mesh will have approximately uniform resolution.
J1 < 0 means the mesh is to be concentrated at particular vertices of the polygonal domain; these vertices are to be listed on the next line.
J1 > 0 means that the mesh is to be concentrated around the points listed.

The remaining arguments J2 to J5 are used for various diagnostic tests and will seldom be required by the user. They are usually set to zero.

In this thesis, the first block of the mesh file looks as follows:

```
% Cross-flow.msh
1000   0    4                          % nr. of corner nodes and element type
-8     0    0    0    0                % mesh concentrated at 8 vertices
1      2    3    4    7    8    9   10  % points of concentration
```

The first line tells the software that 1000 corner nodes must be used, the zero ("0") invokes the internal mesh generator and the "4" tells the software to use 6-noded triangular elements in constructing the mesh. Three nodes are located at the corners of the triangle, while the other 3 nodes are located on the midpoints of the sides of the triangle, as shown in fig. D.1.

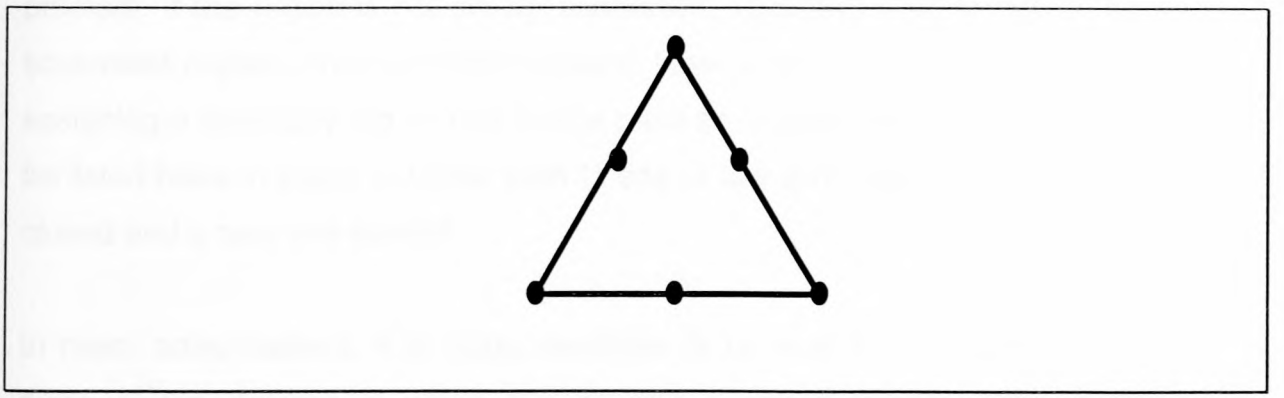

Fig. D.1 : 6-noded triangular element.

The second line starts with "-8", which tells the software to concentrate the mesh at 8 vertices listed on the next line. The negative value means the mesh will be concentrated at the given vertices, whereas a positive value would've concentrated the mesh around those vertices. The four remaining zero's are for diagnostic tests and are very seldom used. Finally the third lines lists all the vertex numbers where the mesh is to be concentrated.

Block 2

x(1,1)	x(1,2)
x(2,1)	x(2,2)
x(i,1)	x(j,2)

where x(i,1) and x(j,2) are the X and Y (or Y and X) coordinates of the vertices of the polygons used to define the mesh region.

Block 3

I1	I2

I1 is a vertex number determined according to the order of the listed vertices in block 2. I2 is the integer tag assigned to the boundary segment that joins vertex I1 with the vertex whose number appears on the next line. These lines can be made curved by using a special form of the **b** boundary statement in the file which specifies the problem. If the region is not simply connected, such as an annulus or topologically equivalent regions, then a bridge between inner and outer boundaries is invoked by assigning a boundary tag 0. This bridge must be crossed twice, and hence needs to be listed twice in Block 3. When both I1 and I2 are zero, then the current polygon is closed and a new one started.

In many computations, it is highly desirable to be able to concentrate the mesh in parts of the domain in which the solution changes rapidly. The *Fastflo* mesh generator produces triangles in which the element sides are as uniform as possible. When the mesh is concentrated in particular regions, the lengths of the element sides in those regions are multiplied by a scaling factor.

APPENDIX E : PROBLEM FILE

Problem file

```
% Crossflow.prb
% PARAMETER VALUES
%
% Variable parameters
P    L       1.2              % module length
P    dP      29869.           % axial pressure drop
P    OD      90.              % module outer diameter
P    ID      80.              % module inner diameter
P    n       1229.            % number of fibres for 62% packing density
%
% Fixed parameters
P    Axis    1                % enforces axisymmetry
P    pi      3.1415927
P    mu      0.001002         % fluid viscosity
P    curv    0.3341           % boundary curvature
P    rC      ID/2./1000.      % module inner radius
P    rL      0.0006           % fibre lumen radius
P    rM      0.0009           % fibre outer radius
P    Leff    L-0.12           % dry effective filtration length
P    Lwet    1.07*Leff        % wet effective filtration length
P    Aflow   pi*rL^2*n        % cross-sectional flow area
P    Adry    2.*pi*rL*Leff*n  % dry membrane surface area
P    Awet    2.*pi*rL*Lwet*n  % wet membrane surface area
P    pLin    100000.          % lumen inlet pressure
P    pLi     pLin/pLin        % dimensionless pLin
P    pLout   pLin-dP          % lumen outlet pressure
P    pLo     pLout/pLin       % dimensionless pLout
P    pSout   0.               % shell side outlet pressure (atmospheric)
P    pSo     pSout/pLin       % dimensionless pSout
P    TMP     ((pLin+pLout)/2)-pSout    % transmembrane pressure
```

```
P     Av          2.*n*rL*Lwet/(rC^2*Leff)    % membrane area per unit volume
P     Lp          2.3e-13                     % membrane permeability
P     psi         n*rM^2*Lwet/(rC^2*Leff)     % fibre volume fraction
P     kxL         n*rL^4*Leff/(8*rC^2*Lwet)   % Darcy permeabilities
P     kxs         rM^2*Leff^2/(4*psi*Lwet^2)*(-(log psi)-1.5+2*psi-0.5*psi^2)
P     krs         rM^2/(4*psi)*(-(log psi)+((psi^2-1)/(psi^2+1)))
P     k1          kxL/kxs                     % dimensionless kxL
P     k2          krs/kxs*Leff^2/rC^2         % dimensionless krs
P     k3          kxs/kxs                     % dimensionless kxs
P     k4          kxs/mu*(pLin/Leff)*(rC*Leff)
P     k5          kxL/mu*(pLin/Leff)*rC^2
P     k6          krs/mu*(pLin/rC)*(rC*Leff)
P     La          Lp*Av*Leff^2/kxs            % dimensionless group
%
D     1     Lout      % lumen outlet
D     2     wall      % walls
D     3     conv      % convex corners
D     4     Sout      % shell outlet
D     5     Lin       % lumen inlet
%
A     pressure
e     D_ j{-k2,0.0,0.0,-k3}_ jkD_kU1 = {La}U2 - {La}U1     % PDE for PS
e     D_ j{0.0,0.0,0.0,k1}_ jkD_kU2 = {La}U2 - {La}U1      % PDE for PL
b     conv  curvature={curv}
b     Sout  U1={pSo}
b     Lin   U2={pLi}
b     Lout  U2={pLo}
%
A     fluxLin
b      Lin   v400=normal
b      Lin   [integrated]  {0.,-k5*v402}_ jD_ j{v102}
%
A     fluxSout
b     Sout  v400=normal
```

```
b       Sout   [integrated]  {-k6*v401,-k4*v402}_ jD_ j{v101}
%

A       fluxLout
b       Lout   v400=normal
b       Lout   [integrated]  {0.,-k5*v402}_ jD_ j{v102}
%
A       veloS
e       v400=[grad]{v101}
e       v600={-k6,0.,0.,-k4}
e       v000={v600 p v401}
%
A       veloL
e       v400=[grad]{v102}
e       v600={0.,0.,0.,-k5}
e       v000={v600 p v401}
%
< run1
  prim
  pressure
  solve
  shade
  fluxLout
    QLout = Out*3600000.
  fluxLin
    QLin = -Out*3600000.
  fluxSout
    QSout = Out*3600000.
!#
  Diff = QLin-QLout
  Error = sqrt(((QSout+Diff)/2.-Diff)^2.)
  PercentError = Error/(QSout+Diff)/2.*100.
  Lpapp = mu*(Diff/3600000)/(Awet*TMP)
  Flux = Diff/Awet
```

```
  diameter = 2*rC*1000.
  PackDens = n*rM^2/(rC^2)*100.
!#
!# Calculated flowrates (L/h):
  show QLin
  show QLout
!#
  show Diff
  show QSout
  show PercentError
  show Flux
!#
  show Length
  show diameter
  show pLin
  show dP
  show pLout
  show n
  show PackDens
  show Aflow
  show Adry
  show Awet
  show Lp
  show Lpapp
  show Flux
>
< run2
  veloS
  black
  arrow 101
  popp
>
< run3
  veloS
```

```
  black
  v500={sqrt((v101*v101)+(v102*v102))}
  cont 501
  shad 501
  popp
>
< run4
  veloL
  black
  arrow 101
  popp
>
< run5
  veloL
  black
  v500={sqrt((v101*v101)+(v102*v102))}
  cont 501
  shad 501
  popp
>
```

Discussion

Generally, the problem file is divided into three distinct blocks with the format below.

```
% Name.prb
P  Parameter   I1
%
A  Problem name
e   Partial differential equation
b   I2  expression
%
< macro
  commands
>
```

The % is used to add comments. The problem file begins with the name of the file, *Name.prb*. The first block is a list of all parameters, specified by the **P** statement. *Parameter* can be anything like sq2, eps or g, except the specially reserved code letters mentioned earlier. I1 can be any numerical value or expression. The second block is used for problems. Multiple problems can be contained in this block. A name is assigned to each problem by the **A** statement, with the particular PDE and boundary conditions below it. I2 is the tag number of the boundary on which the boundary condition applies. The boundary condition is given by an expression. I2 is the same number as that contained in the mesh file, therefore linking the mesh and problem files. Lastly a macro, delimited by < and >, is used for subroutines. This liberates the user from having to type all commands individually in the input window.

All the lines beginning with the **P** atom define the various parameters. The *Axis* command informs the program that the mesh describes an axisymmetric region, with coordinate X1 as the radial coordinate and X2 as the axial coordinate. The % sign is used as a separator between lines or to add comments. The **D** atom assigns names to the tagged boundary sections, as indicated. See fig. C.1 and Table C.1 in Appendix C.

```
A    Pressure
e    D_ j{-k2,0.0,0.0,-k3}_ jkD_kU1={La}U2-{La}U1          % PDE for Ps
e    D_ j{0.0,0.0,0.0,k1}_ jkD_kU2={La}U2-{La}U1          % PDE for PL
b    Sout    U1={piSo}                  % known outlet shell presure
b    Lin     U2={piLi}                  % known inlet lumen pressure
```

The **A** atom declares the name of the problem to be assembled. The problem Pressure contains the two PDEs to be solved. Both lines create the term $\nabla \cdot \left(\underline{\underline{A}} \nabla u \right)$ (expression nr. 5 in Appendix B) where the tensor $\underline{\underline{A}}$ is defined by :

$$\underline{\underline{A}} = \begin{bmatrix} -k2 & 0 \\ 0 & -k3 \end{bmatrix}$$

in the first PDE and

$$\underline{\underline{A}} = \begin{bmatrix} 0 & 0 \\ 0 & k1 \end{bmatrix}$$

in the second PDE.

The result is the second-order expressions

$$-k_2 \frac{1}{R} \frac{\partial}{\partial R}\left(R \frac{\partial P_S}{\partial R} \right) - k_3 \frac{\partial^2 P_S}{\partial X^2}$$

and

$$k_1 \frac{\partial^2 P_L}{\partial X^2}$$

The remainder of the **e** statements is equivalent to

$$La\left(P_L - P_S\right)$$

where the variables *U2* and *U1* refer to P_L and P_S respectively.

The boundary conditions are expressed by the **b** statements. The value of P_s at boundary with tag *Sout* is assigned to be *piSo*, while a value of *piLi* is assigned to P_L at boundary with tag *Lin*. At all other boundaries, a Neuman condition applies, i.e. no-flux or zero pressure gradient conditions over those boundaries. The results of the solutions for P_L and P_S are stored in v102 and v101 respectively.

```
A     fluxLin
b     Lin     v400=normal                          % outward unit normal vector
b     Lin     [integrated] {0.,-k5*v402}_ jD_ j{v102}  % integration of velocity
```

Here, the name of the problem to be assembled is called *fluxLin*. The volumetric flowrate at the boundary tagged *Lin* will be determined by integrating the normal component of the superficial velocity over the area of the specified boundary, where the velocity is the gradient of the pressure. The statement, *v400=normal*, sets v400 to the normal vector, with radial component in v401 and axial component in v402. The third line creates the term $\underline{n}$ *grad v102* (scaled by k5), or $\underline{n} \bullet \nabla P_L$ (expression nr. 3 in Appendix B), which is the product of the normal vector ($\underline{n}$) and the first derivative of P_L (grad P_L). As already mentioned, the normal vector *{0, -k5*v402}* consists of a radial and axial component. In this case, the outward unit normal on boundary *Lin* is in the axial direction, hence the radial component is set to zero. Finally, the keyword *[integrated]* integrates the velocity over the boundary *Lin* and writes the result to the special parameter *Out*.

```
< run
   Pressure                          % call the "Pressure" problem
   solve                             % solve the problem
   fluxLin                           % call the "fluxLin" problem
   Flowrate = Out*3600000.           % multiply result of integration by factor
!#
!# Calculated flowrate (L/h) :      % print heading
   show Flowrate                     % show value of "Flowrate"
>
```

The macro run assembles and solves the *Pressure* problem. The problem *fluxLin* is then called, in which the volumetric flowrate is calculated by integration. The parameter *Out*, which contains the result of the integration, is then multiplied by a factor to convert it to units of L/h. The *show* command is used to display the value of L_p and the corresponding flowrate on the screen. The characters *!#* are used to display text and/or an open space in the results window.

APPENDIX F : ΔP ESTIMATION

Initial estimate for ΔP with Hagen-Poiseuille equation

$$\Delta P = \frac{8\mu L_{eff}}{\pi r_L^4} \cdot \frac{Q_{feed}}{N}, \quad \text{where } Q_{feed} = uA_{flow}$$

Module outer diameter = 90mm

μ	L_{eff}	u	Aflow	rL	N	ΔP
Pa.s	m	m/s	m^2	m	-	Pa
0.001002	0.38	1.2	0.00139	0.0006	1229	10729
0.001002	0.48	1.2	0.00139	0.0006	1229	13509
0.001002	0.58	1.2	0.00139	0.0006	1229	16274
0.001002	0.68	1.2	0.00139	0.0006	1229	19022
0.001002	0.78	1.2	0.00139	0.0006	1229	21755
0.001002	0.88	1.2	0.00139	0.0006	1229	24473
0.001002	0.98	1.2	0.00139	0.0006	1229	27178
0.001002	1.08	1.2	0.00139	0.0006	1229	29869

Estimation of ΔP with the 1-D model of Kelsey *et al.* (1990)

Use initial ΔP calculated by Hagen-Poiseuille and determine $P_{L,out} = P_{L,in} - \Delta P$.

Then use Kelsey's 1-D model to calculate Q_{feed} and thus the inlet velocity, u.

Adjust ΔP until u = 1.2 m/s.

L	m	0.5	0.6	0.7	0.8	0.9	1.0	1.1	1.2
Leff	m	0.38	0.48	0.58	0.68	0.78	0.88	0.98	1.08
Lwet	m	0.41	0.51	0.62	0.73	0.83	0.94	1.05	1.16
rS	m	0.0011	0.0011	0.0011	0.0011	0.0011	0.0011	0.0011	0.0011
γ	-	0.382	0.382	0.382	0.382	0.382	0.382	0.382	0.382
κ	-	1.76E-04	2.81E-04	4.10E-04	5.64E-04	7.42E-04	9.44E-04	1.17E-03	1.42E-03
λ	-	0.101	0.127	0.154	0.181	0.207	0.234	0.26	0.287
α	m^4s/kg	-1.50E-07	-1.20E-07	-1.00E-07	-8.60E-08	-7.50E-08	-6.60E-08	-6.00E-08	-5.40E-08
PL,in	Pa	100,000	100,000	100,000	100,000	100,000	100,000	100,000	100,000
ΔP	Pa	10,729	13,509	16,274	19,022	21,755	24,473	27,178	29,869
PL,out	Pa	89,271	86,490	83,725	80,975	78,242	75,522	72,815	70,120
B1	Pa	-29,770	-29,770	-29,770	-29,770	-29,770	-29,770	-29,770	-29,770
B3	Pa	-7,860	-9,928	-11,997	-14,066	-16,134	-18,202	-20,270	-22,339
Qfeed	L/h	6,005	6,005	6,005	6,005	6,005	6,005	6,005	6,005
Qfeed	m^3/s	1.67E-3	1.67E-3	1.67E-3	1.67E-3	1.67E-3	1.67E-3	1.67E-3	1.67E-3
A_{flow}	m^2	0.00139	0.00139	0.00139	0.00139	0.00139	0.00139	0.00139	0.00139
u	m/s	1.2	1.2	1.2	1.2	1.2	1.2	1.2	1.2

$$Q_{feed} = \alpha(\lambda B_1 + B_3)$$

where

$$\alpha = -\frac{N\pi r_L^4}{8\mu L_{wet}}$$

$$\lambda = 4\sqrt{\kappa(1+1/\gamma)}$$

$$\kappa = \frac{L_p L_{wet}^2}{r_L^3}$$

$$\gamma = \left(\frac{1}{r_L^4}\right)\left[4r_S^4 \ln(r_S / r_M) + 4r_S^2 r_M^2 - 3r_S^4 - r_M^4\right]$$

$$B_1 = \frac{(P_{S,out} - P_{L,in})[\cosh(\lambda) - 1] + (P_{L,out} - P_{L,in})\left[1 + \frac{\cosh(\lambda)}{\gamma}\right]}{\frac{[\lambda - \sinh(\lambda)][\cosh(\lambda) - 1]}{\gamma} + \left[\frac{\lambda}{\gamma} + \sinh(\lambda)\right]\left[1 + \frac{\cosh(\lambda)}{\gamma}\right]}$$

$$B_3 = \frac{\lambda}{\gamma} B_1$$

APPENDIX G : L_p VALUES

L_p and $L_{p,app}$ values for correction plot

	A	B	C	D	E
Lp[m]	Lp,app (m)	Lp,app (m)	Lp,app (m)	Lp,app (m)	Lp,app (m)
1.00E-13	9.890E-14	9.926E-14	9.970E-14	9.830E-14	9.900E-14
1.00E-12	8.960E-13	9.000E-13	9.527E-13	9.590E-13	9.450E-13
1.00E-11	4.730E-12	5.140E-12	6.684E-12	7.786E-12	6.490E-12
1.00E-10	9.550E-12	1.769E-11	2.270E-11	3.464E-11	1.723E-11
1.00E-09	1.250E-11	6.140E-11	6.738E-11	1.212E-10	2.341E-11

Configuration A

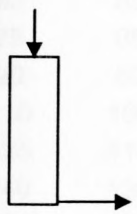

Configuration B

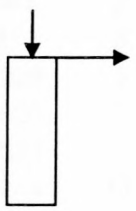

Configuration C

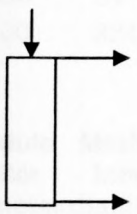

Configuration D

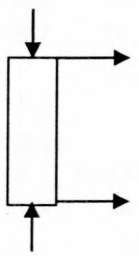

Configuration E

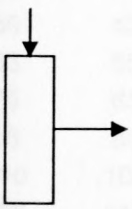

APPENDIX H : MODULE PARAMETERS

Module parameters

Module outer diameter	Module inner diameter	Length	Effective length	Fibre outer diameter	Fibre inner diameter	Packing density	Number of fibres	Membrane area	Flow area
mm	mm	m	m	mm	mm	%	-	m^2	m^2
20	17	**1.2**	1.08	1.8	1.2	62.2	55	0.23	6.27E-05
25	22	**1.2**	1.08	1.8	1.2	62.2	93	0.38	1.05E-04
32	29	**1.2**	1.08	1.8	1.2	62.2	161	0.66	1.83E-04
40	37	**1.2**	1.08	1.8	1.2	62.2	263	1.07	2.97E-04
50	42	**1.2**	1.08	1.8	1.2	62.2	339	1.38	3.83E-04
63	55	**1.2**	1.08	1.8	1.2	62.2	581	2.36	6.57E-04
75	65	**1.2**	1.08	1.8	1.2	62.2	811	3.30	9.17E-04
90	80	**1.2**	1.08	1.8	1.2	62.2	1229	5.00	1.39E-03
110	100	**1.2**	1.08	1.8	1.2	62.2	1920	7.82	2.17E-03
125	115	**1.2**	1.08	1.8	1.2	62.2	2539	10.34	2.87E-03
140	130	**1.2**	1.08	1.8	1.2	62.2	3244	13.21	3.67E-03
160	150	**1.2**	1.08	1.8	1.2	62.2	4319	17.59	4.89E-03
200	190	**1.2**	1.08	1.8	1.2	62.2	6930	28.22	7.84E-03
250	240.2	**1.2**	1.08	1.8	1.2	62.2	11076	45.10	1.25E-02
315	302.6	**1.2**	1.08	1.8	1.2	62.2	17579	71.57	1.99E-02
355	341.0	**1.2**	1.08	1.8	1.2	62.2	22323	90.89	2.52E-02
400	384.4	**1.2**	1.08	1.8	1.2	62.2	28367	115.50	3.21E-02

Module outer diameter	Module inner diameter	Length	Effective length	Fibre outer diameter	Fibre inner diameter	Packing density	Number of fibres	Membrane area	Flow area
mm	mm	m	m	mm	mm	%	-	m^2	m^2
20	17	**1.1**	0.98	1.8	1.2	62.2	55	0.20	6.27E-05
25	22	**1.1**	0.98	1.8	1.2	62.2	93	0.34	1.05E-04
32	29	**1.1**	0.98	1.8	1.2	62.2	161	0.60	1.83E-04
40	37	**1.1**	0.98	1.8	1.2	62.2	263	0.97	2.97E-04
50	42	**1.1**	0.98	1.8	1.2	62.2	339	1.25	3.83E-04
63	55	**1.1**	0.98	1.8	1.2	62.2	581	2.15	6.57E-04
75	65	**1.1**	0.98	1.8	1.2	62.2	811	3.00	9.17E-04
90	80	**1.1**	0.98	1.8	1.2	62.2	1229	4.54	1.39E-03
110	100	**1.1**	0.98	1.8	1.2	62.2	1920	7.09	2.17E-03
125	115	**1.1**	0.98	1.8	1.2	62.2	2539	9.38	2.87E-03
140	130	**1.1**	0.98	1.8	1.2	62.2	3244	11.99	3.67E-03
160	150	**1.1**	0.98	1.8	1.2	62.2	4319	15.96	4.89E-03
200	190	**1.1**	0.98	1.8	1.2	62.2	6930	25.60	7.84E-03
250	240.2	**1.1**	0.98	1.8	1.2	62.2	11076	40.92	1.25E-02
315	302.6	**1.1**	0.98	1.8	1.2	62.2	17579	64.94	1.99E-02
355	341.0	**1.1**	0.98	1.8	1.2	62.2	22323	82.47	2.52E-02
400	384.4	**1.1**	0.98	1.8	1.2	62.2	28367	104.80	3.21E-02

Module outer diameter	Module inner diameter	Length	Effective length	Fibre outer diameter	Fibre inner diameter	Packing density	Number of fibres	Membrane area	Flow area
mm	mm	m	m	mm	mm	%	-	m^2	m^2
20	17	**1.0**	0.88	1.8	1.2	62.2	55	0.18	6.27E-05
25	22	**1.0**	0.88	1.8	1.2	62.2	93	0.31	1.05E-04
32	29	**1.0**	0.88	1.8	1.2	62.2	161	0.54	1.83E-04
40	37	**1.0**	0.88	1.8	1.2	62.2	263	0.87	2.97E-04
50	42	**1.0**	0.88	1.8	1.2	62.2	339	1.12	3.83E-04
63	55	**1.0**	0.88	1.8	1.2	62.2	581	1.93	6.57E-04
75	65	**1.0**	0.88	1.8	1.2	62.2	811	2.69	9.17E-04
90	80	**1.0**	0.88	1.8	1.2	62.2	1229	4.08	1.39E-03
110	100	**1.0**	0.88	1.8	1.2	62.2	1920	6.37	2.17E-03
125	115	**1.0**	0.88	1.8	1.2	62.2	2539	8.42	2.87E-03
140	130	**1.0**	0.88	1.8	1.2	62.2	3244	10.76	3.67E-03
160	150	**1.0**	0.88	1.8	1.2	62.2	4319	14.33	4.89E-03
200	190	**1.0**	0.88	1.8	1.2	62.2	6930	22.99	7.84E-03
250	240.2	**1.0**	0.88	1.8	1.2	62.2	11076	36.75	1.25E-02
315	302.6	**1.0**	0.88	1.8	1.2	62.2	17579	58.32	1.99E-02
355	341.0	**1.0**	0.88	1.8	1.2	62.2	22323	74.06	2.52E-02
400	384.4	**1.0**	0.88	1.8	1.2	62.2	28367	94.11	3.21E-02

Module outer diameter	Module inner diameter	Length	Effective length	Fibre outer diameter	Fibre inner diameter	Packing density	Number of fibres	Membrane area	Flow area
mm	mm	m	m	mm	mm	%	-	m^2	m^2
20	17	**0.9**	0.78	1.8	1.2	62.2	55	0.16	6.27E-05
25	22	**0.9**	0.78	1.8	1.2	62.2	93	0.27	1.05E-04
32	29	**0.9**	0.78	1.8	1.2	62.2	161	0.47	1.83E-04
40	37	**0.9**	0.78	1.8	1.2	62.2	263	0.77	2.97E-04
50	42	**0.9**	0.78	1.8	1.2	62.2	339	1.00	3.83E-04
63	55	**0.9**	0.78	1.8	1.2	62.2	581	1.71	6.57E-04
75	65	**0.9**	0.78	1.8	1.2	62.2	811	2.39	9.17E-04
90	80	**0.9**	0.78	1.8	1.2	62.2	1229	3.61	1.39E-03
110	100	**0.9**	0.78	1.8	1.2	62.2	1920	5.65	2.17E-03
125	115	**0.9**	0.78	1.8	1.2	62.2	2539	7.47	2.87E-03
140	130	**0.9**	0.78	1.8	1.2	62.2	3244	9.54	3.67E-03
160	150	**0.9**	0.78	1.8	1.2	62.2	4319	12.70	4.89E-03
200	190	**0.9**	0.78	1.8	1.2	62.2	6930	20.38	7.84E-03
250	240.2	**0.9**	0.78	1.8	1.2	62.2	11076	32.57	1.25E-02
315	302.6	**0.9**	0.78	1.8	1.2	62.2	17579	51.69	1.99E-02
355	341.0	**0.9**	0.78	1.8	1.2	62.2	22323	65.64	2.52E-02
400	384.4	**0.9**	0.78	1.8	1.2	62.2	28367	83.41	3.21E-02

Module outer diameter	Module inner diameter	Length	Effective length	Fibre outer diameter	Fibre inner diameter	Packing density	Number of fibres	Membrane area	Flow Area
mm	mm	m	m	mm	mm	%	-	m^2	m^2
20	17	**0.8**	0.68	1.8	1.2	62.2	55	0.14	6.27E-05
25	22	**0.8**	0.68	1.8	1.2	62.2	93	0.24	1.05E-04
32	29	**0.8**	0.68	1.8	1.2	62.2	161	0.41	1.83E-04
40	37	**0.8**	0.68	1.8	1.2	62.2	263	0.67	2.97E-04
50	42	**0.8**	0.68	1.8	1.2	62.2	339	0.87	3.83E-04
63	55	**0.8**	0.68	1.8	1.2	62.2	581	1.49	6.57E-04
75	65	**0.8**	0.68	1.8	1.2	62.2	811	2.08	9.17E-04
90	80	**0.8**	0.68	1.8	1.2	62.2	1229	3.15	1.39E-03
110	100	**0.8**	0.68	1.8	1.2	62.2	1920	4.92	2.17E-03
125	115	**0.8**	0.68	1.8	1.2	62.2	2539	6.51	2.87E-03
140	130	**0.8**	0.68	1.8	1.2	62.2	3244	8.32	3.67E-03
160	150	**0.8**	0.68	1.8	1.2	62.2	4319	11.07	4.89E-03
200	190	**0.8**	0.68	1.8	1.2	62.2	6930	17.77	7.84E-03
250	240.2	**0.8**	0.68	1.8	1.2	62.2	11076	28.39	1.25E-02
315	302.6	**0.8**	0.68	1.8	1.2	62.2	17579	45.06	1.99E-02
355	341.0	**0.8**	0.68	1.8	1.2	62.2	22323	57.23	2.52E-02
400	384.4	**0.8**	0.68	1.8	1.2	62.2	28367	72.72	3.21E-02

Module outer diameter	Module inner diameter	Length	Effective length	Fibre outer diameter	Fibre inner diameter	Packing density	Number of fibres	Membrane area	Flow area
mm	mm	m	m	mm	mm	%	-	m^2	m^2
20	17	**0.7**	0.58	1.8	1.2	62.2	55	0.12	6.27E-05
25	22	**0.7**	0.58	1.8	1.2	62.2	93	0.20	1.05E-04
32	29	**0.7**	0.58	1.8	1.2	62.2	161	0.35	1.83E-04
40	37	**0.7**	0.58	1.8	1.2	62.2	263	0.57	2.97E-04
50	42	**0.7**	0.58	1.8	1.2	62.2	339	0.74	3.83E-04
63	55	**0.7**	0.58	1.8	1.2	62.2	581	1.27	6.57E-04
75	65	**0.7**	0.58	1.8	1.2	62.2	811	1.77	9.17E-04
90	80	**0.7**	0.58	1.8	1.2	62.2	1229	2.69	1.39E-03
110	100	**0.7**	0.58	1.8	1.2	62.2	1920	4.20	2.17E-03
125	115	**0.7**	0.58	1.8	1.2	62.2	2539	5.55	2.87E-03
140	130	**0.7**	0.58	1.8	1.2	62.2	3244	7.09	3.67E-03
160	150	**0.7**	0.58	1.8	1.2	62.2	4319	9.44	4.89E-03
200	190	**0.7**	0.58	1.8	1.2	62.2	6930	15.15	7.84E-03
250	240.2	**0.7**	0.58	1.8	1.2	62.2	11076	24.22	1.25E-02
315	302.6	**0.7**	0.58	1.8	1.2	62.2	17579	38.44	1.99E-02
355	341.0	**0.7**	0.58	1.8	1.2	62.2	22323	48.81	2.52E-02
400	384.4	**0.7**	0.58	1.8	1.2	62.2	28367	62.03	3.21E-02

Module outer diameter	Module inner diameter	Length	Effective length	Fibre outer diameter	Fibre inner diameter	Packing density	Number of fibres	Membrane area	Flow Area
mm	mm	m	m	mm	mm	%	-	m^2	m^2
20	17	**0.6**	0.48	1.8	1.2	62.2	55	0.10	6.27E-05
25	22	**0.6**	0.48	1.8	1.2	62.2	93	0.17	1.05E-04
32	29	**0.6**	0.48	1.8	1.2	62.2	161	0.29	1.83E-04
40	37	**0.6**	0.48	1.8	1.2	62.2	263	0.48	2.97E-04
50	42	**0.6**	0.48	1.8	1.2	62.2	339	0.61	3.83E-04
63	55	**0.6**	0.48	1.8	1.2	62.2	581	1.05	6.57E-04
75	65	**0.6**	0.48	1.8	1.2	62.2	811	1.47	9.17E-04
90	80	**0.6**	0.48	1.8	1.2	62.2	1229	2.22	1.39E-03
110	100	**0.6**	0.48	1.8	1.2	62.2	1920	3.47	2.17E-03
125	115	**0.6**	0.48	1.8	1.2	62.2	2539	4.59	2.87E-03
140	130	**0.6**	0.48	1.8	1.2	62.2	3244	5.87	3.67E-03
160	150	**0.6**	0.48	1.8	1.2	62.2	4319	7.82	4.89E-03
200	190	**0.6**	0.48	1.8	1.2	62.2	6930	12.54	7.84E-03
250	240.2	**0.6**	0.48	1.8	1.2	62.2	11076	20.04	1.25E-02
315	302.6	**0.6**	0.48	1.8	1.2	62.2	17579	31.81	1.99E-02
355	341.0	**0.6**	0.48	1.8	1.2	62.2	22323	40.39	2.52E-02
400	384.4	**0.6**	0.48	1.8	1.2	62.2	28367	51.33	3.21E-02

Module outer diameter	Module inner diameter	Length	Effective length	Fibre outer diameter	Fibre inner diameter	Packing density	Number of fibres	Membrane area	Flow area
mm	mm	m	m	mm	mm	%	-	m^2	m^2
20	17	**0.5**	0.38	1.8	1.2	62.2	55	0.08	6.27E-05
25	22	**0.5**	0.38	1.8	1.2	62.2	93	0.13	1.05E-04
32	29	**0.5**	0.38	1.8	1.2	62.2	161	0.23	1.83E-04
40	37	**0.5**	0.38	1.8	1.2	62.2	263	0.38	2.97E-04
50	42	**0.5**	0.38	1.8	1.2	62.2	339	0.49	3.83E-04
63	55	**0.5**	0.38	1.8	1.2	62.2	581	0.83	6.57E-04
75	65	**0.5**	0.38	1.8	1.2	62.2	811	1.16	9.17E-04
90	80	**0.5**	0.38	1.8	1.2	62.2	1229	1.76	1.39E-03
110	100	**0.5**	0.38	1.8	1.2	62.2	1920	2.75	2.17E-03
125	115	**0.5**	0.38	1.8	1.2	62.2	2539	3.64	2.87E-03
140	130	**0.5**	0.38	1.8	1.2	62.2	3244	4.65	3.67E-03
160	150	**0.5**	0.38	1.8	1.2	62.2	4319	6.19	4.89E-03
200	190	**0.5**	0.38	1.8	1.2	62.2	6930	9.93	7.84E-03
250	240.2	**0.5**	0.38	1.8	1.2	62.2	11076	15.87	1.25E-02
315	302.6	**0.5**	0.38	1.8	1.2	62.2	17579	25.18	1.99E-02
355	341.0	**0.5**	0.38	1.8	1.2	62.2	22323	31.98	2.52E-02
400	384.4	**0.5**	0.38	1.8	1.2	62.2	28367	40.64	3.21E-02

APPENDIX I : EQUIPMENT COSTS

Cost of fibres

27c per 1.4 m length; Fibre packing density = 62.2%

Assume 1.4 m fibre length is used for all module lengths

Module outer diameter (mm)	Number of fibres	Cost of fibres
20	55	R14.98
25	93	R25.09
32	161	R43.60
40	263	R70.98
50	339	R91.46
63	581	R156.84
75	811	R219.06
90	1229	R331.83
110	1920	R518.48
125	2540	R685.70
140	3245	R876.24
160	4321	R1166.59
200	6932	R1871.73
250	11079	R2991.45
315	17584	R4747.59
355	22330	R6028.99
400	28375	R7661.30

Cost of Duroflow ™ u-PVC pipe

Costs (VAT excluded) as at October 2000. Pipe is bought in 6m lengths.

Class	Wall thickness [mm]	OD [mm]	Cost [R/m]	Cost [R/6m]
16	1.5	20	R 4.35	R 26.10
12	1.5	25	R 5.51	R 33.06
9	1.5	32	R 7.03	R 42.18
6	1.7	40	R 8.36	R 50.16
4	1.5	50	R 8.95	R 53.70
4	1.5	63	R 11.51	R 69.06
4	1.5	75	R 13.64	R 81.84
4	1.8	90	R 19.32	R 115.92
6	2.2	110	R 34.83	R 208.98
6	2.5	125	R 52.77	R 316.62
6	2.8	140	R 62.79	R 376.74
6	3.2	160	R 70.80	R 424.80
6	3.9	200	R 110.58	R 663.48
6	4.9	250	R 163.49	R 980.94
6	6.2	315	R 261.47	R 1,568.82
6	7.0	355	R 342.17	R 2,053.02
6	7.8	400	R 428.41	R 2,570.46

Cost of module housing

The table below shows the cost of module housings for various combinations of module length and outer diameter (OD). The cost is based on the cost of u-PVC pipe per 6m length and the number of module lengths that can be obtained from each 6m pipe length.

Module length		0.5m	0.6m	0.7m	0.8m	0.9m	1.0m	1.1m	1.2m
Modules / 6m		12	10	8	7	6	6	5	5
OD	**R/6m**								
20	R 26.10	R 2.18	R 2.61	R 3.26	R 3.73	R 4.35	R 4.35	R 5.22	R 5.22
25	R 33.06	R 2.76	R 3.31	R 4.13	R 4.72	R 5.51	R 5.51	R 6.61	R 6.61
32	R 42.18	R 3.52	R 4.22	R 5.27	R 6.03	R 7.03	R 7.03	R 8.44	R 8.44
40	R 50.16	R 4.18	R 5.02	R 6.27	R 7.17	R 8.36	R 8.36	R 10.03	R 10.03
50	R 53.70	R 4.48	R 5.37	R 6.71	R 7.67	R 8.95	R 8.95	R 10.74	R 10.74
63	R 69.06	R 5.76	R 6.91	R 8.63	R 9.87	R 11.51	R 11.51	R 13.81	R 13.81
75	R 81.84	R 6.82	R 8.18	R 10.23	R 11.69	R 13.64	R 13.64	R 16.37	R 16.37
90	R 115.92	R 9.66	R 11.59	R 14.49	R 16.56	R 19.32	R 19.32	R 23.18	R 23.18
110	R 208.98	R 17.42	R 20.90	R 26.12	R 29.85	R 34.83	R 34.83	R 41.80	R 41.80
125	R 316.62	R 26.39	R 31.66	R 39.58	R 45.23	R 52.77	R 52.77	R 63.32	R 63.32
140	R 376.74	R 31.40	R 37.67	R 47.09	R 53.82	R 62.79	R 62.79	R 75.35	R 75.35
160	R 424.80	R 35.40	R 42.48	R 53.10	R 60.69	R 70.80	R 70.80	R 84.96	R 84.96
200	R 663.48	R 55.29	R 66.35	R 82.94	R 94.78	R 110.58	R 110.58	R 132.70	R 132.70
250	R 980.94	R 81.75	R 98.09	R 122.62	R 140.13	R 163.49	R 163.49	R 196.19	R 196.19
315	R 1,568.82	R 130.74	R 156.88	R 196.10	R 224.12	R 261.47	R 261.47	R 313.76	R 313.76
355	R 2,053.02	R 171.09	R 205.30	R 256.63	R 293.29	R 342.17	R 342.17	R 410.60	R 410.60
400	R 2,570.46	R 214.21	R 257.05	R 321.31	R 367.21	R 428.41	R 428.41	R 514.09	R 514.09

Total capital cost

Total capital cost = cost of fibres + cost of module housing

L →	0.5m	0.6m	0.7m	0.8m	0.9m	1.0m	1.1m	1.2m
OD ↓								
20mm	R 17.16	R17.59	R 18.25	R 18.71	R19.33	R19.33	R 20.20	R 20.20
25mm	R 27.85	R 28.40	R 29.23	R 29.82	R 30.60	R 30.60	R 31.71	R 31.71
32mm	R 47.12	R 47.82	R 48.88	R 49.63	R 50.63	R 50.63	R 52.04	R 52.04
40mm	R 75.16	R 76.00	R 77.25	R 78.15	R 79.34	R 79.34	R 81.01	R 81.01
50mm	R 95.94	R 96.83	R 98.17	R 99.13	R 100.41	R 100.41	R 102.20	R 102.20
63mm	R 162.20	R 163.75	R 165.47	R 166.71	R 168.35	R 168.35	R 170.65	R 170.65
75mm	R 225.88	R 227.24	R 229.29	R 230.75	R 232.70	R 232.70	R 235.43	R 235.43
90mm	R 341.49	R 343.42	R 346.32	R 348.39	R 351.15	R 351.15	R 355.01	R 355.01
110mm	R 535.90	R 539.38	R 544.61	R 548.34	R 553.31	R 553.31	R 560.28	R 560.28
125mm	R 712.08	R 717.36	R 725.27	R 730.93	R 738.47	R 738.47	R 749.02	R 749.02
140mm	R 907.63	R 913.91	R 923.33	R 930.06	R 939.03	R 939.03	R 951.59	R 951.59
160mm	R 1201.99	R 1209.07	R 1219.69	R 1227.28	R 1237.39	R 1237.39	R 1251.55	R 1251.55
200mm	R 1927.02	R 1938.08	R 1954.66	R 1966.51	R 1982.31	R 1982.31	R 2004.42	R 2004.42
250mm	R 3073.19	R 3089.54	R 3114.07	R 3131.58	R 3154.94	R 3154.94	R 3187.64	R 3187.64
315mm	R 4878.33	R 4904.48	R 4943.70	R 4971.71	R 5009.06	R 5009.06	R 5061.36	R 5061.36
355mm	R 6200.07	R 6234.29	R 6285.62	R 6322.28	R 6371.16	R 6371.16	R 6439.59	R 6439.59
400mm	R 7875.50	R 7918.35	R 7982.61	R 8028.51	R 8089.71	R 8089.71	R 8175.39	R 8175.39

APPENDIX J : PARAMETERS USED

Parameters used for cost calculations

Parameter	Symbol	Unit	Value
Pump efficiency	η	-	0.7
Flow rate conversion factor	C	-	2.777E-07
Pressure drop across module	$\Delta P_{0.5}$	kPa	10.73
Pressure drop across module	$\Delta P_{0.6}$	kPa	13.51
Pressure drop across module	$\Delta P_{0.7}$	kPa	16.28
Pressure drop across module	$\Delta P_{0.8}$	kPa	19.03
Pressure drop across module	$\Delta P_{0.9}$	kPa	21.76
Pressure drop across module	$\Delta P_{1.0}$	kPa	24.48
Pressure drop across module	$\Delta P_{1.1}$	kPa	27.19
Pressure drop across module	$\Delta P_{1.2}$	kPa	29.88
Feed pressure	P_f	kPa	100
Required product flow rate	Q_{req}	L/h	variable
Packing density	PD	%	62.2
Operating time per year	θ	h/yr	8000
Inlet flow velocity	u	m/s	1.2
Capital Recovery Factor	CRF	1/yr	0.3
Cost of electricity	C_{kWh}	c/kWh	30.27c

APPENDIX K : SPREADSHEET EXAMPLE

Spreadsheet for cost calculations

A spreadsheet was constructed in the fashion below, using the parameters in Appendix F. Outer module diameter ranged from 20mm – 400mm, while module length ranged from 0.5m – 1.2m

Row number	Description	Symbol	Unit	Series 1	Series 2	Series 3	Series n
A = specified	Outer module diameter	Do	mm	90	110	125	...
B = specified	Module length	L	m	1.2	1.2	1.2	...
C = specified	Packing density	PD	%	62%	62%	62%	...
D = L/h to m^3/s	Flow rate factor	C	-	2.78E-07	2.78E-07	2.78E-07	...
E = function of B	Axial pressure drop	ΔP	kPa	29.88	29.88	29.88	...
F = from Fastflo	Flux	J	LMH	67.18	68.00	68.44	...
G = specified	Membrane area per module	Am	m^2	5.00	7.82	10.34	...
H = specified	Permeate required	Qreq	L/h	1000	1000	1000	...
I = H/F	Required membrane area	Areq	m^2	14.89	14.71	14.61	...
J = I/G	Number of modules	N	-	3	2	2	...
K = J x G	Actual membrane area	Atot	m^2	15.00	15.64	20.68	...
L = F x K	Actual permeate	Qact	L/h	1008	1064	1415	...
M = Qfeed x J	Total feed flowrate	Q	L/h	18014	18765	24816	...
N = specified	Pump efficiency	η	-	0.7	0.7	0.7	...
O = D x E x M / N	Energy consumption	E	kW	0.21	0.22	0.29	...
P = specified	Electricity cost	CkWh	R/kWh	0.3027	0.3027	0.3027	...
Q = specified	Operating time	θ	h/yr	8000	8000	8000	...
R = O x P x Q	Pumping cost per year	Cyr	R/yr	R 517	R 539	R 712	...
S = R / (Q x H)	Pumping cost	Cpump	c/kL	6.46	6.73	8.90	...
T = J x (cap)*	Capital Cost	Ccap	c/kL	13.31	14.01	18.73	...
U = S + T	Total cost	Ctot	c/kL	19.77	20.74	27.63	...
V = K / I	Area ratio	Ar	-	1.01	1.06	1.42	...
W = U x V	Adjusted cost	Cadj	c/kL	19.62	19.50	19.52	...

* : cap = (Capital cost per module $\times$ N $\times$ CRF) / (Q_{req} $\times$ θ)

where Capital cost = cost of fibres + cost of module housing (see Appendix E)